Validation of the 350 km Effective Height of the Ionosphere for the Low Latitude Region of East Africa

Phillip Opio
2021/PhD/004/PS

Thesis Submitted to Faculty of Science in Fulfillment of the Requirements for the Award of the Degree of Doctor of Philosophy in Physics of Mbarara University of Science and Technology

September, 2024

Declaration

I, OPIO PHILLIP, declare that the work presented in this thesis is my original research work and it has never been presented at any institution for any accademic award. Where I have used the works of other persons, due acknowledgements and sources are provided.

Date: 17/09/2024

Signature: 

Approval

The research has been done under our supervision and submitted with our approval.

Dr. Geoffrey Andima
Department of Physics,
Faculty of Science and Education,
Busitema University.

Signature: _____

Date: 17-09-2024

Assoc. Prof. Edward Jurua
Department of Physics,
Faculty of Science,
Mbarara University of Science and Technology.

Signature: _____

Date: 17/09/2024

Dedication

To my late grandfather John Othieno.

Acknowledgement

First and foremost, I would like to express my profound gratitude to God, whose grace and blessings have provided me with the strength, wisdom, and perseverance to complete this thesis. Without His guidance, this journey would not have been possible.

I am deeply indebted to my supervisors, Assoc. Prof. Edward Jurua and Dr. Geoffrey Andima, for their invaluable guidance, and constructive feedback throughout the course of this research. Their expertise, patience, and encouragement have been instrumental in shaping this thesis, and I am truly grateful for their mentorship.

I would also like to extend my sincere thanks to my sponsors, the Swedish International Development Cooperation Agency (SIDA), through the International Science Programme (ISP) of Uppsala University in Sweden, whose generous financial support made this research possible. Their commitment to funding academic research is deeply appreciated, and their contributions have been crucial in the successful completion of this work.

I am also grateful to the Crustal Dynamics Data Information System (CDDIS) of the International GNSS Services (IGS) that provided access to the GPS observation data online.

I am profoundly grateful to my beloved wife and my wonderful children. Their unwavering support, patience, sacrifices, and love have been my constant source of strength in this journey.

I am very grateful to my brothers, sisters and friends for their constant encouragement, and understanding. Their sacrifices have been my motivation.

In a special way, I acknowledge my late grandfather John Othieno, who believed that one could only be considered truly learned if he/she holds a doctorate degree or the title of Doctor. His faith in the power of education and constant encouragement was my greatest motivation.

Finally, I would like to acknowledge the staff of department of physics, Mbarara University of Science and Technology together with my colleagues from the entire Faculty of Science, Technology and Innovations of Mountains of the Moon University, for creating a stimulating and supportive academic environment. Their assistance, feedback, and camaraderie greatly enriched my research experience.

Contents

Declaration i

Approval ii

Dedication iii

Acknowledgement iv

Contents v

List of Figures ix

Abbreviations and Acronyms xi

Abstract xiii

Publications xiv

1 Introduction 1

1.1 Background 1
1.2 Problem Statement 4
1.3 Aim of the Study 4
1.4 Objectives of the study 4
1.5 Scope 5
1.6 Significance 5

2 Theory and Literature Review 6

2.1 Introduction 6
2.2 The Ionosphere 6
2.2.1 Geomagnetic Regions of The Ionosphere 6
2.2.2 Ionospheric Layers 8
2.2.3 Ionospheric Anomalies 9
2.2.4 Ionospheric Variations 10
2.2.4.1 Ionospheric Regular Variations 11
2.2.4.2 Ionospheric Irregular Variations 11
2.2.5 Electromagnetic Wave Propagation in the Ionosphere 13
2.3 Ionospheric Instrumentation 15
2.3.1 Ionosondes 15
2.3.2 Global Navigation Satellite System 17
2.4 Global Positioning System 18
2.5 Total Electron Content 19
2.5.1 Measurement of Total Electron Content 20

2.5.1.1 TEC From GNSS 20
2.5.1.2 TEC From Ionosonde 22
2.6 Swarm Satellite Mission 22
2.6.1 Swarm Satellite Instrumentation and Measurements 23
2.6.1.1 Instrumentation 23
2.6.1.2 The Langmuir Probes of the SWARM Electric Field Instrument 23
2.6.1.3 The GNSS Receivers of Swarm 24
2.6.2 Swarm Measurements 24
2.6.2.1 Level-1b products 24
2.6.2.2 Level 2 products 26
2.6.2.3 Level 2 -TEC 27
2.7 Ionospheric Models 29
2.7.1 Physics Based Models 29
2.7.1.1 Thermosphere-Ionosphere-Electrodynamics General Circulation Model 29
2.7.1.2 Coupled Thermosphere Ionosphere Model 29
2.7.1.3 Utah State University-Time Dependent Ionospheric Model 30
2.7.1.4 Semi-Analytical Model of the Ionosphere 2 30
2.7.1.5 Semi-Analytical Model of the Ionosphere 3 31
2.7.1.6 Field Line Inter-hemispheric Plasma model 31
2.7.1.7 Global Ionosphere-Thermosphere Model 32
2.7.2 Empirical and Semi-empirical Models of the Ionosphere 32
2.7.2.1 International Reference Ionosphere 32
2.7.2.2 NeQuick 32
2.7.2.3 Consultative Committee for International Radio Model 33
2.7.2.4 Bent Ionospheric Model 33
2.7.2.5 The Thin Layer model 33
2.7.2.6 Klobuchar Model 34
2.7.2.7 Semi Empirical Low-latitude Ionospheric Model . . . 34
2.7.2.8 Fully Analytical Ionospheric Model 35
2.7.2.9 Parameterised Real-time Ionospheric Specification Model 35
2.7.3 Data Assimilation Models 35
2.7.3.1 Kalman Filter and Ensemble Kalman Filter 35
2.7.3.2 3DVAR and 4DVAR 36
2.7.4 Data assimilated in ionospheric models 36
2.7.4.1 GPS Radio Occultation 36
2.7.4.2 Incoherent Scatter Radar 36
2.7.4.3 Machine Learning-Assisted Assimilation: 37

2.7.5 Artificial Intelligence Models of the Ionosphere 37
2.7.5.1 Artificial Neural Networks 37

3 Materials and Methods **39**
3.1 Introduction 39
3.2 Data sources 39
3.3 Methods 42
3.3.1 Effective Height from Ionosondes 42
3.3.2 Estimation of Effective height using GNSS-TEC 42
3.3.2.1 The Inversion Technique 44
3.3.2.2 Coinciding Pierce Point Technique 46
3.3.2.3 Determination of the IPP altitude from IGS-GIMs . . 48
3.3.2.4 Comparison of zenith sTEC with oblique sTEC 49
3.3.3 Swarm-IRI TEC Technique 50
3.3.3.1 Determination of Effective Eeight from Swarm - IRI TEC 50
3.4 Spatial and Temporal Variation of the Effective Height. 51
3.4.1 Diurnal variation 51
3.4.2 Seasonal variation 52
3.4.3 Spatial Variation of Effective Height 52
3.5 Modelling of Ionospheric Effective Height over East Africa 52
3.5.1 Artificial Neural Networks Model 55

4 Results and Discussions **57**
4.1 Introduction 57
4.2 Determination of Effective Height of the Ionosphere 57
4.2.1 Effective Height from Ionosonde 57
4.2.1.1 Effective Height from Addis Ababa Ionosonde 57
4.2.1.2 Effective Height from Malindi Ionosonde 60
4.2.2 Effective Height from GNSS-TEC Techniques 62
4.2.2.1 Inversion Technique 65
4.2.2.2 Coinciding Pierce Point Technique 68
4.2.2.3 Zenith - Oblique Single Epoch sTEC Technique 70
4.2.2.4 IGS-GIMS Technique 72
4.2.2.5 Swarm-IRI Technique 73
4.3 Spatio-Temporal Variations of Effective Height Over East Africa 79
4.3.1 Diurnal Variation of Efective Height 79
4.3.2 Seasonal Variation of Effective Height 81
4.3.3 Spatial Variation of Effective Height 85
4.4 Effective Height Model for East African Region 86
4.4.1 Model Input Selection 86
4.4.2 Artificial Neural Network Model 86

4.4.2.1 Optimization of ANN Nodes 87
4.4.3 Validation of the Model 88
4.4.4 Comparison of the ANN model with IRI 89

5 Conclusions and Recommendations **91**
5.1 Conclusions 91
5.2 Recommendations 91

References **92**

List of Figures

2.1 Geomagnetic regions of the ionosphere 7
2.2 Sample ionogram from Addis Ababa, Ethiopia for 29^{th} July 2014 at 09:00:06 17
2.3 Side-view of instrumentation on the Swarm satellites. The satellite flies with the boom trailing at the rear. 23
2.4 Example illustrating the filename of the Swarm-A Level-1b low-rate magnetic product MAGx LR from 23^{th} February 2013 25
2.5 Geometry of the thin shell model 34

3.1 Locations of the ground based receivers used in this study 40
3.2 Geometry for the estimation of the mapping function (MF) 43
3.3 Schematic diagram showing the variation of oblique factor (χ) for the two different heights (h_s and h_s^I) 44
3.4 Geometry for estimation of mapping function error 46
3.5 Summary of steps followed to determine ionospheric effective height using the coinciding pierce point technique 48
3.6 Geometry for effective height determination from Swarm satellite and ground receiver 50

4.1 The variation of the ionospheric height with frequency at different times of DoY 156. Time indicated on each panel is the epoch of the ionograms. The curves are asymptotic at particular frequencies (critical frequency) corresponding to the hmF2. 58
4.2 Values of hmF2 recorded at the Addis ababa for the different epochs on DoY 157 panel (a), DoY 161 (b), DoY 162 (c) and DoY 166 (d). The mean of hmF2 values for a given day is represented by h, and printed at the center of each panel. 60
4.3 Variation of AIS ionosonde values of hmF2 with time of the day in 2023. 61
4.4 Visibility duration of all the satellites at the station MBAR on DoY 5 . 63
4.5 The effect of elevation angle on mapping function and vTEC. 64
4.6 Scatter plot of slant TEC vs vTEC for the different epochs over station MAL2 66
4.7 Comparison of height obtained from the Addis Ababa ionosonde and inversion technique at 13:00 UT, for selected days in 2014 67
4.8 Variation of vTEC error with IPP height using station pair MAL2-RCMN 69
4.9 Relationship between number of coinciding pairs with IPP height chosen over MAL2-RCMN station pair. 69
4.10 Sample results for the days of the year 2016 (004, 012, 015 and 021) from station MAL2 using single epoch technique. The red horizontal line is the vTEC for the Zenith satellite. 71

4.11 Comparison of height got from Addis Ababa ionosonde and zenith - oblique single epoch technique in 2014 72
4.12 Variation of ionospheric height with rmse of the two vTEC values for different days. 73
4.13 Comparison of TECbs obtained from Swarm B and MAL2 with IRI TEC for 122 points of all the epochs when swarm B passes over MAL2 in 2016. The rsme = 18.4901 TECu 74
4.14 Variation of ionospheric height h obtained using SWARM-IGS technique with vTEC. 75
4.15 Swarm-IRI technique values of effective height at a given hour for particular days of 2014. 76
4.16 Scatter Plot Showing the Correlation Between AIS hmF2 and effective height obtained by Swarm-IRI technique over MAL2 in Sept 2023 . . . 78
4.17 The ionospheric effective height obtained by the different methods. . . . 79
4.18 Diurnal variation of effective height of the ionosphere 80
4.19 Diurnal variation of hmF2 from ionosonde for two given days 81
4.20 Variation of hourly mean of hmF2 with time of the day for the different months. 82
4.21 Seasonal variation of effective height with DoY. 83
4.22 Seasonal dependence of effective height of the ionosphere for station pair MAL2-RCMN 84
4.23 Day by day variation of effective height 84
4.24 Variation of C2T with the time of the day. 85
4.25 rmse between training/validation data set and the respective predicted number of neurons when hidden layers are kept constant 87
4.26 An illustration of the final architecture adopted for the neural network model. 88
4.27 Diurnal variation of observed and modeled hmF2 of the AIS ionosonde measurements 89
4.28 Comparison of the diurnal variation between model predicted values of hmF2 and values from both ionosonde and IRI 90
4.29 Variation of rmse between IRI and predicted values 90

Abbreviations and Acronyms

CODE Centre for Orbit Determination in Europe

CTIM Coupled Thermosphere Ionosphere Model

AIS Advanced Ionospheric Sounder

ANNs Artificial Neural Networks

BDS BeiDou Navigation Satellite System

CCIR Consultative Committee for International Radio

CDAAC COSMIC Data Analysis and Archive Center

CTIPe Coupled Thermosphere Ionosphere Plasmasphere electrodynamics model

COSMIC Constellation Observing System for Meteorology, Ionosphere & Climate

DCB Differential Code Biases

DGPS differential GPS

EGNOS European Geo-stationary Navigation Overlay Service

EIA Equatorial Ionization Anomaly

ESWua Electronic Space Weather upper atmosphere

EUV Extreme Ultraviolet

EIA Equatorial Ionization Anomaly

EnKF Ensemble Kalman Filter

FAIM Fully Analytical Ionospheric Model

FLIP Field Line Interhemispheric Plasma

GAGAN GPS Aided Geo-Augmentation Navigation

GIMs Global Ionospheric Maps

GITM Global Ionosphere-Thermosphere Model

GLONASS GLObalnaya NAvigatsionnaya Sputnikovaya Sistema

GNSS Global Navigation Satellite System

HWM Horizontal Wind Model

IMF Interplanetary Magnetic Field

INGV Istituto Nazionale di Geofisica e Vulcanologia

IGRF International Geomagnetic Reference Field

IGS International GNSS Service

IRNSS Indian Regional Navigation Satellite System

IPP Ionospheric Pierce Point

ITEC Ionosonde Total Electron Content

IRI International Reference Ionosphere

MSAS MTSAT Satellite-based Augmentation System

MSIS-86 Mass Spectrometer and Incoherent Scatter - 1986

NASA National Aeronautics and Space Administration

NCAR-HAO National Center for Atmospheric Research High-Altitude Observatory

NRL Naval Research Laboratory

NRLMSIS Naval Research Laboratory Mass Spectrometer Incoherent Scatter

PDGS Swarm Processing and Data Archiving Ground Segment

PNT positioning, navigation and timing

PRISM Parameterised Real-time Ionospheric Specification Model

PPS Precise Positioning Service

SCARF Swarm Core Algorithm Research Facility

SLIM Semi Impirical Low-latitude Ionospheric Model

SLM Single Layer Model

sTEC slant TEC

SPS Standard Positioning Service

SAMI2 Semi-Analytical Model of the Ionosphere 2

SAMI3 Semi-Analytical Model of the Ionosphere 3

TEC Total Electron Content

TIE-GCM Thermosphere-Ionosphere-Electrodynamics General Circulation Model

TIIL Thermal Ion Imager and Langmuir probe

US DoD United States Department of Defence

URSI International Union of Radio Science

UV Ultraviolet

USU-TDIM Utah State University-Time Dependent Ionospheric Model

vTEC vertical TEC

VIPIR Vertical Incidence Pulsed Ionospheric Radar

WAAS Wide Area Augmentation System

QZSS Quasi-Zenith Satellite System

Abstract

The centroid of mass of the ionosphere lies in the region that contains the highest concentration of electrons. The height from the Earth's surface to the point where the centroid is located is called the effective height of the ionosphere. The effective height is useful for aspects such as mapping the Total Electron Content (TEC) over a given region, calibration of Global Navigation Satellite System (GNSS) observations, and satellite navigation augmentation among others. Due to the heterogeneous nature of the ionosphere, the effective height varies from one place to another. This variation is particularly pronounced in the low-latitude regions which have high electrodynamic activity. The high electrodynamic activity may render the value of the effective height used in most models and algorithms unsuitable for the low latitude region, particularly the East African region. In this study, the 350 km effective height of the ionosphere used in many ionospheric algorithms was validated for the East African region. This was determined using data from GNSS receivers and Ionosondes in the region. Another technique that utilizes the GNSS receivers aboard the swarm satellites was introduced to supplement the existing GNSS-TEC methods. The results show that the effective height over the East African region lies in a range of 350 km to 500 km, with a modal value of 400 km. The effective height of the ionosphere exhibit temporal variations, where the day-time values are higher than the night-time values, with the peak appearing between 09:00 UT and 16:00 UT. The seasonal variation showed slightly higher values in the equinox months than in the solstice months. The spatial variation of the effective height shows an asymmetry between the trough and the crest of the anomaly region, with higher values at the equator during the day-time and vice versa at night. The model predicted values of effective height were validated against the height of the peak electron density (hmF2) obtained from ionosondes for the month of April 2024. The predicted values are in good agreement with the measured values, and performed slightly better than International Reference Ionosphere (IRI) values especially in the day-time ionosphere. The good agreement between the predicted values and observations suggest that the model may be used to predict the effective height over a place in the East African region where observations are not available. The results showed that while the value of 350 km can still be used for the nighttime ionosphere, the most appropriate value for the East African region is 400 km.

Publications from this thesis

Two papers have so far been published from the work presented in this thesis. These are the details of the papers.

1. **Opio Phillip**, Andima, G., & Jurua, E. (2023). Characterization of the effective height of the ionosphere using GPS data over East Africa, a low latitude region. Advances in Space Research, 71(12), 5196-5207. https://doi.org/10.1016/j.asr.2023.0

2. **Opio Phillip**, Uwamahoro, J. C., Andima, G., and Jurua, E. (2024). Comparative analysis of the GNSS-TEC methods for determining effective height of the ionosphere. Advances in Space Research. https://doi.org/10.1016/j.asr.2024.07.022

Chapter 1: Introduction

1.1 Background

The refractive ability of the ionosphere causes signals propagating through it to be slightly delayed (Houminer and Soicher, 1996; Birch et al., 2002; Li et al., 2017). The delay suffered by a signal is a useful phenomenon that currently enables Scientists to estimate the integral number of electrons in a square meter column from the satellite to the receiver, referred to as the Total Electron Content (TEC) (Ma and Maruyama, 2003; Li et al., 2017). Global Navigation Satellite System (GNSS) transmits signals at different frequencies: L1, ranging from 1,559 to 1,610 MHz to accommodate all constellations, L2 ranging from 1,215 to 1,300 MHz, and L5 ranging from 1,598 to 1,609 MHz (Hegarty, 2012). For the dual frequency GNSS receivers, two of the signals L1 and L2, are analyzed by ground receivers to measure the carrier phase and pseudorange. The difference in travel time between the signals transmitted at these two frequencies is determined to estimate the ionospheric delay, which is then translated into TEC (Arikan et al., 2016; Seemala, 2023). Several techniques have been employed to clean the derived TEC from both the satellite and receiver biases, with the most common being Grid method (Ma and Maruyama, 2003; Li et al., 2017), Kalman filtering method (Acharya et al., 2009; Muslim et al., 2019), polynomial method (Ya'acob et al., 2009; Osei-Poku et al., 2021), and the method of minimisation of standard deviation of VTEC for a single station (Ma and Maruyama, 2003; Seemala, 2023).

The measured TEC from the satellite to the receiver, called slant TEC (sTEC), is often converted in to vertical TEC (vTEC). The vTEC is useful in estimating the adjustment needed to compensate for the ionospheric delay, commonly referred to as correction factor. This factor is calculated for the GNSS receivers, especially for single frequency type, through augmentation system (Komjathy et al., 2012; Juan et al., 2004; Krankowskia et al., 2009). The conversion of sTEC is achieved with the help of a mapping function that depends on the effective height of the ionosphere, or the thin shell in the Single Layer Model (SLM) (Klobuchar, 1987b). The altitude of the shell above the GNSS ground receiver greatly influences the measured value of TEC due to the spatial and temporal variation of the electron content (Huang et al., 2011; Li et al., 2017). In addition, the thin shell ionospheric model, which is also called SLM helps in calibration of the GNSS observations by removing the inter frequency biases, known as the Differential Code Biases (DCB). The DCB originate in both the satellite and receiver hardware (Brunini et al., 2011).

The SLM assumes a thin layer above the Earth's surface at the altitude of the ionospheric mass centroid or effective height. The ionospheric mass centroid is the point in the F2 layer of the ionosphere where the centre of gravity of the ionosphere lies (Gulyaeva et al., 2021), and the height from the Earth's surface to this point is called

the effective height of the ionosphere. This height is also considered as the height of the Ionospheric Pierce Point (IPP), which is a point in the ionosphere where the vertical line above the user intersects with the direct line of sight from the satellite to the user (Rao et al., 2006). Other uses of ionospheric effective height are to compare the sTEC received from satellites when at different elevation angles (Ya'acob et al., 2010), map TEC over the globe, e.g the Global Ionospheric Maps (GIMs) products (Hernández-Pajares et al., 2017), argumentation (Nava et al., 2007), and calibration of the GNSS observations (Brunini et al., 2011).

Earlier studies, e.g ionospheric corrections for GPS systems in North America (Klobuchar, 1987a), a review of ionospheric models and empirical data (Davies, 1990a), and the Bent ionospheric model developed and used extensively for GPS ionospheric correction studies (Bent et al., 1972), considered an effective ionospheric height of approximately 350 km. Other studies, e.g (Lanyi.G, 1986; Coco et al., 1991; Wilson and Mannucci, 1993; Sardón et al., 1994), all conducted in mid-latitude, recommended a height of 350 km to be a suitable value of the effective height of the ionosphere (Wang et al., 2024).

However, because the ionosphere varies with location on Earth and with the time of day or season (Forbes et al., 2000), the 350 km altitude used in the SLM, drawn primarily from studies in mid-latitude regions, may not be consistent or optimal for all regions. More studies conducted in various locations have uncovered differing values. For example, a value of 400 km has been suggested in the studies by Jakowski and Jungstand (1994) and Ciraolo and Spalla (1997) for Europe; and G.L.Goodwin (1992) for Australia. This disparity in the values of effective height obtained prompted more studies in several places around the world, where the findings have suggested a range of values rather than just a single value. For example, a study by Birch et al. (2002) in United Kingdom, located in the mid-latitude region, revealed a range of 750 km to 1200 km, which is way above the 350 km. Similarly, Nava et al. (2007) used GPS data from the Italian sector of the mid-latitude region, and suggested a value of 400 km and above.

In the recent years, numerous simulations have been conducted on the effective height of the ionosphere, and their results also illustrate variations. For example, Brunini et al. (2011), found a range between 340 and 410 km in South America, Guo et al. (2014) utilized a simulation based on the Global Core Plasma Model (GCPM), which encompassed data and analysis from various regions around the world to estimate the effective height. The study found that the optimal value of the effective height is 560 km during low solar activity periods, and 695 km during high solar activity periods. In the same way, Yang et al. (2014) simulated the effective height of the ionosphere using an International GNSS Service (IGS) station, DLFT found in Greece, together with the Klobuchar model (Klobuchar, 1987b), and suggested a range from 350 km

to 500 km to be suitable for Greece. Similarly, Wang et al. (2016) employed the grid method in the Chinese region to simulate the effective height of the ionosphere, and found that the value ranges from 350 km to 500 km. These variations in results may be associated with the differences in electrodynamics of different ionospheric regions (Richmond, 2017; Chen et al., 2021).

The ionospheric regions, such as the equatorial and low latitude areas where East Africa is located, present unique challenges due to several distinct phenomena (Ogwala et al., 2022). The ionosphere over low latitudes (within the $\pm 30^{o}$ latitude range) exhibits unique characteristics compared to other latitudes due to the low inclination of geomagnetic field lines, and the relatively higher amount of incident solar ionizing radiation in this region (Abdu, 2016). The Equatorial Ionization Anomaly (EIA) is one of the key features in this region, with two peaks of electron density approximately 15° North and South of the magnetic equator, driven by the eastward electric field and the fountain effect (Kelley, 2009). Other low latitude phenomena include, the equatorial electrojet, that modifies the current systems of the ionosphere over the low latitude regions (Reddy, 1989; Onwumechikli, 2019), equatorial Spread F (ESF) that involves irregularities in electron density, typically occurring after sunset with the post-sunset rise of the F region (Rao et al., 2006). These phenomena are associated to the changes in altitude or the centroid of ionization mass distribution in low latitude regions, which can cause high ionospheric perturbations that greatly modify its vertical structure including effective height (Li et al., 2017; Tang et al., 2021). This implies that the altitude for the peak electron density over East Africa, a low latitude region, could be significantly different both spatially and temporally compared to other regions.

Most research on the effective height of the ionosphere in the low latitude regions have been conducted in the Asian sector. These studies have shown that the values of the effective height of the ionosphere over the low latitude region are distinct. For example, Rao et al. (2006) investigated the effective height of the ionosphere for the Indian low latitude region, and found the value in the range from 275 km to 570 km. In another study in the low latitude region, Hu et al. (2014) focused on validating the peak electron density (NmF2) and the peak height (hmF2) of the F2 region of the ionosphere using data from the Constellation Observing System for Meteorology, Ionosphere & Climate (COSMIC) satellite and a chain of ionosondes in China. They observed that the effective height (hmF2) ranged from 250 km to 350 km. Li et al. (2017) found that the optimal ionospheric effective height for the Chinese region ranges from 400 to 600 km. Additionally, some studies in the Asian sector used different values of ionospheric effective height, e.g Cheng et al. (2021) used an effective height of 300 km around Taiwan in their statistical study of medium-scale traveling ionospheric disturbances. While these findings provide valuable insights, they may not be directly applicable

to the East African low-latitude region due to potential differences in ionospheric conditions between Asia and Africa.

The ionosphere in the low latitude regions of Africa and Asia exhibits several key differences. Geographically, Africa spans the geomagnetic equator, leading to more pronounced Equatorial Ionization Anomaly (EIA) effects, whereas Asia's geomagnetic distribution is more complex due to its larger landmass and varying geomagnetic declinations (Chen et al., 2008; Oyedokun et al., 2020). The ionospheric density, especially electron density, tends to be higher in Africa due to strong solar radiation and the EIA, leading to greater TEC values, whereas in Asia, electron density and TEC variations are influenced by more complex geomagnetic structures and local atmospheric conditions (Dugassa et al., 2020; Kayode et al., 2023).

However, for effective use of satellite technologies in the East African region for point to point communication, surveillance, Navigation (in cars, mobile phones, Google maps, Planes, Ship etc) and Mapping (for surveyors), the ionospheric errors on the GNSS signal in positioning that can extend even up to 10 meters have to be minimised (Doherty et al., 2003; Basu et al., 2002). This is done through fully characterising the ionosphere that contributes a percentage of this error. One such aspect to be characterised is the effective height of the ionosphere.

There are different values of ionospheric effective height being used in the different models of the ionosphere. This affects the characterisation of ionospheric layers, influencing the understanding of ionospheric behavior and its impact on communication systems. Further more, when integrating or comparing results from different models, discrepancies due to the varying effective heights can complicate analysis, highlighting the need for consistent values over particular regions.

1.2 Problem Statement

The ionospheric effective height value of 350 km that is being used to convert sTEC to vTEC in some analysis applications such as GPS-TEC analysis program, and some models used to map TEC over the world may not be suitable for the East African region.

1.3 Aim of the Study

To validate the value of 350 km effective height of the ionosphere for the low latitude region of East Africa.

1.4 Objectives of the study

The objectives of the study were to:

(i) Estimate the effective height of the ionosphere for East Africa, a low latitude region.

(ii) Determine the spatial and temporal variation of the ionospheric effective height over the East African low latitude region.

(iii) Model the effective height of the ionosphere for the low latitude region of East Africa.

1.5 Scope

The study focused on the ionospheric effective height, for the East African region. It used data from ionosondes and GNSS receivers in the East African region collected in 2014, 2016, 2021, 2022 and 2024. For 2024, the data used was from January to April.

1.6 Significance

This study has provided a range of values of the ionospheric effective height suitable for the East African region. This is useful in the region to refine ionospheric models, improve space weather forecasting, allow for tailored regional studies, and provide a basis for future augmentation system for East Africa.

Chapter 2: Theory and Literature Review

2.1 Introduction

This section presents theoretical background concerning the ionosphere, its basic formation and the relevant characteristics. The shell model, The ionosonde and the GPS as the major instruments for the measurement of the ionospheric parameters. Total Electron Content (Total Electron Content (TEC)) the indicator of the ionospheric compositions and variation, the effect of the ionosphere on signals, and ionospheric models.

2.2 The Ionosphere

The ionosphere which was initially termed as "Heaviside layer" by William Eccles around 1910, and "Appleton layer" by Watson-Watt in about 1924, is the partially ionized region of the Earth's upper atmosphere, which covers a height of 50 km above the Earth's surface to about 1000 km and completely encircles the Earth (Henry and Owen, 1969; Goodman, 2005; Griffiths, 2018). It is mainly caused by the Sun's Extreme Ultraviolet (EUV) and X-ray radiations, which ionize the neutral molecules of the gas in a process known as photoionization (Shim, 2009). In the polar regions, photoionization is supplemented by collision of the energetic particles with the neutral molecules (Schunk and Nagy, 2009; Shim, 2009; Bagiya et al., 2009). A chemical reaction then takes place between the ions created with the neutrals and the ions formed by the ionisation process. The same ions also recombine with electrons and diffuse latitudinal, or they are moved via neutral wind and electric fields due to magnetic field of the Earth. This results into non uniform distribution of the ionosphere (Memarzadeh, 2009). The spatial coverage of the ionosphere has been categorised geographically and geomagnetically into regions.

2.2.1 Geomagnetic Regions of The Ionosphere

The electron density profile of the ionosphere also depends greatly on the geomagnetic latitude. Therefore, the ionosphere is divided into three broad latitudinal regions whose properties and features differ greatly from each other (Shim, 2009). The regions are: the high latitude (polar or Auroral) regions, Mid-latitude and Low latitude regions.

The Low Latitude Region

This is a region about 30° South or North of the magnetic equator. It is the region containing the dip equator where the magnetic field lines of the Earth are horizontal and therefore the magnetic drift together with plasma fountain, results in high variability of the electron density, this makes modeling and characterizing ionosphere of this region

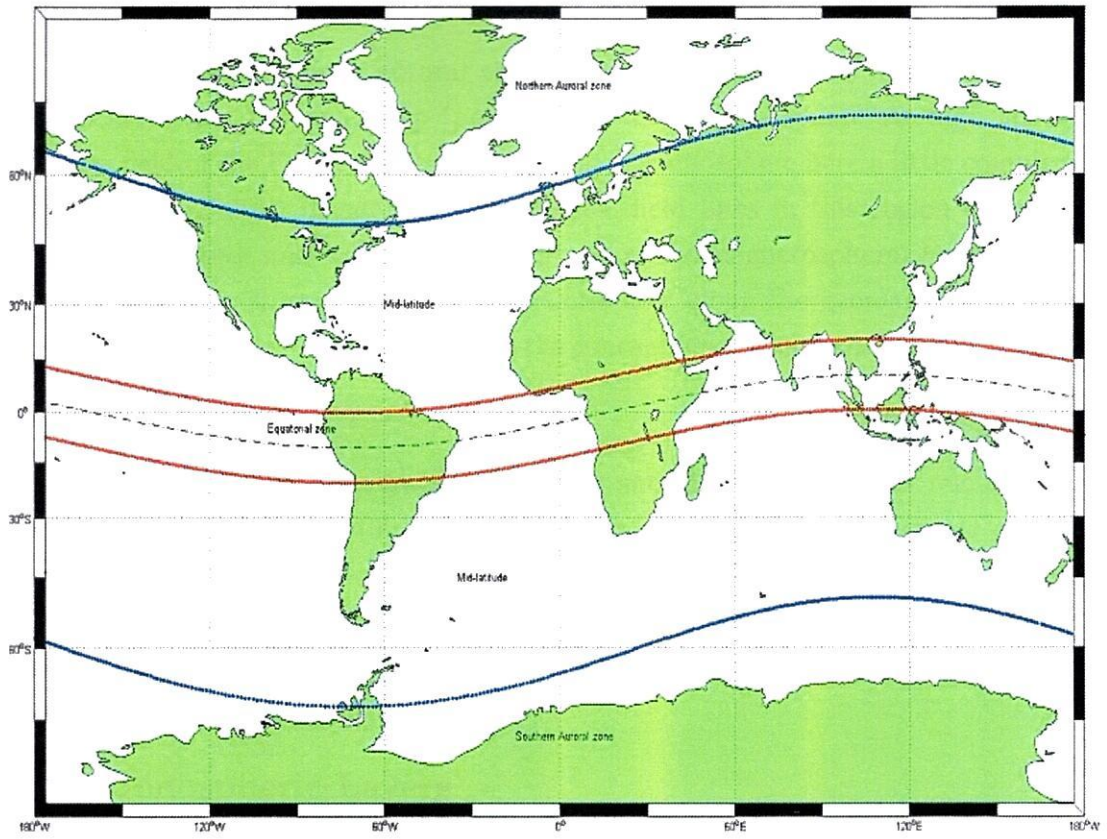


Figure 2.1: Geomagnetic regions of the ionosphere (Memarzadeh, 2009).

complicated. Some studies have been carried out in this region especially in Asia and American sector, with little in the African sector. Therefore, this study covers the low latitude zone particularly for the East African sector that covers the area shown in Figure 2.1.

Mid-Latitude Region

This region includes magnetic latitudes of the Earth from about 20^o to 60^o on both sides of the geomagnetic equator. It is the region that is free from direct influence of plasma fountain of the low latitude region, making it the best understood of all regions (DasGupta et al., 2007). The mid latitude ionosphere is believed to be connected to the inner magnetosphere that rotates with the Earth, and is therefore not much affected by the external influence. According to Norsuzila et al. (2008), the day to day changes in the ionosphere layers for mid latitude show regular variations, which is the reason why most of the first ionospheric observations were made in it. The process of ionisation depends on solar photon radiation and the electron density is not much affected by particle radiation in general (Schunk and Nagy, 2009).

High-Latitude (polar) Regions

The region constitutes both auroral zone (approximately 60^o -70^o magnetic latitudes of the Earth) and the polar cap (poleward of the auroral zone). At high latitudes, magnetic field of the Earth are vertical making the ionosphere here a little complicated (Memarzadeh, 2009). In addition, the vertical field lines in this region connect the auroral regions with solar wind driven outer part of the magnetosphere. For this reason, during a magnetic storm the charged particles flow along the geomagnetic field lines and interact with ions and electrons in the ionosphere causing the aurora (Moldwin, 2008).

Similarly the ionosphere coverage in space is sub-divided into three regions: lower or bottom-side ionosphere (50 km to about 90 km that consist of the D layer and some E layer), the mid ionosphere (90 km to about 400 km having E and F layers), and topside ionosphere (400 km to about 1000 km). These three regions contain the electrons concentration of varying extent which constitute the different layers of the ionosphere (Habarulema, 2010).

2.2.2 Ionospheric Layers

The lower and bottom-side layer contain highest concentration of electron density and this varies slowly with altitude. The variation led to sub-division of these two regions into ionospheric layers, namely: D, E, and F layers (Hunsucker and Hargreaves, 2003). The layers are as a result of photoionization and they vary with time of the day, solar activity and season (Goodman, 2005).

D- Layer

This is the lowest layer of the Earth's ionosphere that covers about 60 to 90 km (taking care of the C-layer that lies in the altitude of about 50 - 60 km caused by the galactic cosmic rays) (Habarulema et al., 2013). It is where the heavy components of the ionosphere dominate, such as the neutral molecular gases of N_2 and O_2 (DasGupta et al., 2007). As the Sun's radiation traverse the atmosphere, some components of the radiation such as X-rays and Ultraviolet (UV) are absorbed in the upper atmosphere during ionisation and the components that are able to go through all the layers play a role in the D-region formation (Kelley, 2009). This makes the region to have a low electron density compared to other regions by existing only during day time and disappears at night (Liu et al., 2006). Important to note is that, the vertical profile of the electron density in the D- layer does not have a typical maximum (Hunsucker and Hargreaves, 2003). The molecules in the D-layer are more influenced by gravity compared to those in the upper layers, and their free electrons re-attach easily to the molecules accounting for its electron loss. Because it exhibits much lower electron densities, then its contribution to the TEC within the ionosphere is negligible.

E- Layer

This is the second layer of the Earth's ionosphere which extends from 90 km to about 120 km or 140 km depending on the equatorial, or mid-latitude, or polar regions of the ionosphere. The molecular positive ions of the di- atomic gases, O_2^+ and NO_+, dominate the region (Komjathy, 1997). These ions can survive even at night compared to that of the D- layer, making the E-region to be relatively stable than other regions of the ionosphere, with a behaviour that is characterized by the solar zenith angle and solar activity (Kelley, 2009; Goodman, 2005). The loss of ions in this region is through direct dissociative recombination, and the rate of loss varies linearly to the electron density, and that is why one can say that the E-region is created under photochemical equilibrium, i.e ion disappearance rate is balanced by the ion production rate) (Memarzadeh, 2009).

F- Layer

This is the last layer as one tends toward the topside part of the ionosphere and covers between 120 km and 400 km of altitude but can extend to altitudes as high as 500 km or more (Zhang et al., 2000). According to McNamara (1991), the formation of the F-layer is majorly by ionizing atomic oxygen (O), a process described in Lyman continuum or emission lines of helium (He). During the day, the F-layer is divided into F_1 and F_2 especially at the equatorial region and during summer of the other regions. The F_1 layer tends to have a peak of about 200 km and disappears in the ionosphere mainly by a process known as dissociative recombination.

The F_2-layer has the longest life time as it can exist during the day with a very high concentration of electrons even up to the order 10^6 cm^{-3} peaking at a height of about 450 km or more in the local noon and can survive even in the night (Hysell, 2020). This makes it the most important layer for High Frequency (HF) propagation due to its ability to reflect even slightly higher frequencies. The F_2-layer is the most variable and the most irregular, bringing about the anomalies exhibited by the ionosphere (Millward et al., 1996).

2.2.3 Ionospheric Anomalies

There are three common ionospheric anomalies, namely:

Diurnal Anomaly

This is when the maximum value of the F_2-layer occurs at other time of the day that is not the local noon as it was earlier predicted by the Chapman theory (Goodman, 2005). The Earth-Sun geometry for a given day causes a variation in the amount of ions produced. The maximum electron density is expected to occur at noon time when

the zenith angle of the Sun is about 0^o. Similarly, the upper atmosphere temperature tends to maximise around local noon where the ionospheric ion density is expected to reach its maximum in the same time (Shim, 2009; Moldwin, 2008). However, there are some days when the ionosphere exhibits a semidiurnal component producing two maxima about the local noon, giving an appearance of a slight minimum at the local noon commonly referred to as the midday "bite-out" (Saryo et al., 1989; Cherniak et al., 2014).

Seasonal Anomaly

During certain solar periods, the value of the F_2-layer peak electron density that occurs at local noon tends to be higher in winter than in summer, which is opposite of the expected Chapman theory. This phenomenon is regarded as "seasonal anomaly" in the F_2-layer. This seasonal anomaly is attributed to the fact that, the ratio between the molecular components and atomic components at the F_2-layer changes. This brings about the changes in recombination and ion production rate (Hunsucker and Hargreaves, 2003; Hawk, 2001).

Equatorial Anomaly

Around the magnetic equator of the Earth, the magnetic field line is horizontal and there is a day time eastward electric field and westward field during the night (Moeketsi et al., 2005; Bagiya et al., 2009). The two orthogonal fields create an upward force resulting into a plasma lift referred to as $\vec{E} \times \vec{B}$ drift. During this phenomenon, the plasma around this region move upwards to a peak height and then later diffuse downwards along magnetic field lines, to low altitudes on both sides of the Earth's magnetic equator by gravity and the plasma pressure gradient (Malik et al., 2010; Bagiya et al., 2009). This creates a depletion of electron concentration around the magnetic equator, and a concentration enhancement in two regions, found around 15^o North or South of the magnetic equator, called EIA crests. This feature also termed as Appleton anomaly has a unique and pronounced effect on the ionospheric F_2-layer of low latitude due to the combination of higher altitude, strong and horizontal geomagnetic fields, lower collision rates, and the high plasma density found at these altitudes (Pavlov, 2008).

2.2.4 Ionospheric Variations

The variations of the ionosphere can be categorised into two; those that directly depend on the Sun's activity or its radiation intensity (regular variations), and those that indirectly depend on the Sun (irregular variations) (MacDougall et al., 2009; Wang et al., 2008).

2.2.4.1 Ionospheric Regular Variations

These are ionospheric variations that entirely depend on the Sun. They include:

Diurnal variation

This is the variation with the time of the day, where by, after local mid-night the electron density is least, and the values rise gradually to a peak around the local noon (highest ionisation by the Sun) after which it gradually falls to a minimum again after mid-night (greatest recombination) (Rishbeth and Mendillo, 2001).

Solar activity variation

The ionosphere varies with solar activity, which is measured by the Sunspot numbers and the solar radio flux index (F10.7). The Sunspot numbers exhibit 11-year solar cycle, having a solar maximum and a solar minimum with very high electron density and very low electron density, respectively.

Latitudinal variation

The continuous change in zenith angle of the Sun over different latitudes, leads to a varying extent to the radiation intensity traversing the ionosphere of different latitudes. This in turn causes a variation in electron production, where by ionization reduces as one ascends the latitude during summer of each hemisphere (McNamara, 1991). In general, the latitudinal variation of the ionosphere is influenced by four major parameters: solar radiation, geomagnetic field effects, seasonal effects and ionospheric disturbances (Chernigovskaya et al., 2021).

Seasonal variation

The Earth-Sun rotation brings about the Sun lying overhead a particular hemisphere of the Earth (summer) at a particular time. This leaves the other hemisphere of the Earth tilted away from the sun (winter). Winter in one hemisphere corresponds to summer in the other. During the summer period, the peak value of electron density is expected to be high, compared to the values during winter. However, in some cases this may not be the case because of varying composition of neutrals bringing about the seasonal anomaly (McNamara, 1991; Meggs et al., 2006). Similarly, when the Sun is directly over the equator (equinox), there is near-equal distribution of solar radiation across both hemispheres leading to increased ionization of the equatorial ionosphere.

2.2.4.2 Ionospheric Irregular Variations

These are random ionospheric variations that do not depend on the Sun directly. The common ones include; sudden ionospheric disturbances, spread F, sporadic E and

ionospheric storms, or geomagnetic storms variation.

Geomagnetic storm variation

When a geomagnetic storm occurs, the ionospheric electron density is characterised by either an increase (positive effect) or a decrease (negative effect), that may depend on the strength of the storm, the latitude etc. A geomagnetic storm is the moment when the Sun releases charged particles from its corona that move across geomagnetic field generating new ionospheric current. The additional currents in the ionosphere create another magnetic field within the ionosphere that keeps on varying (Moldwin, 2008).

Sporadic E

Sporadic E may be taken as clouds of plasma suspended within the E layer. It involves random formation of varying electron concentration in the E region. This may lead to E-layer reflecting frequencies meant for the F layer by the radiosonde. In low and mid-latitudes, the phenomenon is common during day more especially in summer, whereas for high latitudes, its common during the night. Sporadic E-layer may also be caused by other atmospheric parameters such meteor showers, thunderstorms (Arras, 2010). In addition, sporadic E-layers are also formed via the interaction between neutral wind and magnetic field vectors, commonly referred to as $\vec{V} \times \vec{B}$ or "windshear" mechanism (Whitehead, 1989).

Spread F

Ionospheric spread F is a night-time phenomenon predominantly in the F region of equatorial and low-latitude regions and are more pronounced at equinoxes. It creates irregularities that may be in the form of plasma bubbles, depletion, or blobs in the ionosphere, causing the electron density to vary significantly over short distances. It manifests by scattering of the radio wave or reflection of the waves. This event can either be frequency spread or range spread (Davies, 1989; Whitehead, 1989). Some of the studies attribute the mechanism of spread F to post-Sunset rise, where the rapid recombination of ions in the lower ionosphere after Sunset leads to a steep vertical gradient in electron density, known as the evening pre-reversal enhancement (PRE) that triggers Rayleigh-Taylor instabilities, causing the formation of plasma bubbles that rise through the ionosphere (Hysell, 2020). In addition, gravity waves and tides in the lower atmosphere propagate upward and interact with the ionosphere, seeding instabilities leading to spread F (Fritts et al., 2008).

Ionospheric variation significantly influences electromagnetic wave propagation by changing the density and distribution of ionized particles in the ionosphere (Quan et al., 2021). These variations, caused by factors discussed in section 2.2.4 affect how electromagnetic waves, travel through the atmosphere. As the electron density in the

ionosphere fluctuates, the signals propagating can be refracted, reflected, absorbed, or scattered. This can result in signal distortion, delay or enhance signal transmission through the ionosphere. Conversely, the ionosphere can enable Electromagnetic signals to reach by reflecting radio waves over longer distances (Davies, 1989).

2.2.5 Electromagnetic Wave Propagation in the Ionosphere

The ionosphere delays radio waves travelling through it by refraction and dispersion (Yeh and Liu, 1982; Rino, 2011). In a similar way, GPS signals passing through the ionosphere will suffer from dispersion. The delay a signal experiences in the ionosphere and the phase advance can be put in perspective by discussing the magnetic and ionic theory involved with ionospheric radio propagation. Edward Appleton and Douglas Hartree in the early 1930's described the medium of the ionosphere with a dispersion equation of the refractive index μ of the ionospheric medium (Davies, 1990b).

$$\mu^2 = 1 - \left[\frac{\mathrm{R}}{1 - \mathrm{iT} - \left(\frac{\mathrm{S_Y^2}}{2(1-\mathrm{R}-\mathrm{iT})} \right) \pm \left(\frac{\mathrm{S_Y^4}}{4(1-\mathrm{R}-\mathrm{iT})^2 + \mathrm{S_X^2}} \right)^{\frac{1}{2}}} \right], \tag{2.1}$$

Where R, S and T are dimensionless quantities defined by the following expressions

$$R = \frac{\omega_p^2}{\omega^2},\ S = \frac{\omega_B}{\omega},\ T = \frac{\omega_e}{\omega},$$

and

$$S_X = \frac{\omega_X}{\omega} = \frac{\omega_B cos\theta}{\omega},\ S_Y = \frac{\omega_Y}{\omega} = \frac{\omega_B Sin\theta}{\omega},$$

where:

i	:	$\sqrt{(-1)}$
ω	:	Propagating wave angular frequency,
ω_p	:	Angular frequency of plasma,
ω_B	:	Gyro frequency of electron, $\omega_B = \frac{Be}{m}$
ω_X	:	Longitudinal component of ω_B ,
ω_Y	:	Transverse component of ω_B,
ω_e	:	Angular frequency of collision between heavier particles and electrons ,
θ	:	Angle between geomagnetic field and wave propagation direction,
B	:	Magnetic flux density

At high frequencies, the angular frequency due to collision were ignored, i.e. $\omega_e \approx 0$, making the T term to vanish (Davies, 1990b);

$$\mu^2 = 1 - \left[\frac{R}{1 - \left(\frac{S_Y^2}{2(1-R)} \right) \pm \left(\frac{S_Y^4}{4(1-R)^2 + S_X^2} \right)^{\frac{1}{2}}} \right] \tag{2.2}$$

Expanding Equation 2.2 into the fourth inverse frequency power (Komjathy, 1997) gives:

$$\mu^2 \cong 1 - \frac{1}{2}R \pm \frac{1}{2}RS|cos\theta| - \frac{1}{8}R^2 - \frac{1}{4}RS^2|1 + cos^2\theta| \tag{2.3}$$

According to Komjathy (1997), the 2^{nd} and 4^{th} terms depend on frequency and maximum electron density, whereas the 3^{rd} and 5^{th} terms depend on magnetic flux density of the Earth, electron density and frequency. Considering a wave moving at right angles to the magnetic field B, equation above reduces to (Komjathy, 1997);

$$\mu^2 = 1 - \left[\frac{R}{1 - \left(\frac{S_Y^2}{2(1-R)}\right) \pm \left(\frac{S_Y^2}{2(1-R)^2}\right)}\right] \tag{2.4}$$

The electromagnetic wave that is plane polarised is therefore divided into ordinary and extraordinary waves as represented by the following expressions

Ordinary wave: $\mu^2 \cong 1 - \left[\frac{R}{1-\left(\frac{S_Y^2}{2(1-R)}\right)-\left(\frac{S_Y^2}{2(1-R)^2}\right)}\right] \cong 1 - R$

For extra ordinary wave: $\mu^2 \cong 1 - \left[\frac{R}{1-\left(\frac{S_Y^2}{2(1-R)}\right)+\left(\frac{S_Y^2}{2(1-R)^2}\right)}\right] \cong 1 - \frac{R(1-R)}{1-R-S_Y^2}$

The profile of the propagated wave without the influence of magnetic field is approximated by the ordinary wave (Chen, 1984). Therefore ignoring the effects of the magnetic field and considering the refractive index μ, as complex ($\mu = n + i\chi$) (Langley, 2000; Langley et al., 2002), then both the ordinary and extraordinary wave expressions become the same:

$$\mu^2 = (n + i\chi)^2 \cong 1 - R$$

However, for a wave to propagate, then the the refractive index of the medium must be real, thus considering only the real part, the expression becomes

$$n^2 \cong 1 - R \text{ or } n \cong (1 - R)^{\frac{1}{2}}$$

By applying Binomial expansion and ignoring terms of R with higher powers

$$n \approx 1 - \frac{1}{2}R^2 = 1 - \frac{\omega_p^2}{2\omega^2}, \tag{2.5}$$

Where

ω_p: is the angular frequency of plasma given by: $\omega_P = 2\pi f_p$ or $\omega_p^2 = \frac{N_e e^2}{m\varepsilon_o}$

ω: is the radio wave angular frequency given by $\omega = 2\pi f$

Therefore, at frequency f the refractive index n, is given by

$$n \approx 1 - \frac{f_p^2}{2f^2} = 1 - \frac{N_e e^2}{8\pi^2 m\varepsilon_o f^2} \tag{2.6}$$

where N_e is electron density (per m^3), m rest mass of electron (9.11×10^{-31}), e electron charge (-1.602×10^{-19}C) and ε_o the permittivity of free space.

Substituting the above values in Equation 2.6, the refractive index of the phase advance reduces to

$$n_\phi = 1 - \frac{40.28 N_e}{f^2} \tag{2.7}$$

According to Komjathy (1997), the Appleton-Hartree magneto-ionic theory is applicable under the following assumptions:

(i) The mass of electron is less than the mass of ion implying that positive ions may have no effect on radio waves

(ii) The electrons in the ionosphere are oscillating with angular frequency f.

(iii) The ionosphere being the medium of propagation of electromagnetic wave is electrically neutral.

According to Langley (2000), expressing group refractive index n_g in terms of the phase refractive index n_ϕ gives:

$$n_g = n_\phi + f\frac{dm_\phi}{df} = n_\phi + \frac{80.56 N_e}{f^2} df \tag{2.8}$$

Putting Equation 2.7 in Equation 2.8, the group refractive index reduces to

$$n_g = 1 + \frac{40.28 N_e}{f^2} \tag{2.9}$$

From equations 2.7 and 2.9, it can be shown that the group and phase velocities, V_g and V_ϕ respectively, of the electromagnetic wave in the ionosphere depend only on its frequency (f) and electron density (N_e). i.e

$$\begin{aligned} V_\phi &= \frac{c}{n_\phi} = \frac{c}{1 - \frac{40.28 N_e}{f^2}} \\ V_g &= \frac{c}{n_g} = \frac{c}{1 + \frac{40.28 N_e}{f^2}} \end{aligned} \tag{2.10}$$

2.3 Ionospheric Instrumentation

The state of the ionosphere is observed and monitored by a number of instruments. Among these include: ionosondes, GNSS receivers, Incoherent scatter radars, Langmuir probes, Faraday rotation monitors, Radio occultation etc.

2.3.1 Ionosondes

Ionosondes are high frequency, vertically sounding radars that transmit radio waves vertically upwards above its antenna at different frequencies, ranging from about 0.1 to 30 MHz. The different frequencies of the signal are each reflected by the respective plasma density regions, whose echoes are detected by the receiver antenna installed within the same area. Ionosondes are of two types: the ionosonde that employs pulse

and the chirp ionosonde. The pulse ionosondes transmit strong pulses of approximately 100μs at a strong peak power of about 1 - 30 KW, that gives peaks as output in the time domain. On the other hand chirp ionosondes transmit a weak pulse of 0.5 - 1 seconds at a lower peak power (10 - 100 W), having peaks as outputs instead in the frequency domain (Davies, 1989).

Two ionosondes installed at the East African region by US DoD in collaboration with Boston college are special pulse type, known as Vertical Incidence Pulsed Ionospheric Radar (VIPIR), with unique features such as: very high interference immunity (IP3 > 40 dBm); High dynamic range of 115(1) + 30(V)dB; direct RF sampling of 14 bits at 80 MHz; fully digital conversion, receiver and exciter; wave form agility of $2\,\mu$s to 2ms pulse width; 8 coherent receiver channels of frequency range 0.3 - 25 MHz; 4 KW class AB amplifier of 3^{rd} harmonic (< -30 dBc) and an open source C code Radar software running under Linux (Habarulema, 2010).

The principle of operation of the ionosondes are based on the fact that plasma is a dispersive medium. According to Reinisch et al. (2005), the refractive index of the dispersive medium depends on the sounding frequency (f) and electron density N_e.

$$\mu^2 = 1 - \kappa\left(\frac{\mathrm{N_e}}{\mathrm{f^2}}\right) \tag{2.11}$$

The waves will not pass across the medium if the critical frequency of the radio waves (f_o) reaches the same value with the plasma frequency (f_p) where $\mu = 0$. This makes Equation (2.11) to become (Davies, 1990b).

$$\mathrm{f_p^2} = \kappa \mathrm{N_e}, \tag{2.12}$$

where by ε_o is permittivity of free space, e is electron charge, m is mass of electron. and $\kappa = \left(\frac{e^2}{4\pi\varepsilon_o m}\right) = 80.5$

The altitude from which the radiowaves are reflected is estimated by determining the virtual distance vertically, h^1, covered by the wave if it were continuing with the speed of light c in the ionized region for a time of flight τ

$$\mathrm{h^1} = \frac{\mathrm{c}\tau}{2} = \mathrm{c}\int \frac{\mathrm{dh}}{\mathrm{u}} = \int \mu \mathrm{dh} \tag{2.13}$$

where u is the group speed and μ, the refractive index of the medium, and the factor 2 caters for the fact that the pulse traverses the distance h^1 twice (Davies, 1989).
The signal echoes recorded by the receiver form a frequency dependent characteristic pattern of "traces" referred to as ionogram. It is a graph of vertical height against frequency, for example the Figure 2.2 shown

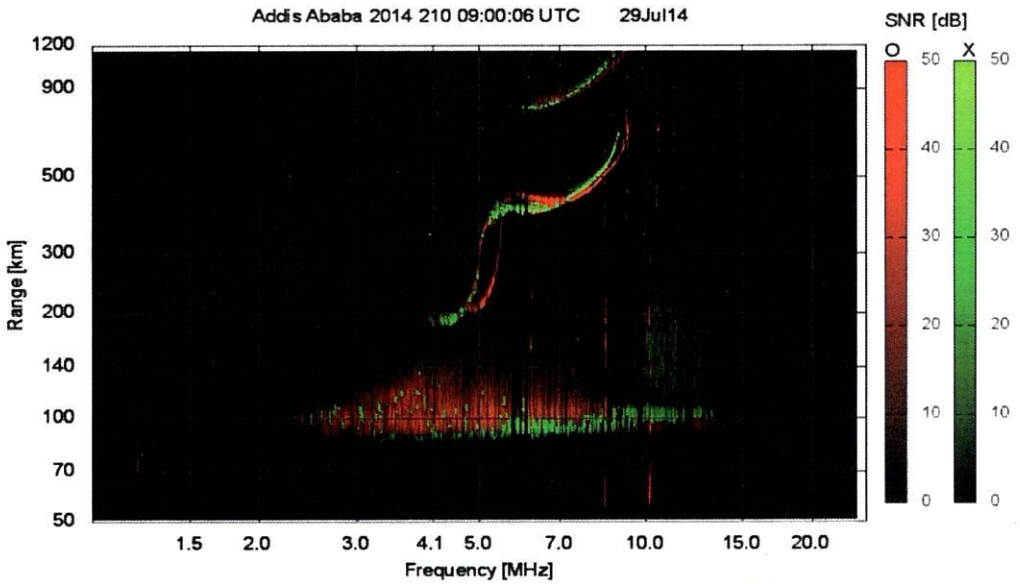


Figure 2.2: Sample ionogram from Addis Ababa, Ethiopia for 29^{th} July 2014 at 09:00:06

From Figure 2.2 of the ionogram, two traces are seen. The red trace representing the ordinary (O) wave and the green trace representing the extraordinary (X) wave. The two traces arise due to the effect known as magneto-ionic splitting where, the transmitted pulses propagate in two different ways by the influence of the Earth's magnetic field on propagation through the ionised plasma (Chen et al., 2013). The vertical asymptotes in the ionogram for these traces represent the critical frequencies foF2 for the O-wave and fxF2 for the X-wave (McNamara, 1991; Chen et al., 2013).

2.3.2 Global Navigation Satellite System

Global Navigation Satellite System (GNSS) is a network of satellites orbiting the Earth each broadcasting its location in space and time to ground control stations and receivers such that their ground positions are calculated by a technique of trilateration (Moldwin, 2008). It is any satellite constellation that provides positioning, navigation, and timing (PNT) services on a global or regional basis. So far the most prevalent GNSS constellation in the global system are two in full operation; the Global Positioning System (GPS) of United states with 33 satellites and GLObalnaya NAvigatsionnaya Sputnikovaya Sistema (GLONASS) of the Russian Federation with 29 satellites. In addition to the two, there are other global and regional systems under development, Globally for example there is: European satellite navigation system (Galileo) of Europe with 26 satellites and COMPASS or BeiDou Navigation Satellite System (BDS) of China with 27 satellites. Regionally, there is Indian Regional Navigation Satellite System (IRNSS) with 7 satellites and Quasi-Zenith Satellite System (QZSS) of Japan with 6 satellites. When all these come into full operation, there will be more precision for the users.

GNSS are now used in various fields such as: scientific research, precision agriculture, positioning, navigation and timing (PNT), mining, law enforcement, emergency response, land surveying, space stations, rail transport, aviation, finance, maritime etc. It is also useful in controlling computer networks, air traffic, power grids etc. In scientific research, the most commonly used so far is the GPS because it was the first GNSS of its kind.

2.4 Global Positioning System

GPS is a network of 24 satellites at a given time spread over six orbital planes that are inclined at an angle of about 55^o to Earth's horizontal at an altitude of about 20,200 km (Moldwin, 2008). The six planes are such that a receiver on the surface of Earth can view at least four satellites at a time. So far there are five generations of GPS satellites since the first one was launched in 1978.

The system of GPS contains three segments namely: the space segment (containing the satellites), the ground segment (control stations), and the user segment (civilians and military). Accurate position anytime, anywhere is provided by the interaction between these three segments. The GPS satellite and receiver have inbuilt clocks that measure the time a signal is sent and received respectively, so that the time of travel of a signal (satellite - receiver) is got from the difference between the two. The distance of a receiver is then obtained by multiplying the travel time with the vacuum speed of electromagnetic wave, c. This implies that any delay in the travel time will automatically cause an error in the position calculated, making the GPS primary purpose null (Pretab and Enge, 2006; Moldwin, 2008).

There are two main services from the GPS network: Standard Positioning Service (SPS) for civilian use, such as scientific research, surveying, precision agriculture, etc; and the Precise Positioning Service (PPS) for the military and other authorised users. All these are achieved from the current three signals that may be sent by a satellite: L1 having carrier frequency of 1575.42 MHz, L2 of frequency 1227.60 MHz and L5 having a frequency of 1176.45 MHz. The L5 signal is still limited to only precise positioning service while the SPS single frequency receivers are able to pick only the L1, and its dual frequency receivers can receive both L1 and L2. In addition to restricting L5 signal, the SPS users cannot still have access to the full capabilities of GPS through a mechanism known as Anti-Spoofing (AS). Anti-Spoofing is done by encrypting the two codes; Precision (P) code and Coarse/Acquisition (C/A) code, by the most precise P-code broadcasted on both L1 and L2 to Y-code which can only be used by authorised users (Pretab and Enge, 2006). Both L1 and L2 have the P-code but the C/A-code is restricted to only the L1 carrier frequency.

However, all the above may be affected by errors such as: satellite receiver clock error (due to the gradual drift of the clocks); atmospheric error (the space through which these signal pass are not homogeneous); multipath errors (due to multiple reflections of the signals by the surface objects like tall buildings before they reach a receiver); jamming (the signals interacting with other radio signals or electromagnetic radiations on their way to the Earth). Several techniques have been employed to try to eliminate these errors. First, GPS receivers are modified such that they can receive corrections from a second receiver at a known location. These modified receivers are known as differential GPS (DGPS). The second receivers are the base stations that cover relatively wide areas for augmentation. In America it is the Wide Area Augmentation System (WAAS), European Geo-stationary Navigation Overlay Service (EGNOS) for Europe, MTSAT Satellite-based Augmentation System (MSAS) for Japan, there is GPS Aided Geo-Augmentation Navigation (GAGAN) in India, System for Differential Corrections and Monitoring (SDCM) for Russian GLONASS. Nothing yet is established for Africa.

2.5 Total Electron Content

TEC is a parameter that describes the state of the Earth's ionosphere. TEC is the total number of electrons integrated from the satellite to the receiver, along a column of one square meter cross section, i.e., the electron columnar number density or the integral number of electrons along the column of one square meter path of a signal from the satellite to the receiver. It is often reported in multiples of Total Electron Content unit (TECu), where 1TECu=10^{16} electrons per square meter.

$$mathrmTEC = \int_{\text{satellite}}^{\text{receiver}} N_e \, dl \ \text{TECu}$$

Effects like advance of the phase and Doppler shift of a carrier, Faraday rotation of polarization and refraction of wave direction by wedge, group retardation and time delay of a modulation. All these depend on the total number of electrons along the ray path through the ionized atmosphere.

The TEC has a minima and maxima occurring approximately late in the night (before dawn) and mid-afternoon respectively on a quiet day (Garner et al., 2008). During the night, TEC gradually die off because of recombination of electrons and ions. TEC attains its maximum usually in the early afternoon and its minimum around midnight (Adewale et al., 2008; Habarulema, 2010; D'ujanga et al., 2013; Oron et al., 2013; Opio et al., 2015).

2.5.1 Measurement of Total Electron Content

Different techniques have been employed for decades to measure TEC experimentally. Much as few satellites have been built for this very purpose, radio signals from satellites that were launched for another purposes have made it possible for one to estimate TEC (Norsuzila et al., 2008; Kersley et al., 2004).

At first, the satellite that was launched for communication was used to estimate TEC by determining the polarization rotation of VHF signal coming from it. Later on signals from the various satellite navigation and positioning systems were exploited. For example: Naval Navigation Satellite System (NNSS) and now the GPS. Currently there is much information about TEC basing on the data that has been collected over a long period of time worldwide (Gao and Liu, 2002). In a related development, models yielding TEC have been employed regionally and globally including maps that are now routinely available on the Internet for TEC.

2.5.1.1 TEC From GNSS

Total Electron Content from GNSS can be measured from both single frequency receivers, such as the Differential GNSS, and the dual frequency receivers. However, TEC from dual frequency GNSS receivers are preferred over that from single frequency because dual frequency is capable of compensating for the ionospheric errors. The measurement composition of a dual frequency GNSS receiver are code-delay and carrier phase on L1 and L2 frequencies from the satellite. According to Gao and Liu (2002); Kersley et al. (2004), these can be expressed mathematically as:

$$\begin{aligned} P_1 &= R + c(dT_s - dT_r) + e_o + d_t + k_2 D + d_{P_a} - B_{P_a} + \varepsilon(P_a) \\ P_2 &= R + c(dT_s - dT_r) + e_o + d_t + k_1 D + d_{P_b} - B_{P_b} + \varepsilon(P_b) \\ \Phi_1 &= R + c(dT_s - dT_r) + \lambda_1 N_1 + e_o + d_t - k_2 D + b_{\Phi_a} - B_{\Phi_a} + \varepsilon(\Phi_a) \\ \Phi_2 &= R + c(dT_s - dT_r) + \lambda_2 N_2 + e_o + d_t - k_1 D + b_{\Phi_b} - B_{\Phi_b} + \varepsilon(\Phi_b), \end{aligned} \tag{2.14}$$

where:

P_j	:	Pseudorange measured on L_j (m) for j = 1, 2
Φ_j	:	Carrier phase measured on L_j (m)
R	:	Range between the satellite and the receiver (m)
c	:	speed of light (ms^{-1})
dT_s	:	Clock error of the satellite with respect to GPS time (s),
dT_r	:	Clock error of the receiver with respect to GPS time (s),
λ_j	:	GPS signal wavelength measured on L_j (m),
N_j	:	Carrier phase integer ambiguity,
d_t	:	Delay from the troposphere (m),
D	:	Delay parameter of the ionosphere (m),
d_o	:	Orbit error of satellite (m),
d	:	Hardware delays of satellite (m)
B	:	Hardware delays of receiver (m)
$\varepsilon(\Phi_j)$	:	Pseudorange Noise measurement and multipath (m)
$\varepsilon(P_j)$	:	Carrier phase measurement noises (m).

Setting the pseudorange and carrier phase observations as a linear combination at the two frequencies gives.

$$\begin{aligned} \Delta P &= P_b - P_a \\ \Delta\Phi &= \Phi_b - \Phi_a \end{aligned} \tag{2.15}$$

Substituting equations 2.15 into equation 2.14 gives

$$\begin{aligned} \Delta P &= dD + d_p - B_p + \varepsilon(P_b) - \varepsilon(P_a) \\ \Delta\Phi &= dD + \lambda N + d_\Phi - B_\Phi + \varepsilon(\Phi_b) - \varepsilon(\Phi_a) \end{aligned} \tag{2.16}$$

where

$dD = D(k_1 - k_2)$: is delay in the ionosphere

$d_p = d_{p_b} - d_{p_a}$: is the differential satellite delay for carrier phase

$d_\Phi = d_{\Phi_b} - d_{\Phi_a}$: is the differential satellite delay for pseudorange

$B_P = B_{P_b} - B_{P_a}$: is the differential receiver delay for carrier phase observation

$B_\Phi = B_{\Phi_b} - B_{\Phi_a}$: is the differential receiver delay for pseudorange observations

$\lambda N = \lambda_2 N_2 - \lambda_1 N_1$

The sTEC can then be estimated from the Equation 2.16 as

$$\begin{aligned} \Delta P &= 40.3\left(\tfrac{1}{f_2^2} - \tfrac{1}{f_1^2}\right) sTEC_p \\ \Delta\Phi &= 40.3\left(\tfrac{1}{f_2^2} - \tfrac{1}{f_1^2}\right) sTEC_\Phi \end{aligned} \tag{2.17}$$

This slant TEC obtained from the differential pseudorange and differential carrier phase is given by:

$$\begin{aligned} sTEC_P &= \tfrac{1}{40.3}\left(\tfrac{f_1^2 f_2^2}{f_2^2 - f_1^2}\right)\Delta P \\ sTEC_\Phi &= \tfrac{1}{40.3}\left(\tfrac{f_1^2 f_2^2}{f_2^2 - f_1^2}\right)\Delta\Phi \end{aligned} \tag{2.18}$$

The TEC values estimated using the procedures explained above are not exact. They are affected by different types of errors. The TEC from pseudorange contain high

level of noise compared to that of carrier phase measurement. To minimize the noise effect, we smoothen the pseudorange data using a carrier phase measurement technique known as carrier phase leveling:

$$B = \frac{1}{n}\sqrt{\sum_{i=1}^{n}[(\Delta P_1 i - \Delta P_2 i) - (\Delta\Phi_1 i - \Delta\Phi_2 i)]^2}$$

where n is the phase-connected arc number of measurements for a given receiver and satellite (Mannucci et al., 1998).

2.5.1.2 TEC From Ionosonde

Ionosondes are useful in mainly characterising the profile of the ionosphere from the bottom-side to reveal the peak electron density and height (M.Stankov et al., 2010). This is all possible after extracting the important ionosonde parameters such as the E layer critical frequency (foE), F2 layer critical frequency (foF2) that helps to calculate the F2 layer peak height (hmF2), and the propagation factor (M3000F2). Ionosondes on the ground can measure electron concentration N(h) only up to the peak of the F2 layer. They cannot provide direct information on the top-side ionosphere. To determine TEC from the ionosonde called Ionosonde Total Electron Content (ITEC)) from ionograms, the topside electron density N_T is modeled using all information contained in the measured bottom-side profile (McKinnell et al., 2007). i.e

$$\mathrm{ITEC} = \int_0^{\mathrm{h_m f2}} \mathrm{N_B(h)dh} + \int_{\mathrm{h_m f2}}^{\infty} \mathrm{N_T(h)dh} \tag{2.19}$$

2.6 Swarm Satellite Mission

Swarm Satellite is the 5^{th} mission of the European Space Agency (ESA), launched on 22^{nd} November 2013 (Verhoeven et al., 2011). During the launch, the three satellites named Swarm Alpha, Bravo and Charlie (abbreviated to Swarm A, B and C) were put together on the same rocket and sent to an altitude of about 500 km height (van den IJssel et al., 2015). They were later separated to different orbits where, Swarm A and Swarm C dropped to 450 km altitude while the third satellite (Swarm B) was raised to 530 km (Wood et al., 2022). The satellites are orbiting the Earth in a polar configuration, allowing them to survey almost the entire planet with a mission to measure the strength and direction of Earth's magnetic field with unprecedented precision. The angle between the orbital planes of the upper and lower satellites was very small and started increasing gradually and by 2015, it was at 90° to each other. This allows the entire Earth to be sampled more quickly and the sources of the magnetic fields to be identified more accurately (van den IJssel et al., 2015).

2.6.1 Swarm Satellite Instrumentation and Measurements

2.6.1.1 Instrumentation

The body of a Swarm satellite is nine meters long and is covered in solar panels, with a four-meter boom holding sensitive magnetic field measuring instruments, positioned to minimize electrical and magnetic interference (Pastena et al., 2020). Two instruments are dedicated to measure the magnetic field: one at the end of the boom, the scalar device that measures the strength of the magnetic field, while the other is a vector sensor, positioned in the middle of the boom, measures the field's direction. The vector sensor uses star cameras to ensure accurate satellite orientation (Pastena et al., 2020; van den IJssel et al., 2015). Other different payloads are positioned on the vehicle as shown in Figure 2.3.

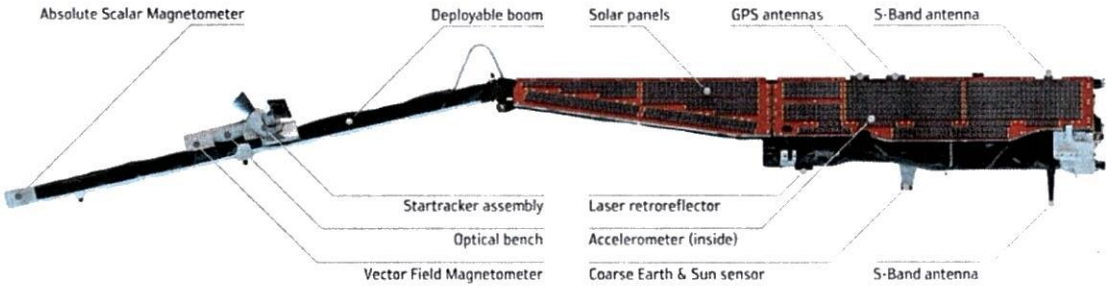


Figure 2.3: Side-view of instrumentation on the Swarm satellites. The satellite flies with the boom trailing at the rear (Copyright of ESA).

2.6.1.2 The Langmuir Probes of the SWARM Electric Field Instrument

The Electric Field Instrument of swarm satellite is equipped with two Langmuir probes (LPs), consisting of solid titanium spheres, 8 mm in diameter, mounted on rods that are 8 cm long (Buchert et al., 2015; Knudsen et al., 2017). These rods are mounted on the satellite and protrude in the direction of Earth at the front. The probes generally function in harmonic mode, where a bias voltage is applied and modulated in a sinusoidal pattern, or "rippled," at a frequency of 125 Hz over intervals of 79–112 ms (Buchert et al., 2015). The onboard measurement yields the average current, i, over this duration, along with the mean derivative $\frac{di}{dv}$, which reflects admittance. To determine the plasma density N_e, periods with a rippled negative bias are employed, leading to the current to the probe being primarily carried by ions. Both i and the real component of $\frac{di}{dv}$ are proportional to N_e on assumption of quasi-neutrality. The proportionality factor relies on the probe's known cross-section and the velocity of the ions. Assuming that the ions are exclusively O^+, thermal ion effects can be disregarded. The satellites travel along their orbit at a high speed, approximately 2.06 kilometers per second, which is considerably faster than typical plasma convection speeds, except possibly during periods of intense convection at high latitudes. As a result, the orbital

speeds of the satellites serve as a reasonable approximation for the ion velocities.

The ion current and admittance are recorded for 79 ms at a frequency of 2 Hz. During the intervals outside these periods, the mean bias is adjusted to measure the electron current using the previously mentioned ripple technique, which is used to estimate the temperature of the electron and the electric potential of the spacecraft. Between the two probes, one is consistently set to high gain, while the other is set to low gain. The high gain measurements are used to capture the (weaker) ion current.

2.6.1.3 The GNSS Receivers of Swarm

The Swarm satellites are equipped with upward-facing embedded dual-frequency GNSS receivers, allowing Precise Orbit Determination (POD) with location precision within a few centimeters.

2.6.2 Swarm Measurements

Swarm measure the magnetic field, electric field and ionospheric parameters. The magnetic field measured by the satellite originates from four main sources: the Earth's core (generating the main field), magnetic rocks in the Earth's crust, the ionosphere in the upper atmosphere, and the interaction between the Earth's magnetic field and the Sun's magnetic field (magnetosphere) (Friis-Christensen et al., 2006). One of the ionospheric parameters measured by swarm is the TEC using the same steps as described in subsection 2.5.1.1. All the data collected by these satellites are processed by the British Geological Survey (BGS) and is stored in the database of ESA. The archived data are of two types. i.e level-1b and level 2 products (Fan et al., 2022).

2.6.2.1 Level-1b products

Swarm's Level-1b data products consist of time-series data that have been quality-checked, calibrated, and corrected. It is presented in standard physical SI units within geo-referenced coordinate systems. These products are generated separately for each of the three satellites each day. Each product includes all available data for the given day, from 00:00 to 23:59 UT. An example illustrating the convention naming of the files of Swarm Level-1b 1 Hz magnetic product MAGx LR from 23^{th} February 2013 is given in Figure 2.4. In every epoch, the data has three different products, Ephemeris products, magnetic products, and plasma products as shown in Table 2.1.
The various Level-1b data products listed in Table 2.1 comprise: Ephemeris Products, which are generated from data collected by the GNSS receiver; Magnetic Products, which include measurements from the two magnetometers; and Plasma Products, which feature data from the Thermal Ion Imager and Langmuir probe (TIIL). Most Level-1b products are available in the Common Data Format (CDF), a file format designed for time series data storage. However, GNSS receiver data are provided in RINEX and

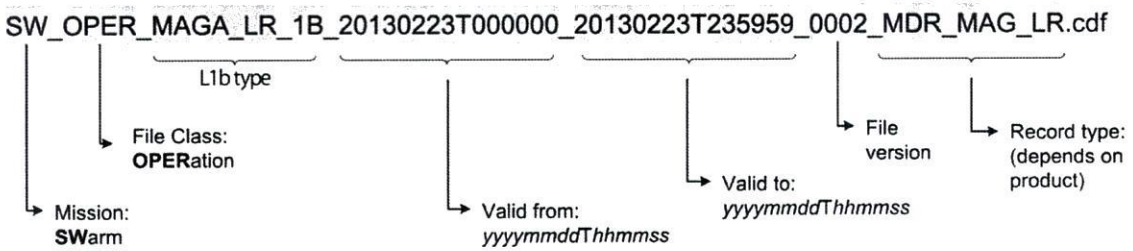


Figure 2.4: Example illustrating the filename of the Swarm-A Level-1b low-rate magnetic product MAGx LR from 23th February 2013 (Olsen et al., 2013).

Table 2.1: Swarm Level-1b products. The "i" in the product type is a placeholder for "A", "B", or "C" indicating the satellite. (Olsen et al., 2013)

Type	Descriptive Name	format	Contents
Ephemeris products			
GPSi_RO	RINEX Observations	RINEX 3,0	Processed and corrected data from the GPS receiver, 0.1 Hz sampling
GPSi_RN	RINEX Navigation data	RINEX 3.0	GPS navigation data from the GPS receiver
GPSiNAV	Navigation solution	SP3	Position and velocity from on-board GPS receiver navigational solution 1 Hz sampling
MADi_SC	Medium precision orbit determination	SP3	Position and velocity from automated, medium-precision orbit determination based on GPSx_RO data 1 Hz sampling
STRiATT	Attitude	CDF	Processed and corrected attitude information of the spacecraft rame from the star Tracker, 1 Hz sampling
ACCi_PR	Non gravitational acceleration	CDF	Pre-processed linear and angular non-gravitational acceleration measurements from the accelerometer, 1 Hz sampling.
Magnetic products			
MAGi_LR	Low rate (1Hz) Magnetic data	CDF	Calibrated and corrected magnetic vector and scaler measurements interpolated to UTC seconds and provided in VFM sensor as well as in NEC frame.
MAGi_HR	High rate (50 Hz) magnetic data	CDF	Calibrated and corrected magnetic vector measurements, provided in VFM sensor as well as in NEC frame
MAGi_CA	Magnetic calibration data	CDF	Magnetic scaler calibration data for long-term VFM analysis
Plasma products			
EFIi_PL	plasma data	CDF	Processed and corrected plasma measurements from the EFI instruments including electric field vector, plasma density, plasma electron and ion temperature, 2 Hz sampling.
LPi_CA	Langmuir probe calibration data	CDF	Offset determination mode data and corresponding estimated calibration parameters
TIIi_CA	Thermal ion imagery calibration data	CDF	Daily calibration parameters used for monitoring and optimisation of the TII instrument performance.

SP3 formats, as is standard for this type of information.

Arguably the most significant Level-1b product, MAGx LR (where "x" represents "A," "B," or "C" to indicate the respective satellite), provides 1 Hz time series data with magnetic field observations from each of the three satellites. A more detailed description of the product's contents can be found in Table 2.2. Along with time and position data, it includes the magnetic scalar intensity F and the three components of the magnetic vector.

Table 2.2: Content of Swarm Level-1b Product MAGx LR.

Element	Contents	Units
Timestamp	Time of observation	CDF_EPOCH
SyncStatus	Time reference information	—
Latitude	Latitude of observation in the *International Terrestrial Reference Frame* (ITRF)	degree
Longitude	Longitude of observation in the ITRF	degree
Radius	Radius of observation in ITRF	m
F	Magnetic field intensity	nT
dF_AOCS	Magnetic stray field correction intensity related to attitude control magneto-torquers	nT
dF_other	Magnetic stray field correction intensity of all other sources	nT
F_error	Error estimate on magnetic field intensity	nT
B_VFM	Magnetic field vector in the instrument frame of the VFM magnetometer	nT
B_NEC	Magnetic field vector in the NEC (North, East, Center) frame	nT
dB_AOCS	Magnetic stray field correction vector related to attitude control magneto-torquers (in VFM frame)	nT
dB_other	Magnetic stray field correction vector of all other sources (in VFM frame)	nT
B_error	Error estimates on magnetic field vector $\mathbf{B}_{\mathrm{VFM}}$ (in VFM frame)	nT
q_NEC_CRF	Rotation from NEC frame to STR Common Reference Frame (CRF), quaternion (NEC $\leftarrow$ CRF)	—
Att_error	Error estimate on attitude information	degree/10^3
Flags_F	Flags characterizing the magnetic field intensity measurement: spikes or gap in data, discrepancy between ASM and VFM, etc.	—
Flags_B	Flags characterizing the magnetic field vector measurement $\mathbf{B}_{\mathrm{VFM}}$ and $\mathbf{B}_{\mathrm{NEC}}$: spikes or gap in data, discrepancy between ASM and VFM, etc.	—
Flags_q	Flags characterizing the attitude information: identification of active heads, blinding, etc.	—
Flags_Platform	Flags characterizing the spacecraft platform information: thruster activation, lack of telemetry, etc.	—
ASM_Freq_Dev	ASM reference frequency calibration data deviation for ASM stability assessment	$\mathrm{Hz}^{1/2}$

2.6.2.2 Level 2 products

Swarm Level-2 data products are the processed and corrected outputs from each of the three Swarm satellites, presented in a standardized format. There are two types of Level-2 products, referred to as Cat-1 and Cat-2 products, depending on the complexity of the processing involved. Cat-1 data processing utilizes advanced algorithms to produce Level-2 products that characterize specific sources of the Earth's magnetic field, such as the lithosphere field or time series of the large-scale magnetospheric signal. Cat-1 products are generated by the Swarm Core Algorithm Research Facility (SCARF), as the processing requires specialized scientific expertise.

On the other hand, Cat-2 product processing is less complex. These products are generated daily by ESA in the Swarm Swarm Processing and Data Archiving Ground Segment (PDGS) using algorithms developed by SCARF. This automated processing allows for quick product releases with minimal delays. Cat-2 products are designed for near-real-time applications, with processing delays of under one hour, making them ideal for purposes such as space weather monitoring. Table 2.3 provides an overview of the Level-2 products. Lastly, all Level-2 products undergo validation through inter-product comparisons and comparisons with independent data, with further details

Table 2.3: Content of Swarm Level-1b Product MAGx LR.

Science Objective	Name	Format	Description
(needed for Level-1b processing)	MSW_EUL_2_	ASCII	Time series of Euler angles describing transformation from STR-CRF to VFM frame for all three *Swarm* satellites (3 × 3 Euler angles)
Core field	MCO_SHA_2_	ASCII	Spherical harmonic model of the core field and its temporal variation
Lithospheric field	MLI_SHA_2_	ASCII	Spherical harmonic model of the lithospheric field
Electrical conductivity of the mantle	MIN_1DM_2_	ASCII	1D model of mantle conductivity
	MIN_3DM_2_	ASCII	3D model of mantle conductivity
	MCR_1DM_2_	ASCII	1D C-responses
	MCR_3DM_2_	ASCII	3D C-response maps
External current systems	MMA_SHA_2_	CDF	Spherical harmonic model of the large-scale magnetospheric field and its Earth-induced counterpart
	MIO_SHA_2_	ASCII	Spherical harmonic model of the daily geomagnetic variation at middle latitudes (Sq) and low latitudes (EEJ)
Precise Orbit Determination (POD)	SP3xCOM_2_	SP3	Time series of position and velocity of the center of mass for satellite x (x = A, B or C)
	ACCxCAL_2_	CDF	Accelerometer calibration parameters for satellite x
	ACCxPOD_2_	CDF	Time series of non-gravitational accelerations estimated for satellite x
Magnetic Forcing of the Upper Atmosphere	ACCx_AE_2_	CDF	Time series of calibrated and pre-processed accelerometer observations and of aerodynamic accelerations for satellite x
	DNSxWND_2_	CDF	Time series of neutral thermospheric density and wind speed for satellite x
Earth environment and Space-Weather (Cat-2 products)	IBIxTMS_2F	CDF	Ionospheric bubble index for satellite x
	TECxTMS_2F	CDF	Time series of the ionospheric total electron content for satellite x
	FAC_TMS_2F	CDF	Time series of field-aligned currents determined from combination of *Swarm* A and *Swarm* B
	FACxTMS_2F	CDF	Time series of field-aligned currents (single-satellite solution) for satellite x
	EEFxTMS_2F	CDF	Equatorial Electric Field for satellite x

available in Beggan et al. (2013).

2.6.2.3 Level 2 -TEC

TEC measured by GNSS receivers on Swarm satellites follow the same processes as described in section 2.5.1.1, and the final processed TEC presented as level 2 TEC (L2-TEC). L2-TEC data provide the integrated electron density along the line of sight from the Swarm satellites to the GNSS satellites. The highest frequency for L2-TEC data is 1 Hz, which is lower than that of the Swarm Level-1b (L1b) electron density data. However, since a single Swarm satellite can communicate simultaneously with multiple GNSS satellites, there can be several STEC data points for a specific universal time (UT). Due to the broad spatial coverage at a given UT, the L2-TEC data can serve as valuable input for global ionospheric assimilation, which aims to define three-dimensional electron density structures.

One data file of L2-TEC (TECxTMS_2F), is produced each single day and per each of the three swarm satellites (where "x" represents "A," "B," or "C" to indicate the respective satellite). An L2-TEC file is generated only when all of the following input files are present:

Table 2.4: The list of variables in the L2-TEC data product.

Variable name	Description	Unit
Timestamp	Time stamps in Universal Time	cdf epoch
Latitude	Geographic latitude of the Swarm satellite	degree
Longitude	Geographic longitude of the Swarm satellite	degree
Radius	Distance of the Swarm satellite from the Earth's center	m
GPS-Position	X-, Y-, Z-coordinates of the GNSS satellite used for STEC calculation	m
LEO-Position	X-, Y-, Z-coordinates of the Swarm satellite used for STEC calculation	m
PRN	Pseudo-Random Number (PRN) identifier of the GNSS satellite used for STEC calculation	no unit
L1	GNSS L1 carrier phase observation	m
L2	GNSS L2 carrier phase observation	m
P1	GNSS P1 carrier phase observation	m
P2	GNSS P2 carrier phase observation	m
S1	GNSS signal-to-noise ratio or raw signal strength on L1	no unit
S2	GNSS signal-to-noise ratio or raw signal strength on L2	no unit
Absolute-STEC	Absolute slant TEC	TECU
Absolute-VTEC	Absolute vertical TEC	TECU
Elevation-Angle	Elevation angle	degree
Relative-STEC	Relative slant TEC	TECU
Relative-STEC-RMS	Root mean square error of relative slant TEC	TECU
DCB	GNSS receiver differential code bias	TECU
DCB-Error	Error in the GNSS receiver differential code bias	TECU

(i) GNSS RINEX observation files (GPSA_RO_1B, GPSB_RO_1B, or GPSC_RO_1E

(ii) Swarm ephemerids (MODA_SC_1B, MODB_SC_1B, or MODC_SC_1B).

(iii) GNSS satellite ephemerids (AUX_GPSEPH), and

(iv) Differential code bias of GNSS satellite transmitters (AUX_DCB_2F).

The frequency of the L2-TEC data for any of the three satellites varies: it began at 0.1 Hz at the start of the mission and was increased to 1 Hz in July 2014. Table 2.4 lists the variables included in the L2-TEC data product. The elevation angle of the GNSS satellites as observed from Swarm can be calculated using the position of the two satellites (swarm and GNSS).

2.7 Ionospheric Models

There are three different types of ionospheric models. These are Physics-based models, Empirical (or semi-empirical) models and data assimilation models.

2.7.1 Physics Based Models

These are models that involves the conservation of physical parameter such as continuity, momentum, energy etc, using an equations solved numerically as a function of spatial and time coordinates to calculate plasma densities, temperatures and flow velocities (Bellan, 2008; Ho et al., 2018). The model utilises the physics and chemistry for completeness where quality inputs of atmospheric, solar, and geomagnetic variables are fed for accuracy. Physics based models are tools that can comprehend the physical and chemical processes of the environment above the Earth's surface. Examples include: Thermosphere-Ionosphere-Electrodynamics General Circulation Model, Coupled Thermosphere Ionosphere Model, Utah State University-Time Dependent Ionospheric Model, and Semi-Analytical Model of the Ionosphere.

2.7.1.1 Thermosphere-Ionosphere-Electrodynamics General Circulation Mode

The Thermosphere-Ionosphere-Electrodynamics General Circulation Model (TIE-GCM) is a global 3-D numerical model developed at the National Center for Atmospheric Research High-Altitude Observatory (NCAR-HAO). It can simulate the coupling between the systems of the ionosphere and the thermosphere ranging from about 97 km to 600 km (MacQueen et al., 1980; Orrall et al., 2005). The model solves fully a series of thermodynamic, hydrodynamic, nonlinear and continuity equations consistently. Some of the continuity equations solved include: the ion continuity equation, neutral wind dynamo, continuity equations of the neutral gas, the ion and electron energy and momentum equations. The model can be accessed freely or on request from NASA's modeling center, Community Coordinated Modeling Center (CCMC).

2.7.1.2 Coupled Thermosphere Ionosphere Model

The Coupled Thermosphere Ionosphere Model (CTIM) consisted of two major components coupled together: Global thermosphere model developed by Fuller-Rowell and Rees (1980), and Mid- and high-latitude ionosphere convection model developed by Quegan et al. (1984). The plasmasphere and low latitude ionosphere has been added as the third component to extend further the CTIM model in order to give Coupled Thermosphere Ionosphere Plasmasphere electrodynamics model (CTIPe) (Gulyaeva and Bilitza, 2012). It can calculate the global thermosphere and the ionosphere of high-latitude using the physics processes. The inputs of CTIM include: the precipitation parameters of potential and the electron from the MHD model and subsequently provides the conductance and the ionospheric dynamo current to the potential solver.

Therefore, CTIM introduces first-principle calculations to replace the empirical conductance calculations (Bilitza and Tamara, 2012).

2.7.1.3 Utah State University-Time Dependent Ionospheric Model

The Utah State University-Time Dependent Ionospheric Model (USU-TDIM) developed by Schunk and Walker (1973) is an ion-based model that was meant for mid-latitude in the first place. The model solves the time-dependent continuity and momentum equations for ions (N_O^+, O_2^+, N_2^+, and O^+) as a function of altitude within a plasma flux tube that rotates with the system. It accounts for diurnal variations and incorporates all relevant processes in the E- and F-regions. It was later stretched by Schunk et al. (1976) to cover the high-latitude effects due to convection electric fields and particle precipitation. A reduced form of the ion energy equation was included, assuming that local heating and cooling processes are the primary factors, which is valid below 500 km. Sojka et al. (1981) described the incorporation of plasma convection and particle precipitation models, which was later expanded by Schunk and Sojka (1982) in the ionospheric model to account for ion thermal conduction and diffusive thermal heat flow. Additionally, Schunk et al. (1986) incorporated the electron energy equation, enabling a rigorous calculation of electron temperature at all altitudes. Overall, the theoretical development of the TDIM is thoroughly detailed by Schunk (1988).

Typically, the standard TDIM configuration requires inputs for the convection electric fields, neutral winds, neutral atmosphere and auroral precipitation. These inputs are provided by the Mass Spectrometer and Incoherent Scatter - 1986 (MSIS-86) model Hedin (1987), the Horizontal Wind Model (HWM) model Hedin (1991), the Hardy auroral oval (Hardy et al., 1987), and the Heppner-Maynard convection patterns (Heppner and Maynard, 1987), respectively. These predictors are empirical models that use the geomagnetic indices Kp and Ap on a three-hour basis, along with the solar indices f10.7 and f10.7A for the MSIS-86 and HWM models. In summary, the model incorporates the indices Kp, Ap, f10.7, and f10.7A.

2.7.1.4 Semi-Analytical Model of the Ionosphere 2

Semi-Analytical Model of the Ionosphere 2 (SAMI2) developed at the Naval Research Laboratory (NRL), is a physics based low-latitude ionospheric model. It It addresses the evolving dynamics of plasma and chemical interactions among seven ion species (H^+, He^+, N^+, O^+, N_2^+, NO+, and O_2^+) over an altitude range from about 100 km to the altitude of the outer space. SAMI2 resolves the continuity equations as well as the momentum equations for all seven ion species, while the temperature equation is addressed for H^+, He^+, O^+, and the electrons. It models plasma dynamics across the Earth's dipole field from one hemisphere to the other. SAMI2 accounts for the drift of $E \times B$ of a flux tube, both in longitude and altitude, and incorporates ion inertia in

the momentum equation for ions moving along the dipole field line. This consideration is particularly relevant for plasma dynamics at very high altitudes, where ion inertia becomes significant (Huba et al., 2000).

2.7.1.5 Semi-Analytical Model of the Ionosphere 3

Semi-Analytical Model of the Ionosphere 3 (SAMI3) is an improvement over SAMI2 by the same team at NRL, modeling the same ion species that extend from 70 km to approximately eight Earth radii and including magnetic latitudes up to ±88°. Similar to SAMI2, SAMI3 also resolves the same continuity and momentum equations for the three corresponding ion species. The unique thing about the model is that it has catered for the motion along the geomagnetic field by adding the ion inertia in the ion momentum equation. SAMI3 employs a fixed, irregular grid established in the magnetic coordinate system. One axis of this grid is oriented with the Earth's geomagnetic field, allowing the model to distinguish between motion parallel to and perpendicular to the magnetic field. SAMI3 can be set up to utilize either a oblique dipole model of the geomagnetic field of the Earth or a spherical harmonic depiction of Magnetic Apex coordinates, which incorporates the International Geomagnetic Reference Field (IGRF) model of the geomagnetic field (Emmert et al., 2010; Richmond, 1995).

SAMI3 calculates electric fields self-consistently by solving a 2-D equation of electrostatic potential, which is derived from current conservation in magnetic coordinates and takes into account currents driven by gravity. The orthogonal electric field is then used to compute the $E \times B$ drifts at mid- and low latitudes (Huba et al., 2008; Huba and Joyce, 2010). In its standard configuration, SAMI3 utilizes version 2.0 of the Naval Research Laboratory Mass Spectrometer Incoherent Scatter (NRLMSIS) climatology to define thermospheric composition and neutral temperature, and the HWM to specify East-West and North-South thermospheric winds (Drob et al., 2015; Emmert et al., 2021).

2.7.1.6 Field Line Inter-hemispheric Plasma model

The Field Line Interhemispheric Plasma (FLIP) model is a numerical tool designed to investigate the behavior of ionospheric plasma along magnetic field lines linking the northern and southern hemispheres. It emphasizes the movements and variations of plasma across the equator, considering factors such as solar activity, geomagnetic conditions, and ionospheric processes Kotov et al. (2018). The model is utilized to analyze how plasma flows and changes in various regions of the ionosphere, especially concerning phenomena such as equatorial spread F, ionospheric irregularities, and the overall interactions between the two hemispheres.

2.7.1.7 Global Ionosphere-Thermosphere Model

Global Ionosphere-Thermosphere Model (GITM) developed at the University of Michigan's Space Physics Research Laboratory (now known as the Climate and Space Sciences and Engineering Department), is a three-dimensional spherical code that models the coupled behavior of the Earth's thermosphere and ionosphere system (Ridley et al., 2006). It uses a stretched grid in latitude and altitude with a specified number of grid points in each direction for a flexible resolution. The model solves for both the neutral densities (O, O_2, N(2D), N(2P), N(4S), N_2, NO, H and He) and ion species (O+(4S), O+(2D), O+(2P), O_2^+, N^+, N_2^+, and NO^+).

GITM has four inputs; F10.7, Hemispheric Power Index (HPI), Solar wind velocity of Interplanetary Magnetic Field (IMF) and Solar irradiance. The output of the model include Temperatures of neutrals and ions, the East-West and North-South electron Neutral winds and vertical Plasma velocities, Neutral mass density, and Number densities.

2.7.2 Empirical and Semi-empirical Models of the Ionosphere

These are mathematical representations of the Earth's ionosphere based on observed data and measurements. They rely on analytical description of the ionosphere with functions obtained from experimental data to give a climatological description of the ionosphere.

2.7.2.1 International Reference Ionosphere

The International Reference Ionosphere (IRI) is an empirical model of the ionosphere that started in the late sixties as a project sponsored by the Committee on Space Research (COSPAR) and the International Union of Radio Science (URSI) (Bilitza et al., 2011). It rely on the worldwide network of ionosondes, the powerful incoherent scatter radars (Jicamarca, Arecibo, Millstone Hill, Malvern, St. Santin), the ISIS and Alouette topside sounders, and in situ instruments flown on many satellites and rockets to provide monthly averages of the electron density, electron temperature, and ion composition for a specified geographic location, time, and date (Rawer et al., 1978; Bilitza et al., 2011; Froń et al., 2020). The IRI model is regularly updated and maintained by an international group of scientists and the latest version is IRI-2020.

2.7.2.2 NeQuick

NeQuick is a 3-D, time-varying model of ionospheric electron density founded on an empirical climatological depiction of the ionosphere. It is an empirical model developed in the European region and predicts monthly mean electron density from analytical profiles, depending on solar-activity-related input values: Sun spot number

or solar flux, month, geographic latitude and longitude, height and Universal Time (UT) (Hochegger et al., 2000). NeQuick provides electron density profiles for different latitudes, longitudes, and times of the day.

2.7.2.3 Consultative Committee for International Radio Model

The Consultative Committee for International Radio (CCIR) model, now replaced by the ITU-R (International Telecommunication Union - Radiocommunication Sector) model, was widely used for ionospheric propagation predictions. It provided information about ionospheric characteristics such as electron density and absorption at different frequencies and times.

2.7.2.4 Bent Ionospheric Model

The Bent ionospheric model, developed in the 1960s by Roger Bent and colleagues at the U.S. Naval Research Laboratory, is an empirical model designed to predict electron density distributions in the Earth's ionosphere for applications such as radio wave propagation and satellite communication (Bilitza et al., 1988). Based on measurements from ionosondes, radars, and satellites, the model provides global coverage of electron density profiles across the key ionospheric layers. It incorporates variations based on latitude, longitude, time of day, season, and solar activity levels, using parametric equations to describe electron density as a function of these variables (Hoque et al., 2022).

2.7.2.5 The Thin Layer model

The thin layer model started with the work of Chapman that describes the profile of electrons in the ionosphere with respect to the height above the ground. The model assumes that the electrons within the ionosphere are distributed in such a way that there is a slight concentration around a thin layer at an altitude of h_m km from the Earth's surface. The point at which the line of sight intercepts this thin layer is the Ionospheric Pierce Point (IPP). Figure 2.5 is an illustration of the geometry used to map the slant TEC into vertical TEC, commonly referred to as vertical TEC (vTEC). From Figure 2.5, the zenith angle at the IPP can be obtained as

$$\sin\chi = \frac{R_e}{R_e + h_m}\cos\theta_{el}, \tag{2.20}$$

where; θ_{el} is the elevation angle of signal path at the receiver, χ is the zenith angle at the IPP, and R_e is the mean radius of the Earth. The slant TEC (sTEC) and the vTEC are related by

$$\text{sTEC} = \frac{1}{\cos\chi}\text{vTEC} \tag{2.21}$$

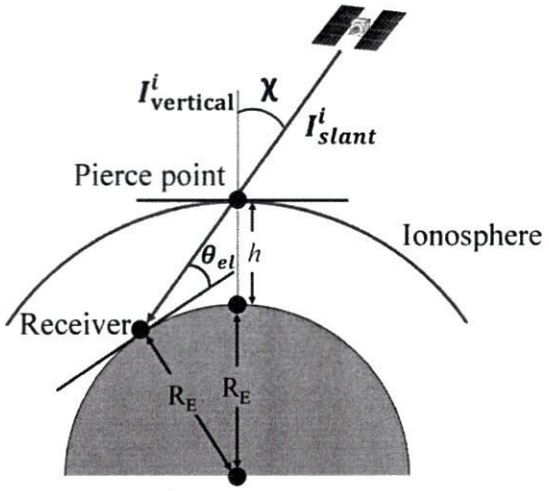


Figure 2.5: Geometry of the thin shell model adapted from Hein et al. (2016)

2.7.2.6 Klobuchar Model

The Klobuchar GPS ionospheric model, developed by by Klobuchar (1987a), is based on an empirical approach. The model was used in ionospheric studies and was is estimated to reduce the root mean square (RMS) of ionospheric range error globally by approximately 50% (Klobuchar, 1987a; Hobiger and Jakowski, 2017). The Klobuchar model treats the ionosphere as a single-layer, assuming that the ionosphere and its Total Electron Content (TEC) are concentrated in a thin layer at an average altitude of 350 km above the Earth's surface. To calculate the slant delay at the L1 frequency, the vertical delay at the Ionospheric Pierce Point (IPP) is multiplied by an obliquity factor, or mapping function, which varies with geomagnetic location and local time (Klobuchar, 1987a; Hoque and Jakowski, 2008; Hasan et al., 2020).

In the model, the daily fluctuation of ionospheric delay is represented using half of the cosine function, with its amplitude and period changing based on geomagnetic latitude and time. At night, the ionospheric delay is set to a constant value, while the amplitude and period of the semi-cosine function focused around 14:00 local time (Hobiger and Jakowski, 2017). When this model is applied to determine the amplitude and period of TEC at any location on Earth, eight coefficients—derived from two separate third-degree polynomials—are transmitted daily via GPS navigation messages. The ground control segment of GNSS computes and updates these coefficients based on seasonal changes and the level of solar activity (Setti Júnior et al., 2019; Ngayap et al., 2023).

2.7.2.7 Semi Empirical Low-latitude Ionospheric Model

A Semi Impirical Low-latitude Ionospheric Model (SLIM) combines theoretical formulations with empirical data to provide accurate and practical representations of ionospheric conditions (Anderson et al., 1987). Its based on three components: Theoretical basis that stems from the fundamental physics of ionospheric processes and influence of

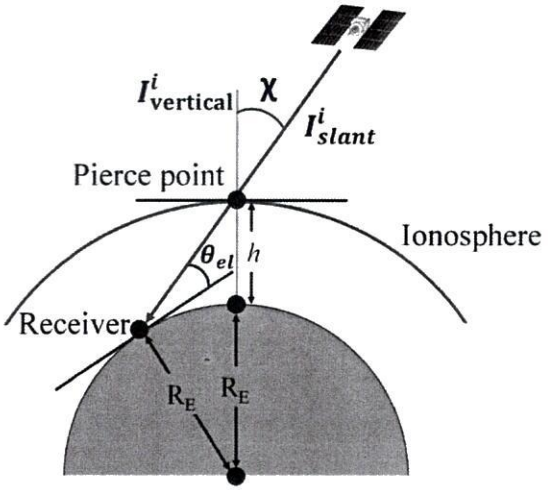


Figure 2.5: Geometry of the thin shell model adapted from Hein et al. (2016)

2.7.2.6 Klobuchar Model

The Klobuchar GPS ionospheric model, developed by by Klobuchar (1987a), is based on an empirical approach. The model was used in ionospheric studies and was is estimated to reduce the root mean square (RMS) of ionospheric range error globally by approximately 50% (Klobuchar, 1987a; Hobiger and Jakowski, 2017). The Klobuchar model treats the ionosphere as a single-layer, assuming that the ionosphere and its Total Electron Content (TEC) are concentrated in a thin layer at an average altitude of 350 km above the Earth's surface. To calculate the slant delay at the L1 frequency, the vertical delay at the Ionospheric Pierce Point (IPP) is multiplied by an obliquity factor, or mapping function, which varies with geomagnetic location and local time (Klobuchar, 1987a; Hoque and Jakowski, 2008; Hasan et al., 2020).

In the model, the daily fluctuation of ionospheric delay is represented using half of the cosine function, with its amplitude and period changing based on geomagnetic latitude and time. At night, the ionospheric delay is set to a constant value, while the amplitude and period of the semi-cosine function focused around 14:00 local time (Hobiger and Jakowski, 2017). When this model is applied to determine the amplitude and period of TEC at any location on Earth, eight coefficients—derived from two separate third-degree polynomials—are transmitted daily via GPS navigation messages. The ground control segment of GNSS computes and updates these coefficients based on seasonal changes and the level of solar activity (Setti Júnior et al., 2019; Ngayap et al., 2023).

2.7.2.7 Semi Empirical Low-latitude Ionospheric Model

A Semi Impirical Low-latitude Ionospheric Model (SLIM) combines theoretical formulations with empirical data to provide accurate and practical representations of ionospheric conditions (Anderson et al., 1987). Its based on three components: Theoretical basis that stems from the fundamental physics of ionospheric processes and influence of

the Earth's geomagnetic field on the ionosphere; Empirical Data from both ground and satellite measurements; Mathematical Representation such as electron density profile and empirical Coefficients (Banerjee and Mallick, 1997).

2.7.2.8 Fully Analytical Ionospheric Model

The Fully Analytical Ionospheric Model (FAIM) is designed to provide an analytical representation of the Earth's ionosphere (Anderson et al., 1989; Feltens et al., 2011). In contrast to empirical or numerical models that rely heavily on observational data and simulations, FAIM uses mathematical expressions to describe the ionospheric parameters quickly and even for real-time applications and integration into larger systems where computational efficiency is crucial (Bilitza, 1999). Such parameters include; electron density, ion composition, and temperature profiles.

2.7.2.9 Parameterised Real-time Ionospheric Specification Model

Parameterised Real-time Ionospheric Specification Model (PRISM) is a parameterised model which involves defining key parameters that describe ionospheric characteristics (Daniell and Brown, 1995). The parameters such as electron density, TEC, and layer heights are used (Filby and D, 1997). PRISM is designed to provide real-time ionospheric specifications since it integrates data from various sources, including ground-based ionosondes, GPS receivers, and satellite measurements, to create accurate ionospheric profiles (Pulliam and Charles, 2003).

2.7.3 Data Assimilation Models

Data assimilation models are a combination of observational data with numerical models of the ionosphere. These models are important for improving our understanding of the ionosphere's behavior and for enhancing the accuracy of ionospheric predictions. The common data assimilation models for the ionosphere are:

2.7.3.1 Kalman Filter and Ensemble Kalman Filter

These sequential data assimilation techniques are commonly used in ionospheric research. They sequentially update the ionospheric state based on available observations, such as TEC measurements from Global Navigation Satellite Systems (GNSS) receivers (Kosary et al., 2022). The Kalman filter and Ensemble Kalman Filter (EnKF) is a scheme that determines the best estimate of the global height-integrated O/N_2 ratio by combining GCM results and uncertainties with measurements and their errors (Codrescu et al., 2004). It then provides real-time updates of ionospheric conditions.

2.7.3.2 3DVAR and 4DVAR

Variational data assimilation methods, such as 3DVAR (three-dimensional variational) and 4DVAR (four-dimensional variational), are used to estimate the ionospheric state that best fits the available observations while considering the dynamics of the ionosphere (Rabier and Liu, 2003). A 4DVAR capability was provided by the introduction of a linear perturbation forecast model based on the Unified Model, the non-hydrostatic grid-point model producing our operational forecasts (Zhang et al., 2019). These methods are often employed in numerical weather prediction models with ionospheric extensions.

2.7.4 Data assimilated in ionospheric models

Data assimilated in ionospheric models typically include various measurements from both ground- and space-based instruments to improve the accuracy of ionospheric predictions. Key data sources include: GNSS receivers, ionosondes, radio occultation, coherent and Incoherent scatter radars etc.

2.7.4.1 GPS Radio Occultation

Radio occultation data from GNSS satellites, where signals pass through the Earth's atmosphere and ionosphere, can be used for ionospheric data assimilation. These observations provide valuable vertical profiles of electron density and temperature in the ionosphere.

The radio occultation technique was engineered in the 1960s to investigate the atmospheres of the outer planets in the solar system (Elliot, 1979). It utilizes the bending of the paths and the delay in the propagation of radio signals from GNSS satellites due to the molecules and electrons as they pass through the atmosphere (Mannucci et al., 2020). COSMIC satellite leverages this effect by capturing the radio signals and measuring their bending and delay, then down-links the data at ground stations found in different locations of the Earth. Different profiles of the signal, including bending angles, refractivity, temperature, pressure, water vapor in the atmosphere, and electron density in the ionosphere, can be retrieved once the data are transmitted back to the COSMIC Data Analysis and Archive Center (CDAAC) in Boulder (Yen et al., 2010). The profiles of Radio Occultation of COSMIC begin at the Earth's surface and reach up to the altitude of the COSMIC satellites, which is 800 km above the Earth (Anthes et al., 2000; Hwang et al., 2009).

2.7.4.2 Incoherent Scatter Radar

Incoherent Scatter Radar (ISR) measurements are valuable for studying the ionosphere's plasma properties. Data assimilation techniques can be used to incorporate

ISR data into ionospheric models, improving the characterization of electron density profiles (Ganguly and Brown, 2001). Radars offer vertical profiles of ionospheric electron density, akin to ionosondes, but they capture data both above and below the F2 peak. These devices are capable of scanning the ionosphere at oblique angles, rather than just vertically. Furthermore, various ionospheric parameters, including electron and ion temperatures, can be deduced from the echoes recieved by radar.

The principles of Incoherent Scatter Radar are based on the reflection of small quantities of energy caused by fluctuations in ionospheric electron density (Beynon et al., 1978). By analyzing the energy that is reflected back, one can derive electron and ion densities, as well as temperature and mass. Since the energy reflected back is minimal, highly precise receivers are required, resulting in very accurate parameter estimates. Incoherent Scatter Radars function at higher frequencies compared to ionosondes, usually ranging from 50 MHz to 1000 MHz. Because these transmitted frequencies exceed the frequency range of ionospheric plasma (0.1 to 9 MHz), it allows for the retrieval of electron density height profiles throughout the entire ionosphere (Bruno, 2021). The radars are equipped with beamforming (directional) antennas, allowing them to collect the distributions of electron density from various directions around the antenna. This capability facilitates the generation of a 2-D electron density maps of the radar's observational field.

2.7.4.3 Machine Learning-Assisted Assimilation:

In recent years, machine learning techniques, such as neural networks, have been explored to assist in ionospheric data assimilation. These approaches aim to learn complex relationships between observations and ionospheric parameters, potentially enhancing assimilation accuracy (Mallika et al., 2020).

2.7.5 Artificial Intelligence Models of the Ionosphere

Artificial intelligence (AI) models for the ionosphere apply machine learning and neural network techniques to enhance ionospheric predictions and analysis (Mallika et al., 2020). These models leverage large datasets from satellite observations, ground-based measurements, and simulations to predict ionospheric parameters, such as Total Electron Content (TEC), electron density, ionospheric disturbances and effective height of the ionosphere. For example: Neural Network models, Support Vector Machines (SVM), and Deep Learning Models (Zhou et al., 2023).

2.7.5.1 Artificial Neural Networks

Artificial Neural Networks (ANNs) is a computer algorithm developed to produce digital mechanisms that can work like the human brain. It is built to adapt to new situations in the same way the brain does (Basheer and Hajmeer, 2000). ANNs

utilize artificial "neurons" as their information processing units, similar to how neurons function in the human brain. An ANNs is a software system that can adjust to the information it receives by identifying trends and patterns. It retains pertinent data and generalizes behavior through its parallel distributed architecture (Habarulema et al., 2011; Haykin, 1998). ANNs has two generalised forms namely; feedforward and recurrent networks.

Typically, neural networks (NNs) are collections of interconnected "neurons" that aim to explore the behavioral trends of non-linear variables. They achieve this by retaining information in the connections among neurons and then extrapolating the changes in the parameters under investigation (Thakur and Konde, 2021). An ANN architecture comprises input, hidden, and output layers that can be tailored to include varying numbers of neurons during the implementation of the network. The quantity of neurons in the hidden layers is determined by the volume of data being processed. To facilitate computation and minimize training time required for optimization, the number of hidden layers can also be adjusted (Thakur and Konde, 2021; Haykin, 1998).

Feedforward networks represent a type of ANN whose structure does not allow for closed loops within the network connections. In contrast, recurrent networks are a type of ANN that feature closed-loop connections, making them effective for learning patterns that change over time (Sussillo et al., 2012; Habarulema et al., 2011). Thus, standard feedforward NNs differ from recurrent NNs in that the latter can allow the outputs of hidden neurons to be fed back into themselves through contextual connections.

Chapter 3: Materials and Methods

3.1 Introduction

The aim of this study was to establish a reference value of the effective height of the ionosphere over the East African region. This was achieved by utilizing data from various sources. The data sources are discussed in the following section.

3.2 Data sources

This study used data from three sources: GNSS receivers, Global Ionospheric Maps (GIMs), and ionosondes. The GNSS receiver network in the region that were utilized to provide the GNSS data are facilities from three different entities, namely:

(a) The University Navistar Consortium (UNAVCO), which has currently changed to the EarthScope Consortium. The stations under this consortium are represented by blue code names shown in Figure 3.1. The receiver of each station records data in a raw form at the host computer, and at the same time converts a copy into Receiver Independent Exchange (RINEX) format relayed through a network to the central database. The RINEX files of these stations were downloaded from the UNAVCO website[1].

(b) The International GNSS Service (IGS), which deployed the instruments at the stations whose four letter code names are represented by red colour in Figure 3.1. Their RINEX files were downloaded from the National Aeronautics and Space Administration (NASA) website[2].

(c) The European Space Agency (ESA), which deployed GNSS receivers on board the Swarm satellite. The swarm data files in Common Data Format (CDF) (see section 2.6.2.1) were downloaded from ESA's Swarm database[3]. The swarm level 2 daily data product was used, since it has an improved quality of the final data products compared to level 1b (Olsen et al., 2013; Beggan et al., 2013; Consortium et al., 2013). The CDF files extracted from the Swarm Level 2 TEC product for each day contained 20 variables. In this study, seven variables (Timestamp, Latitude, Longitude, PRN, Elevation angle, Relative sTEC and Absolute sTEC) of TEC product were used to determine the effective height of the ionosphere. More details about the swarm data formats and variables in each file is presented in section 2.6.

The GIMs are created from the data received from the network of over 2,000 IGS ground-based GNSS receivers distributed all over the world (Hernandez-Pajares et al., 2009; Zhu et al., 2023). Data received from the various IGS stations are analyzed at

[1] `https://data.unavco.org/archive/gnss/rinex/obs/`
[2] `ftp://cddis.gsfc.nasa.gov/pub/gps/data/daily/`
[3] `https://swarm-diss.eo.esa.int`

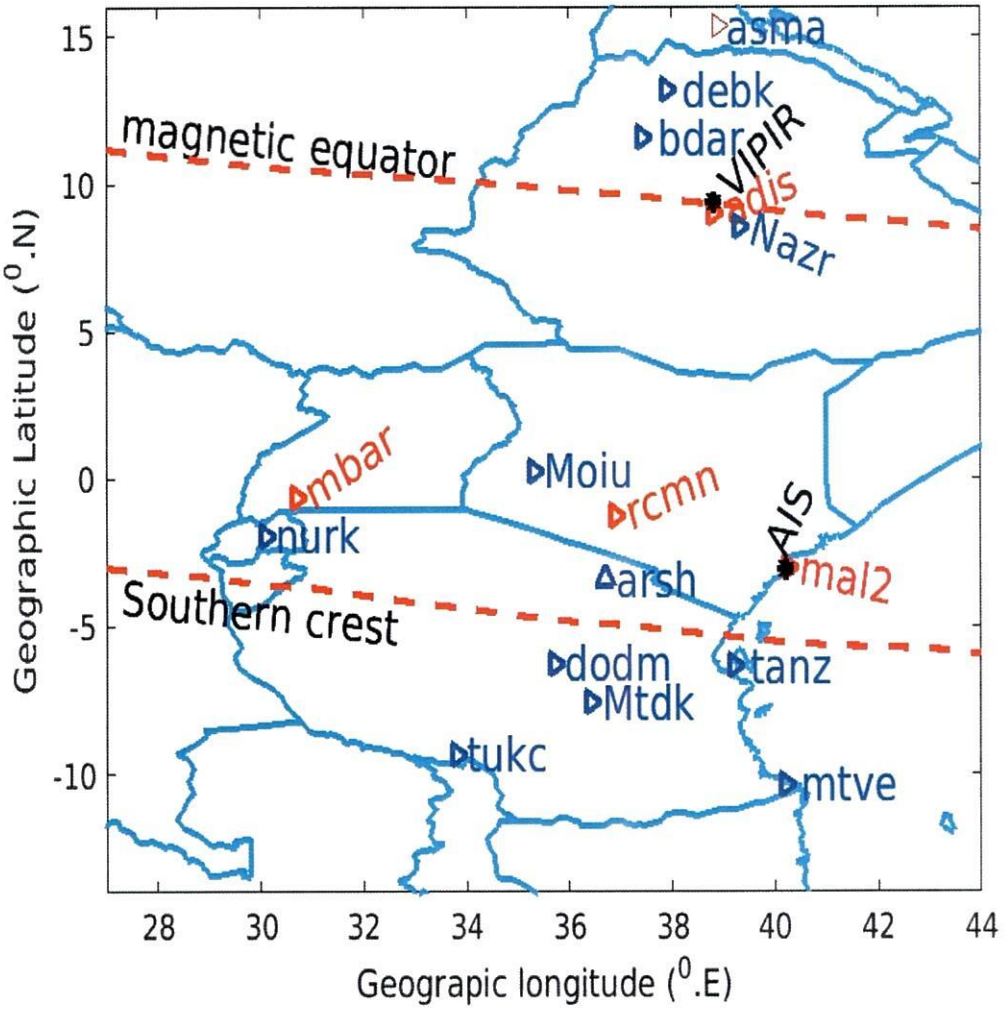


Figure 3.1: Locations of the ground based receivers on the region used in this study. The stations indicated in red are IGS, blue are UNAVCO, and black are ionosondes. The thick red dashes indicate the geomagnetic equator and the southern crest.

twelve different centers, which use various reference frames and techniques to estimate vTEC and the differential code biases (DCB). The results of the vTEC obtained at a given station is what is mapped over the globe as GIMs (Zhu et al., 2023). The computed GIMs are then validated by three validation centers (Jet Propulsion Laboratory (JPL), ESA, and Polytechnic University of Catalonia (UPC)) that combine them into a common IGS GIM (Chen et al., 2020). The temporal resolution and spatial resolution of standard IGS GIMs has been 2 hours and 5.0°× 2.5° in geographic longitude and geographic latitude respectively from 1994. However, some GIM providers such as CODE, have enhanced their products to a higher resolution. The temporal resolution of GIMs from Centre for Orbit Determination in Europe (CODE) was changed to 1 hour, whereas the spatial resolution was improved to 1.0°× 1.0° in geographic longitude and latitude (Liu et al., 2021). The GIMs data provided in IONosphere EXchange

(IONEX) format, was downloaded from earthdata archive of NASA[4]. The vTEC from GIMs at a specific GNSS station was derived by interpolating the IONEX data from the grid cell that includes the coordinates of the ground station.

Data from two ionosondes were used in this study: the Advanced Ionospheric Sounder (AIS) instrument developed and deployed in Malindi-Kenya by the Istituto Nazionale di Geofisica e Vulcanologia (INGV)-group, and the Vertical Incidence Pulsed Ionospheric Radar (VIPIR) deployed around the geomagnetic equator in Addis Ababa, Ethiopia. The VIPIR ionosonde is a donation from the United States Department of Defence (US DoD) in collaboration with the Boston College Institute of scientific research. The detailed location of the two ionosondes are showed in Table 3.1, and Figure 3.1.

The AIS ionosonde started routine operation on July 13, 2023, and the data is archived both on the host computer and the database of Electronic Space Weather upper atmosphere (ESWua). At the database, the raw data recorded by the instrument is remotely processed by a dedicated software (Autoscala) developed at INGV and managed in near-real time by the ESWua system at the INGV headquarters (Zuccheretti et al., 2003; Romano et al., 2008; Scotto and Sabbagh, 2021; Madonia et al., 2022). The users can access the raw ionograms or the processed ionograms (known as level-I data) from either the host computer or from the ESWua website[5]. In this study, the processed ionograms of AIS ionosonde were downloaded from the ESWua website.

The VIPIR ionosonde started routine operation on June 5, 2014, and the ionograms recorded for the short time it was operational are stored on the host computer. The raw ionogram of VIPIR ionosonde were extracted from the host computer, and processed using a special software SAO Explorer (version 3.6.1), commonly abbreviated as SAO-X. The SAO-X software uses edge detection algorithms to identify the traces on the ionogram (Reinisch and Galkin, 2011). These traces represent the different ionospheric layers and their corresponding reflection heights at various frequencies. The software then classifies the identified traces into different ionospheric layers based on predefined criteria and patterns observed in the ionogram (Mochalov and Mochalova, 2019). The location of all the ground-based data sources used in this study are summarized in Table 3.1.

It is important to note that, in this thesis, the methods that used GNSS data to determine the effective height of the ionosphere are referred to as GNSS-TEC techniques. These are discussed in the subsequent section.

[4] `https://cddis.nasa.gov/archive/gnss/products/ionex/`
[5] http://www.eswua.ingv.it/

Table 3.1: Location of Ground GNSS receivers used in this study

Station ID	Network	Data freq(mins)	Geographic Lat(°)	Geographic Lon(°)
MAL2	IGS Malindi	30	-3.02	40.24
RCMN	IGS Kenya	30	-1.22	32.87
MBAR	IGS Mbarara	15	-0.62	30.68
ADIS	IGS Adisababa	30	9.03	38.78
BDAR	IGS Ethiopia	30	11.59	37.42
NAZR	UNAVCO	30	8.57	39.29
ARSH	UNAVCO	15	-3.39	36.7
MTDK	UNAVCO	15	-7.54	36.4
MAKS	Scinda Makerere	30	0.32	32.63
MBRS	Scinda Mbarara	30	-0.61	30.72
DODM	IGS Dodoma	15	-6.22	35.81
MOIU	UNAVCO Kenya	30	0.31	35.33
NURK	UNAVCO Rwanda	30	-1.94	30.1
AIS-Ionosonde	Malindi Kenya	15	-3.02	40.2
Ionosonde 1	Maseno Kenya	15	0.04	34.62
Ionosonde 2	Adisabab Ethiopia	15	9.03	38.76

3.3 Methods

In this section, the methods used to estimate the effective height of the ionosphere over a given area was discussed. The various techniques are summarized in the following subsections.

3.3.1 Effective Height from Ionosondes

The scaled ionograms of the two ionosondes (AIS ionosonde and VIPIR ionosonde) provided a number of ionospheric parameters. The parameters considered in this study are the reflection heights of the signals and their corresponding frequencies. The maximum height beyond which signals are no longer reflected was identified and designated as the effective height of the ionosphere for that location. This height is denoted as hmF2, with the associated frequency known as the critical frequency (foF2). The values of hmF2 were used to investigate both the temporal and spatial variation of effective height.

3.3.2 Estimation of Effective height using GNSS-TEC

The techniques that determine effective height from GNSS-TEC rely on the conversion of sTEC to the equivalent vTEC by the help of an oblique factor known as the mapping function (MF) (Birch et al., 2002; Zhong et al., 2016). The conversion starts with an assumption that vTEC is directly proportional to sTEC, i.e

$$\mathrm{vTEC} = \mathrm{K} \cdot \mathrm{sTEC} \tag{3.1}$$

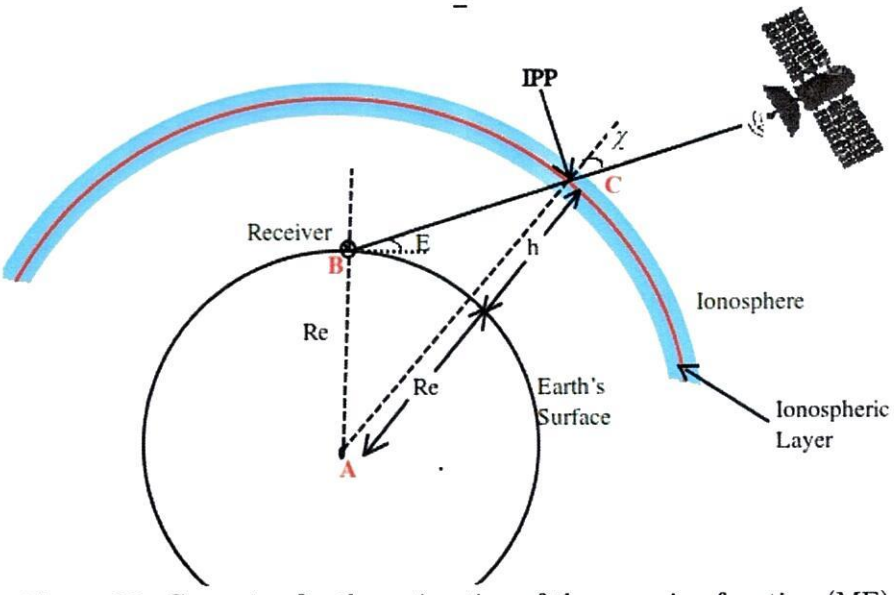


Figure 3.2: Geometry for the estimation of the mapping function (MF)

The constant of proportionality, K in Equation 3.1 is related to the mapping function (MF) under the thin shell approximation (Huang and Yuan, 2013) as.

$$\mathrm{MF} = \frac{1}{\mathrm{K}} \tag{3.2}$$

Figure 3.2 shows the transformation geometry of sTEC to vTEC, and can be used to get an expression for the constant K, and hence the MF. From the figure, applying the sine rule to triangle ABC, it can be shown that

$$\frac{\sin\chi}{\mathrm{R_e}} = \frac{\sin(90+\mathrm{E})}{\mathrm{R_e}+\mathrm{h}}, \tag{3.3}$$

where χ is the zenith angle of the respective satellite at the IPP, E is the elevation angle of the satellite and the ground receiver, and R_e is the radius of the Earth. Re-arranging Equation 3.3, gives the MF which is expressed as,

$$\mathrm{MF} = \sec\chi = \frac{1}{\sqrt{1-\left(\frac{\mathrm{R_e}\cdot\cos(\mathrm{E})}{\mathrm{R_e}+\mathrm{h}}\right)^2}} \tag{3.4}$$

Equation 3.4 shows that the mapping function depends entirely on the elevation angle (E) and the height of the ionosphere h, taken as the IPP height. Therefore, the GNSS-TEC technique can use the mapping function to estimate the effective height of the ionosphere.

In this study, the effective height of the ionosphere is denoted as h_m. A number of GNSS-TEC techniques employ the mapping function to determine the effective height of the ionosphere. These techniques were first applied to the data of the East African

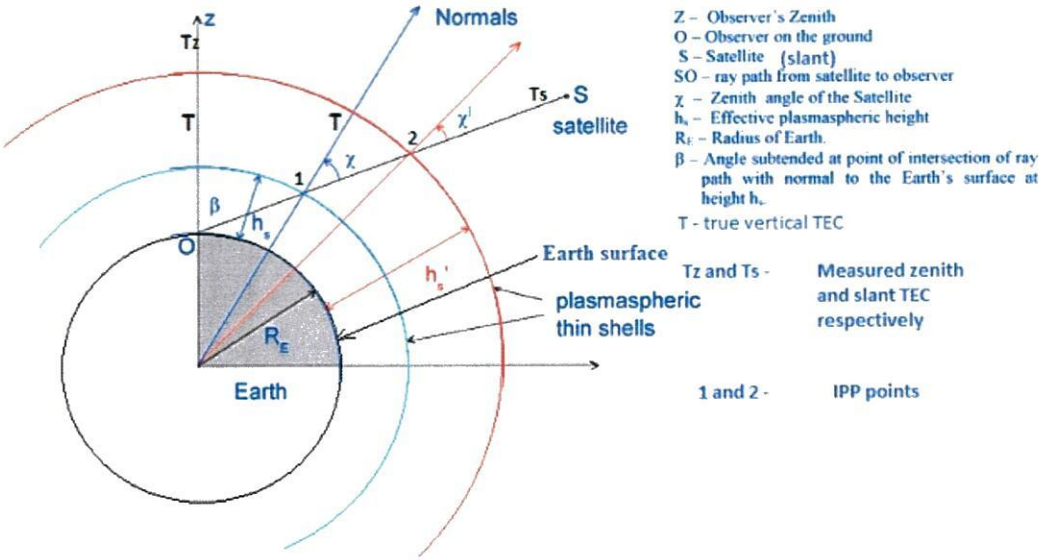


Figure 3.3: Schematic diagram showing the variation of oblique factor (χ) for the two different heights (h_s and h_s^I) (Birch et al., 2002).

low latitude region to test their suitability or effectiveness over the region. The different GNSS-TEC techniques tested include: the inversion technique (Birch et al., 2002), coinciding pierce point technique (Nava et al., 2007), Zenith - Oblique single epoch sTEC technique (Jiang et al., 2018), combined IGS GIMs technique (Li et al., 2017), and Swarm-IRI technique. These techniques are presented in the following subsections.

3.3.2.1 The Inversion Technique

The inversion technique (Birch et al., 2002), is used to estimate the effective height of the ionosphere by expressing the value of sTEC received from two satellites at the same time as a linear combination. The two satellites must be at different elevation angles. One must be at an elevation angle greater than 85^0 (taken as zenith satellite) and the other at an elevation angle between 30^0 and 60^0 (considered as the slant satellite). The value of sTEC of the slant satellite is represented by T_s and that of the zenith satellite represented by T_z (Figure 3.3). To convert sTEC into vTEC, a mapping function that depends on the obliquity factor represented as χ in Figure 3.3 is used for a particular height. The value of χ varies with height as shown in Figure 3.3.

It's clearly seen from Figure 3.3 that the obliquity factors χ and χ^I, for the two separate pierce points of the same ray path of satellite S, are completely different. This shows that for the same sTEC recorded, there will be two different values of vTEC in the two different IPP points. The relationship between χ or χ^I and the shell height (h_s or ${h_s}^I$) (Figure 3.3) is given in Equation 3.3, where the height of the shell represented in the

figure h_s or ${h_s}^I$ can be estimated using the Equations,

$$\begin{aligned} \sin\chi &= \frac{R_E \sin\beta}{R_E + h_s} \\ &or \\ \sin\chi^I &= \frac{R_E \sin\beta}{R_E + {h_s}^I}, \end{aligned} \tag{3.5}$$

where β is the satellite zenith angle at the receiver. Therefore when the most appropriate value of the factor represented by χ is known, the effective height of the ionosphere h_m can be determined.

According to Birch et al. (2002), the obliquity factor can be determined by first expressing each measured sTEC value from the two satellites (T_z and T_s) in terms of vTEC labelled "T" in Figure 3.3 as

$$\begin{aligned} T_z &= T \\ T_s &= T \sec\chi. \end{aligned} \tag{3.6}$$

Birch et al. (2002) assumed that the total biases of the two observed satellites are equal. However, the total biases (DCB) of the two GNSS satellites may not be the same because they are completely two different devices whose hardware failures are unique. Therefore, this study considered the total bias for each satellite independently. Hence, the expressions for T_s and T_z in Equation 3.6 were modified to

$$\begin{aligned} T_z &= T + B_z \\ T_s &= T \sec\chi + B_s \end{aligned} \tag{3.7}$$

where:

B_z : total bias of the receiver and the zenith satellite
B_s : total bias of the receiver and slant satellite

When the two expressions in Equation 3.7 are combined, a linear equation relating the two measured sTEC values (T_s and T_z) is expressed as

$$\mathrm{T_s} = (\mathrm{T_z} - \mathrm{B_z})\ \sec\chi + \mathrm{B_s} \tag{3.8}$$

For this study, the total bias of the GNSS satellite and the receiver were determined, particularly for the zenith satellites (B_z). The total bias of the zenith satellite, B_z, was obtained from the sum of the bias of GNSS satellite at the zenith derived from CODE and the bias of the GNSS receiver estimated when processing sTEC, as described in Seemala and Valladares (2011). From Equation 3.8, the value of $\sec\chi$ is given by the gradient of the graph of T_s vs $(T_z - B_z)$, i.e, the gradient M gives the obliquity factor

$$\mathrm{M} = \sec\chi \quad \text{or} \quad \sin\chi = \frac{\sqrt{\mathrm{M}^2 - 1}}{\mathrm{M}} \tag{3.9}$$

When Equation 3.9 is equated to Equation 3.5, the value of the effective height, h_m, is expressed as

$$h_m = R_E \left[\left(\frac{M}{\sqrt{M^2 - 1}} \right) \sin \beta - 1 \right] \tag{3.10}$$

Using all the GNSS receivers in the mentioned grid region, the total number of pairs of satellites observed simultaneously along the slant and zenithal paths were determined for each station using data for a particular period or month or season. The effective height was then determined for all the epochs when the two satellites were observed.

3.3.2.2 Coinciding Pierce Point Technique

The coinciding pierce point technique (Nava et al., 2007) was first tested in the American sector. According to Nava et al. (2007), the error created by the mapping function when converting sTEC into vTEC is a useful tool for estimating the effective height of the ionosphere or Ionospheric Pierce Point (IPP) altitude. The method uses links of two GNSS satellite signals for a given epoch to two ground stations not very far apart (less tha 1000 km). Two signals reaching the two ground stations are considered to coincide at the altitude of IPP if their coordinates (ϕ_1, λ_1) and (ϕ_2, λ_2) calculated at the IPP altitude fulfill the condition,

$$\begin{aligned} |\phi_1 - \phi_2| &\leq 0.2^o \\ |\lambda_1/\cos\phi_1 - \lambda_2/\cos\phi_2| &\leq 0.2^o \end{aligned} \tag{3.11}$$

Equation 3.11 indicates that the condition to be fulfilled is that the utmost difference

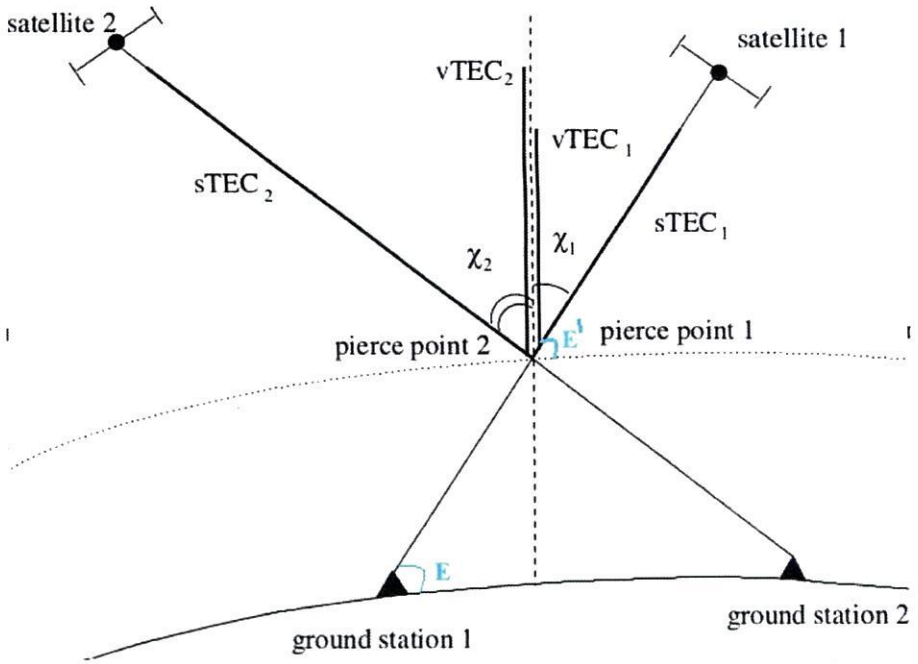


Figure 3.4: Geometry for the estimation of mapping function error extracted from Nava et al. (2007)

between latitudes and the component of the longitudes at the IPP altitude should not

be more than 0.2^{o}.

In this study, the implementation of the method started with identifying a satellite pair at a particular epoch and then calculate the latitude and longitude of the signals at a given height taken as IPP. The latitude and longitude of the IPP points, (ϕ_h, λ_h), were calculated using the Equations (Sunehra, 2013; Sedeek et al., 2017; Rabah and Sedeek, 2018).

$$\begin{aligned} \phi_h &= \sin^{-1}\left[\sin\phi_s \cos\psi_{(h)} + \cos\phi_s \sin\psi_{(h)} \cdot \cos A\right] \\ \lambda_h &= \lambda_s + \sin^{-1}\left(\frac{\sin\psi_{(h)} \cdot \sin A}{\cos\phi_h}\right), \end{aligned} \tag{3.12}$$

where ϕ_s is latitude of ground receiver, λ_s is longitude of ground receiver, A is the azimuth angle of the satellite at the ground receiver (obtained from the broadcast ephemeris of the GNSS satellite), ψ represent the offset between the elevation angles of the GNSS satellite at the ground station and at the IPP. ψ is obtained using the equation

$$\psi_{(h)} = E' - E, \tag{3.13}$$

where E is the elevation angle of the satellite at the ground station, E' is the elevation angle of the satellite at the IPP height (dos Santos Prol and de Oliveira Camargo, 2015). From the geometry of Figures 3.3 and 3.4, the angles E' and χ are complementary angles such that from Equation 3.5, χ can be written in terms of E' as

$$\sin\chi = \frac{\mathrm{R_e}\cos\mathrm{E}}{\mathrm{R_e} + \mathrm{h}} = \cos\mathrm{E}'.$$

E' is given by the equation

$$\mathrm{E}^{\mathrm{I}} = \cos^{-1}\left[\left(\frac{\mathrm{R_e}}{\mathrm{R_e} + \mathrm{h}}\right)\cos\mathrm{E}\right]. \tag{3.14}$$

The IPP coordinates (ϕ_1, λ_1) and (ϕ_2, λ_2) obtained were tested for coincidence using the condition given in Equation 3.11. If the condition is satisfied, the sTEC values of the satellites are then extracted. The sTEC extracted for each satellite was converted to vTEC using the MF (Equation 3.4).

At this point, the vTEC values at pierce point 1 ($\mathrm{vTEC_1}$) and pierce point 2 ($\mathrm{vTEC_2}$) (Figure 3.4) are equal since the signals from the two satellites are assumed to pass the ionosphere under the same condition. If there is any difference between the two vTEC values, it would be attributed to the value of h used in calculating the IPP coordinates. The difference between the two vTEC values is expressed as

$$\Delta\mathrm{vTEC} = |\mathrm{vTEC_1} - \mathrm{vTEC_2}|. \tag{3.15}$$

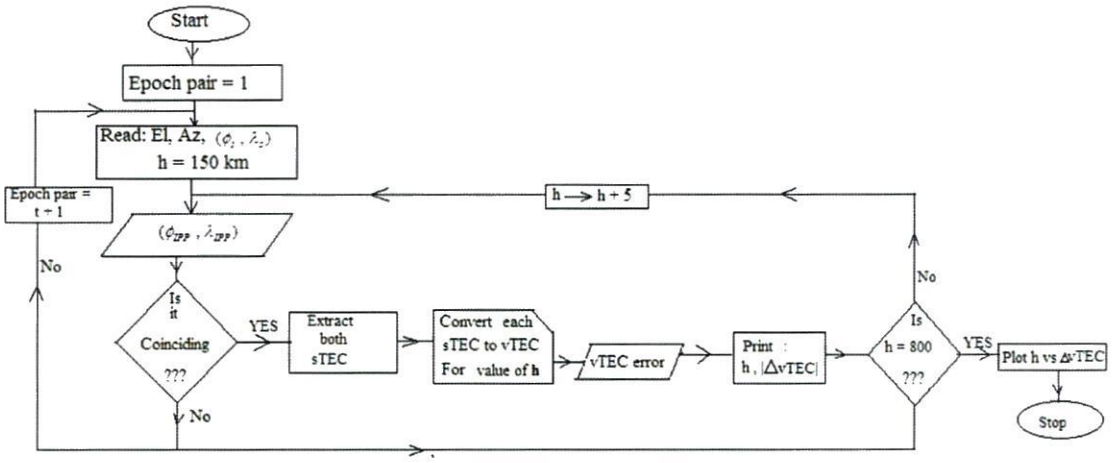


Figure 3.5: Summary of steps followed to determine ionospheric effective height using the coinciding pierce point technique

If the two vTEC values in Equation 3.15 are expressed in terms of sTEC, as indicated in Equation 3.1 and 3.2, $\Delta vTEC$ can be expressed as

$$\Delta\text{vTEC} = \left| \frac{\text{sTEC}_1}{\text{MF}(\chi_1)} - \frac{\text{sTEC}_2}{\text{MF}(\chi_2)} \right|. \tag{3.16}$$

Therefore, the values of the height substituted in Equation 3.12 and Equation 3.4 were adjusted until the difference between the two vTEC values for the two pierce points are minimum, i.e, when ΔvTEC is minimum. The height h_m for which the two VTEC values are equal or have the minimum difference is taken as the effective height.

Generally, the steps followed to determine the value of effective height is summarized using the flow chart in Figure 3.5.

3.3.2.3 Determination of the IPP altitude from IGS-GIMs

The IGS-GIMs technique was used to determine the effective height of the ionosphere for the East African low latitude region. This was done following the approach proposed by Li et al. (2017), i.e,

(i) The absolute value of sTEC of a GNSS satellite was extracted by removing the specific satellite and receiver Differential code biases (DCB) from the directly recorded ionospheric observables (line- of- sight TEC).

(ii) The absolute sTEC obtained was then converted into vTEC using the mapping function for a given value of height h, and this particular vTEC is labelled as vTEC_H.

(iii) The "ground truth" vTEC (vTEC_T) was determined for the hour when the GNSS sTEC was received. This "ground truth" is the vTEC interpolated from GIMs

of the IGS. The standard GIMs TEC for the whole globe, with a resolution of 120 minutes (2 hours), was extracted from IGS Ionosphere Product website. The vTEC over the coordinates of the ground receiver was interpolated to provide $\mathrm{vTEC_T}$ every two hours.

(iv) The root mean square error (rmse) values between the two vTEC values, ($\mathrm{vTEC_H}$ and $\mathrm{vTEC_T}$), at a given height were calculated for all the satellites visible within the two hours of GIMs using the Equation.

$$\mathrm{rmse} = \sqrt{\frac{1}{n}\sum_{i=0}^{n}(\mathrm{vTEC_{H_i}} - \mathrm{vTEC_{T_i}})^2}, \tag{3.17}$$

where n is the number of satellites visible to a given station in the 2 hours.

(v) Finally, the height h substituted in Equation 3.4 was varied between 100 and 1000 km at intervals of 10 km. For each case, the rmse was calculated for all the visible satellites. The height at which the rmse is minimal was considered as the effective height, h_m, of the ionosphere.

3.3.2.4 Comparison of zenith sTEC with oblique sTEC

The zenith-oblique technique (Huang and Yuan, 2013) is based on the principles of the inversion technique described in Section 3.3.2.1, but in this case only a single epoch of the zenith satellite was considered. When using this method over the East African region, two satellites observed simultaneously from a single receiver were considered. One satellite at the zenith ($E \geq 89°$) and the other at an oblique angle of elevation ($30° \leq E \leq 85°$). For a given epoch, TEC recorded by the satellite that is at the zenith was considered as true vTEC ($\mathrm{vTEC_{TR}}$).

The sTEC recorded by the other satellite at an oblique angle of elevation, during the same epoch, is converted to vTEC using Equation 3.4 for a specified height h. This was denoted as $\mathrm{vTEC_{OB}}$. The values of the height h substituted in Equation 3.4 during the conversion ranged from 100 to 1000 km, and this produced different $\mathrm{vTEC_{OB}}$ values for each value of h. The two vTEC values were then compared using graphical analysis to determine the height at which they are equal. The value of h when the two vTEC values are equal ($\mathrm{vTEC_{OB}} = \mathrm{vTEC_{TR}}$), was taken as the effective height, h_m, of the ionosphere.

The four GNSS-TEC techniques all use the mapping function in different ways, which gives room to new techniques that may also be using mapping function in another approach. In this study, a new GNSS-TEC technique is proposed to supplement on the existing GNSS-TEC techniques, and to facilitate cross-validation and provide a

complementary comparison to the four existing techniques. This technique, named as Swarm-IRI TEC technique, is discussed in the following section.

3.3.3 Swarm-IRI TEC Technique

In this technique, sTEC measured simultaneously from the dual-frequency GNSS receiver fixed looking upwards on swarm satellite, and sTEC recorded by a given GNSS receiver on ground when swarm is on a small grid cell of $1.5° \times 1.5°$ over the ground receiver were obtained. The difference between the two sTEC values were calculated to get the sTEC between the ground and the height of swarm satellite (sTEC below swarm satellite). The sTEC below swarm satellite is referred to as TECbs. The values of TECbs were converted into vTEC, and then compared with IRI-TEC integrated from 65 km to the same height as swarm. IRI was chosen because the model relies on data sources from worldwide network of ionosondes, i.e the powerful incoherent scatter radars (Jicamarca, Arecibo, Millstone Hill, Malvern, St. Santin), the topside sounders, and in situ instruments. This provides electron density profiled according to height in the altitude range of 65-2000 km during day-time, and 80-2000 km in the night-time (Shi et al., 2019; Bilitza et al., 2010, 2017; Patel et al., 2019). The IRI TEC was downloaded from the homepage[6]. The procedure followed to determine the effective height using this technique is presented in the following subsection.

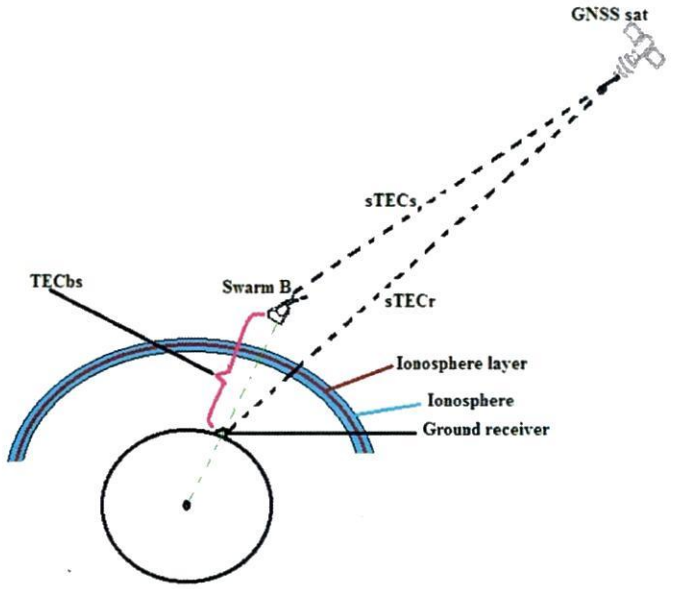


Figure 3.6: Geometry for effective height determination from Swarm satellite and ground receiver

3.3.3.1 Determination of Effective Eeight from Swarm - IRI TEC

The following steps were used to derive effective height of the ionosphere:

[6] http://irimodel.org

(i) The path of swarm satellite (swarm B) was tracked until it was over head a given ground GNSS receiver.

(ii) The absolute sTEC recorded simultaneously by ground station (denoted as sTECr), and by the receiver on board swarm satellite (denoted as sTECs) (see Figure 3.6), were determined.

(iii) TEC below the swarm satellite (TECbs) was then obtained from the difference between sTECs and sTECr (represented in orange in Figure 3.6). This was done only when the GNSS satellites were at an elevation angle between 30^0 and 60^0. For satellites at elevation angles below 30°, there is a risk of losing lock on the ground receiver due to scintillation effects, while at high elevation angles above 60°, the loss of signal is caused by obstruction of the GNSS signal path by swarm satellites.

(iv) TECbs obtained were converted to the vertical component (vTECbs) using a given height in the MF, and the vTEC error determined from the difference between vTECbs and the interpolated IRI_TEC in the same epoch period.

(v) For the same given height h, the vTECbs and it's corresponding vTEC error was determined for all GNSS satellites visible. The root mean square error for all the vTEC errors of the different satellites were obtained.

(vi) The value of height h substituted in Equation 3.4 during conversion of TECbs to vTECbs was varied in steps of 5 km from 100 km up to the height of Swarm B satellite (530 km), and in each case the rmse calculated. The value of h that gives the minimum rmse was taken as the effective height.

3.4 Spatial and Temporal Variation of the Effective Height.

The East African region lies in the low latitude region of the ionosphere that is known for a well developed Equatorial Ionization Anomaly (EIA). This leads to significant variation of TEC, which in turn influences the variation of the ionospheric centre of mass or effective height of the ionosphere, both in space and time (D'ujanga et al., 2013; Opio et al., 2015; Oron et al., 2013; Olwendo et al., 2016). The spatial and temporal variations of the effective height of the ionosphere was investigated. The temporal variation includes diurnal and seasonal changes, while the spatial variation examines the differences in effective height between the crest and trough of the ionization anomaly. These aspects are discussed in the following subsections.

3.4.1 Diurnal variation

To determine the diurnal variation, values of h determined using the different GNSS-TEC techniques described in sections 3.3.2.3 - 3.3.3 were sorted into hourly files and

the modal value of h for each hour considered as effective height of the ionosphere at that hour. This was done for all the 24 hours of the day, using data for the entire year to give the diurnal variation.

Similarly, hmF2 values obtained from ionosondes recorded at an interval of 15 minutes for all the 24 hours of the day over the entire period of the ionograms were used to show the diurnal variation.

3.4.2 Seasonal variation

This was investigated by determining the hourly mean of the measured effective height for a given day. The mean of the hourly values for all the days of a year were grouped into three seasons. December solstice (November, December, January and February), June solstice (May, June, July and August) and Equinox (March, April, September and October). The seasonal variation was analyzed by examining the changes in the mean values of the effective height, h_m, for a specific hour across all the months within each respective season.

3.4.3 Spatial Variation of Effective Height

The spatial variation of the effective height of the ionosphere was investigated using the crest to trough ratio (C2T). The crest to trough ratio is the ratio of values of effective height obtained at the crest to the values of effective height at the trough (McDonald et al., 2011; Zhang et al., 2009). Hourly mean of h for stations at the crest (ARSH, DODM and MTDK) were divided by the hourly mean of h values for stations at the trough (ADIS and NAZR). The variations of C2T gives the spatial variation.

The variation in the effective height of the ionosphere as discussed above, provided a better understanding of the patterns and behavior of the ionosphere. This provided data for modelling the effective height of the ionosphere as discussed in the following section.

3.5 Modelling of Ionospheric Effective Height over East Africa

To model the effective height of the ionosphere, the values of the height, h, obtained from GNSS receiver MAL2 using the different methods discussed in sections 3.3.2.3, 3.3.2.4 and 3.3.3 together with the values of h obtained from the ionograms from Malindi co-located with MAL2 were used. A 15 minute time series of height h from January 1, 2022 to March 31, 2024 was obtained. Any data gap was filled with the value integrated from IRI at that given epoch to give a continuous sizable data for a single station modelling. In modelling, Artificial Neural Networks (ANNs) (Mas and Flores, 2008), was used to study the behavioural patterns of non-linear height parameter

through the storage of information in the interconnections, and later generalising its variations (Mas and Flores, 2008; Shanmuganathan, 2016).

The effective height of the ionosphere at a particular location exhibits temporal variation that can be categorised into periodic and random components (Li et al., 2017). The periodic component (Pr) involves the diurnal and seasonal variations, while the random component (Rr) corresponds to the changes due to solar and magnetic variations. The periodic component is modeled as a function of the hours of the day (diurnal) and day of the year (seasonal) $P_r = f(Hr, doy)$ (Vinnikov et al., 2004).

Basing on the two components of temporal variation, a number of factors could be contributing to the random component of temporal variation. To help determine the extent to which a given solar and magnetic parameter influences the temporal variation of effective height, a regression analysis was first carried out on a number of solar and magnetic parameters. This was useful in getting the most suitable inputs for the final model. The solar and magnetic parameters used in the regression analysis include solar flux f10.7 ($f10.7$), sunspot numbers (ssn), solar wind speed (swp), proton temperature (pnt) and Dst index (Dst). During the regression analysis, the dependent variable h was first expressed as a function of the periodic (Pr) and random (Rr) variables as

$$h = f(P_r, R_r), \tag{3.18}$$

where $P_r = \{Hr, doy\}$ and $R_r = \{f10.7, ssn, pnt, swp, Dst\}$. The seven independent variables were all expressed as a linear combination of the dependent variable h as

$$h = f(Hr, doy, f10.7, ssn, pnt, swp, Dst, A),$$

where A is the matrix of the unknown coefficients of the seven variables. The matrix of the dependent variable can be expressed as

$$h = a_0 + a_1x_1 + a_2x_2 + a_3x_3 + a_4x_4 + ... + a_nx_n, \tag{3.19}$$

where $x_1,\ x_2, ..., x_n$ represent the n-independent variables, a_0 is a constant term, and $a_1, a_2, a_3, ..., a_n$ are the coefficients of the respective independent variables.

In order to allow a continuous numerical trend of the data between the transition of two consecutive days, the two periodic variables (Hr and DoY) were each split into two trigonometric components. The hour (Hr) were split in sine component (Hrs) and cosine component (Hrc), and the day of the year (doy) were split into sine component

(doys) and cosine component (doyc) expressed as

$$\begin{aligned} \text{Hrc} &= a_2 \cos\left(\tfrac{2\pi t}{24}\right) \\ \text{Hrs} &= a_3 \sin\left(\tfrac{2\pi t}{24}\right) \\ \text{doyc} &= a_4 \cos\left(\tfrac{2\pi d}{365.25}\right) \\ \text{doys} &= a_5 \sin\left(\tfrac{2\pi d}{365.25}\right) \end{aligned} \tag{3.20}$$

where t is the time of the day, and d is the DoY.

When the four inputs of the periodic variables in Equation 3.20 were substituted together with the other five solar and magnetic parameter in equation 3.19, a total of nine variables were obtained. This is expressed as

$$h = a_0 + a_1 Hr + a_2 Hrc + a_3 Hrs + a_4 doyc + a_5 doys + a_6 ssn + a_7 f10.7 + a_8 pnt + a_9 swp \tag{3.21}$$

The coefficients a_1, a_2, $a_3, \ldots\ldots\ldots, a_9$, were determined by least square fit of the polynomial h using the following steps.

(i) Formulate the design matrix for the multivariate linear regression of Equation 3.21

$$\mathbf{XA} = \mathbf{h}$$

where

$\mathbf{X}$ is the design matrix,

$\mathbf{a}$ is the vector of coefficients,

$\mathbf{h}$ is the vector for the values of effective height (dependent variable).

The design matrix $\mathbf{X}$ for n data points and the 9 variables is:

$$\mathbf{X} = \begin{pmatrix} 1 & x_{11} & x_{12} & \ldots & x_{19} \\ 1 & x_{21} & x_{22} & \ldots & x_{29} \\ \vdots & \vdots & \vdots & \ddots & \vdots \\ 1 & x_{n1} & x_{n2} & \ldots & x_{n9} \end{pmatrix}$$

The vector of the unknown coefficients A and values of h is:

$$\mathbf{A} = \begin{pmatrix} a_0 \\ a_1 \\ a_2 \\ \vdots \\ a_9 \end{pmatrix} \quad , \quad \mathbf{h} = \begin{pmatrix} h_1 \\ h_2 \\ \vdots \\ h_n \end{pmatrix}$$

(ii) Solve the system of linear equations using the matrix method, i.e,

$$\mathbf{A} = \mathbf{X}^{-1}\mathbf{h}.$$

where, $\mathbf{X}^{-1}$ is the inverse of matrix $\mathbf{X}$.

(iii) Solve for the coefficients $\mathbf{A}$

The values of the coefficients determined correspond to the contribution of a particular independent variable to the variation of the effective height. Hence only independent variables whose contributions are significant (greater than 0.01) were used in the final model development using neural networks. This is discussed in the following subsection.

3.5.1 Artificial Neural Networks Model

The ionosonde dataset based on a single station at Malindi was used to train the model using ANNs. The dataset comprises of h_m values obtained every 15 minutes from a combination of the hmF2 values of the ionosonde (July 2023 - March 2024) and mode of GNSS-TEC values obtained from the station MAL2 co-located with the ionosonde (January 2022 to July 2023). This gave a continuous dataset for the period from January 2022 to March 2024, enough for the ANNs model to learn the pattern. The inputs for the ANN model were chosen from the parameters in the regression analysis (Equation 3.21). The variables with coefficient values greater than 0.01 were considered for ANN model inputs. In this case, six of the nine variables in the regression equation (Hrc, Hrs, Dyc, Dys, ssn and $f10.7$) had coefficient values greater than 0.01, and were used to train the ANN for a single station (Kimura et al., 2019). However, before the training of the whole data was carried out, optimization of the neural network was done to determine the appropriate architecture suitable for the data (Chen and Liu, 2022; Doshi, 2019). The optimization started with dividing the dataset into two: training data set (70%) and validation data set (30%). The training dataset is the one used for training the ANN, while the validation dataset determines the performance of the ANN on patterns of the data that are not trained during learning.

After running the model, the two datasets obtained are the measured and predicted values. The rmse between these measured and predicted values were calculated using the expression.

$$\text{rmse} = \sqrt{\left(\frac{1}{N}\sum_{i=1}^{N}(h_{r_i} - h_{p_i})^2\right)}, \tag{3.22}$$

where $i = 1, 2, ..., N$, N is the total number of observations for a given dataset, h_r is the measured value of a given data set and h_p the predicted value. During parameter optimization, the value of the parameter that minimized the rmse was considered as the most suitable for the ANN architecture.

In ANN, two major parameters define its architecture: the number of neurons in a given layer and the number of hidden layers (Brownlee, 2018; Krishnan, 2022). These two parameters were each optimised using the rmse of the training data set and validation data set. The optimised parameters were then set as the suitable architecture for training the entire data.

After training and evaluating the performance of the model, it was then exported directly to MATLAB using the support from MATLAB that deploys models to .NET applications (Kumar et al., 2019; Li et al., 2024). The exported model was then imported into the .NET environment, where the .NET libraries with compatible frameworks are used to load and utilize the model (Shakouri and Banihashemi, 2019). When the six new inputs are fed into the data, the application then predicts the effective height of the ionosphere for the period specified in the inputs. In this study, MATLAB's support applications was used to carry out predictions using the trained model.

Chapter 4: Results and Discussions

4.1 Introduction

This study focused on the validation of the value of effective height of the ionosphere over the low-latitude region of East Africa. This was achieved through various tools and techniques, and the results obtained are discussed in the following sections.

4.2 Determination of Effective Height of the Ionosphere

The effective height of the ionosphere over a given place is best determined using observations made with vertical incidence ionosondes that give electron density profile with respect to height (Bilitza et al., 2010). Determination of effective height of the ionosphere using ionosonde data is discussed in the following subsection.

4.2.1 Effective Height from Ionosonde

There are two ionosondes found in the East African region: The Vertical Incidence Pulsed Ionospheric Radar (VIPIR) and the Advanced Ionospheric Sounder (AIS). As already mentioned in chapter 3, the VIPIR ionosonde is located in Addis Ababa, Ethiopia, while the AIS is located in Malindi, Kenya. In the following subsection, the results obtained using the ionosonde located at Addis Ababa are presented and discussed.

4.2.1.1 Effective Height from Addis Ababa Ionosonde

The ionosonde at Addis Ababa relays ionograms at an interval of 5 minutes, and the data are stored in the host computer. After being extracted, the ionograms were scaled to reveal several ionospheric parameters for every 5-minute epoch. Two parameters that are most essential for this investigation are the critical frequency (fof2), which is the minimum frequency beyond which the signal passes through the ionosphere fully, and the hmF2 which is the height of the ionospheric layer that corresponds to the critical frequency. The description of how these two parameters are obtained from ionograms is described by the pattern of the curves displayed in a graph of ionospheric height against signal frequency (Figure 4.1). In all the panels of Figure 4.1, the echo of the signal transmitted vertically upwards began to be received from the ionosphere at a height of approximately 90 km, when its frequency reached about 0.1 MHz. This indicates the beginning point of the ionosphere at the distinct time.

The ionosphere is stratified into layers, and each layer of the ionosphere reflects radio waves within a specific frequency range. Higher layers generally reflecting signals of higher frequencies, for example, in Figure 4.1, the signal frequency increases to about 0.5 MHz as the reflection height rises gradually to approximately 100 km, signifying

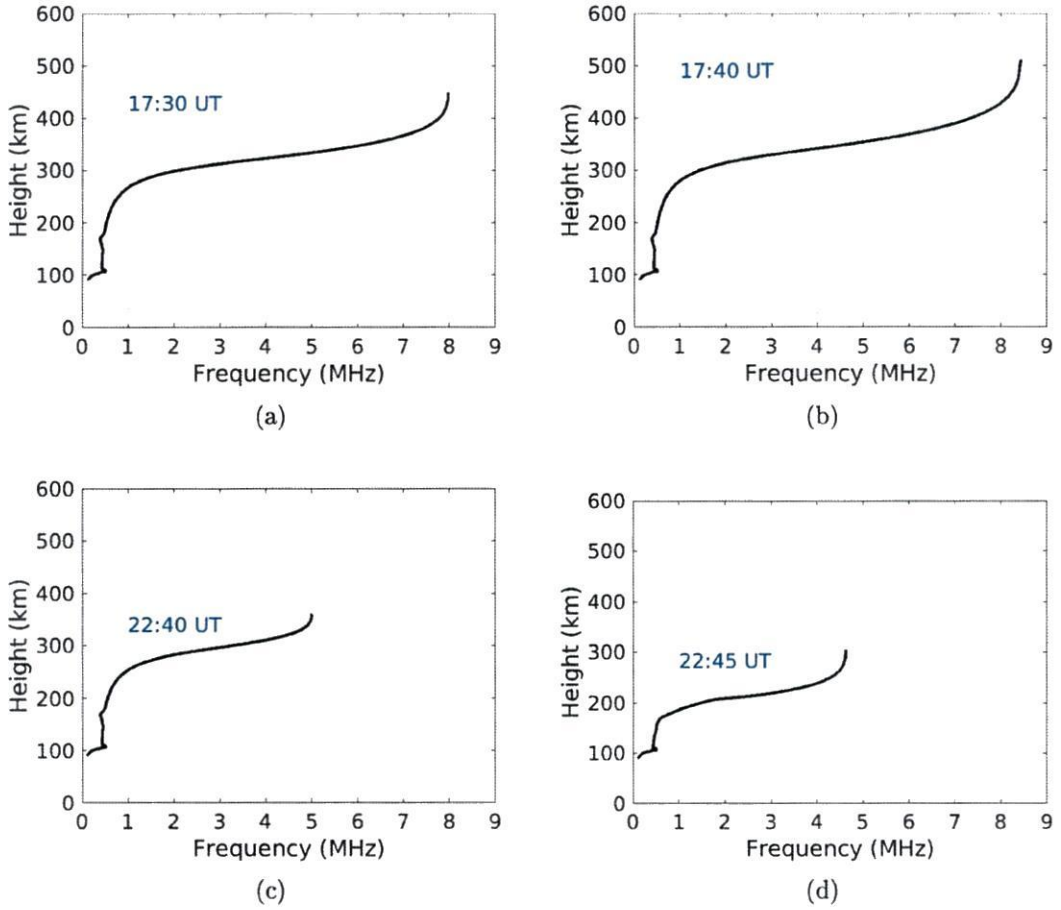


Figure 4.1: The variation of the ionospheric height with frequency at different times of DoY 156. Time indicated on each panel is the epoch of the ionograms. The curves are asymptotic at particular frequencies (critical frequency) corresponding to the hmF2.

the maximum height of the D layer (Bremer, 1998). At the 0.5 MHz, there is a sharp increase in the height of the ionosphere at which the signals are reflected, to about 170 km representing the E-region (Danilov, 2002; Zell, 2015). Beyond a frequency of 0.5 MHz, the reflection height of the ionosphere increased moderately to about 250 km when the frequency reached 1 MHz (Figures 4.1(a), 4.1(b) and 4.1(c)). This indicates the boundary between F1 and F2 layers of the ionosphere (Davies, 1990a). Beyond the 1 MHz frequency, the reflection height gradually increases until it reaches a point where the curve becomes asymptotic. In this frequency range, the signal is reflected at the F2 layer, where the ionosphere is denser. From Figures 4.1(a) and 4.1(b), this behaviour is observed in the frequency range of approximately 1 MHz to 8 MHz, whereas in Figures 4.1(c) and 4.1(d), it is observed from 1 MHz to 5 MHz. Beyond the frequency of the asymptote, the signal penetrates the F2 layer, implying that the critical frequency of the F2 layer (fof2) has been reached. It can be seen that, on DoY 156, the critical frequency as seen in Figure 4.1(a) is about 8 MHz at 17:30 UT, in Figure 4.1(b), critical frequency is about 8.2 MHz at 17:40 UT, while in Figure 4.1(c) and Figure 4.1(d), it is about 5 MHz and 4.6 MHz at 22:40 UT and 22:45

UT respectively. The corresponding effective heights (hmF2) in each of the cases in Figure (4.1(a), 4.1(b), 4.1(c), and 4.1(d)) are about 450 km, 500 km, 360 km and 300 km respectively for the different 5-minute epochs. This is the effective height of the ionosphere at the respective time. Effective height values are higher at 17:30 and 17:40 compared to the values at 22:40 UT and 22:45 UT because of the significant electron loss difference between the two time periods (Titheridge, 1968; Thomson et al., 2021).

Important to note is that the magnitude of fof2 corresponds to the density of the F2 layer at a given time. For example, in Figure 4.1(a) and 4.1(b), the value of fof2 reaches 8 MHz at 17:30 UT, while in figures 4.1(c) and 4.1(d), the value is about 5 MHz at 22:40 UT on the same day. This suggests that the density of the F2 layer is greater at 17:30 UT than at 22:40 UT, which is still due to greater electron loss disparity. The height at which the curve becomes asymptotic to the critical frequency is considered as the value of hmF2 for the particular ionogram of a given time of a day. On a given day, the VIPIR ionosonde is expected to record 288 ionograms. However, due to system malfunction the ionosonde at Addis Ababa was not able to record all the ionograms for the days it was operational as shown in Table 4.1.

In some of the days, as seen in Table 4.1, the number of ionograms recorded were

Table 4.1: Number of Ionograms recorded by Addis Ababa ionosonde in 2014

DoY	Ionograms	DoY	Ionograms	DoY	Ionograms
156	16	166	39	176	00
157	46	167	02	177	00
158	18	168	21	178	00
159	21	169	08	179	15
160	27	170	26	180	12
161	36	171	20	181	04
162	42	172	09	181	00
163	00	173	00		
164	34	174	03		
165	35	175	00		

less than 10, e.g DoY 167, 169, 172, 174, and 181. The highest number of ionograms recorded is 46 on DoY 157. For analysis, the days with atleast 30 ionograms were considered because it would fairly give a better representation of the values of hmF2 of a day. The values of hmF2 were obtained for each ionogram. For the selected days, the values of hmF2 obtained were plotted against the time when the ionograms were recorded, as shown in Figure 4.2. The mean value of hmF2 for each selected day was determined and this value exceeds 350 km. For example, on DoY 157, the mean hmF2 registered is 389 km, on DoY 161 the mean was 371 km, while for DoY 162 and 166, the respective values of the mean hmF2 were 400 km and 376 km. This was repeated for all days where the number of ionograms is above 30 and the mean value of hmF2 for all the days considered was higher than 350 km

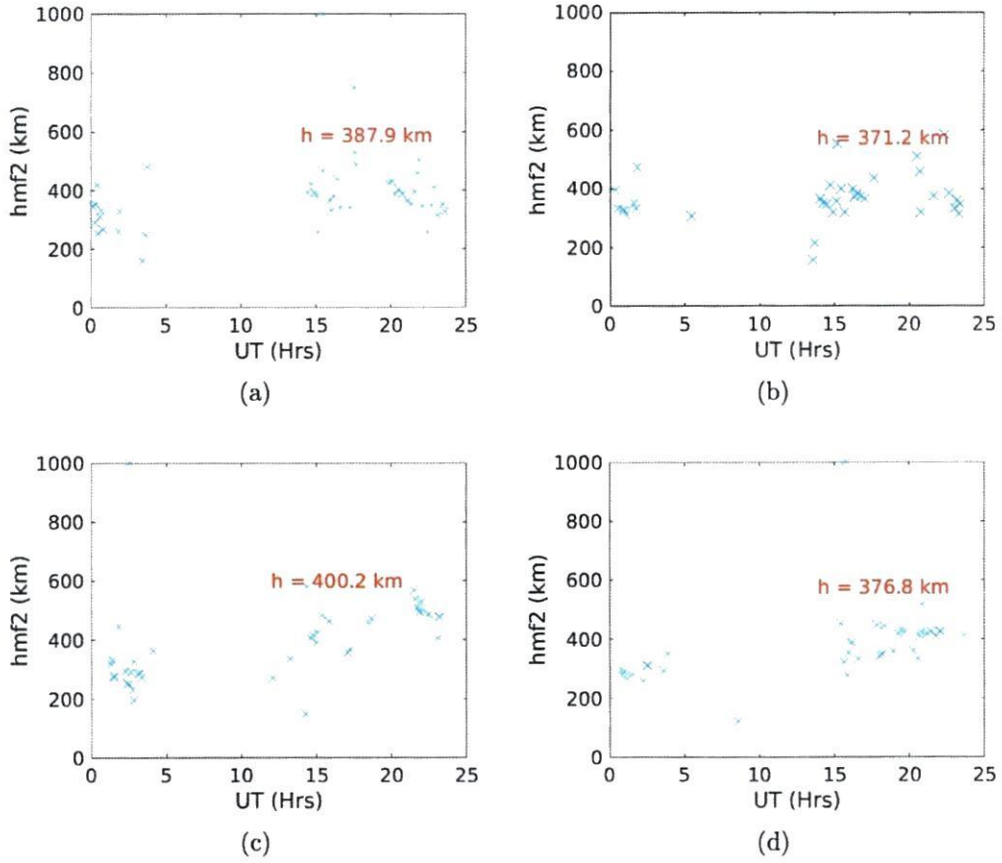


Figure 4.2: Values of hmF2 recorded at the Addis ababa for the different epochs on DoY 157 panel (a), DoY 161 (b), DoY 162 (c) and DoY 166 (d). The mean of hmF2 values for a given day is represented by h, and printed at the center of each panel.

Unfortunately, the ionosonde at Addis Ababa broke down by August 3, 2014, and the East African region did not have other reliable ionosondes for monitoring the ionosphere until July 23, 2023 when the AIS ionosonde was installed in Malindi by the INGV team. The AIS ionosonde has data for the period of August 2023 to date. The data between the period of August 2023 to March 2024 was used to determine the hmF2. The results obtained from the AIS ionosonde is discussed in the following subsections.

4.2.1.2 Effective Height from Malindi Ionosonde

The ionograms recorded at Malindi were obtained and processed as described in section 3.3.1. The processed ionograms for each day contained 38 parameters presented in 38 columns. For each ionogram in this study, three specific parameters were considered, namely: time when ionogram was recorded, frequency of the reflection signals to determine the critical frequency of the F2 layer (fof2), and the height at which the signals are reflected to reveal the height of the peak electron density (hmF2). These parameters were considered because of their relevancy to the study. Unlike the Addis

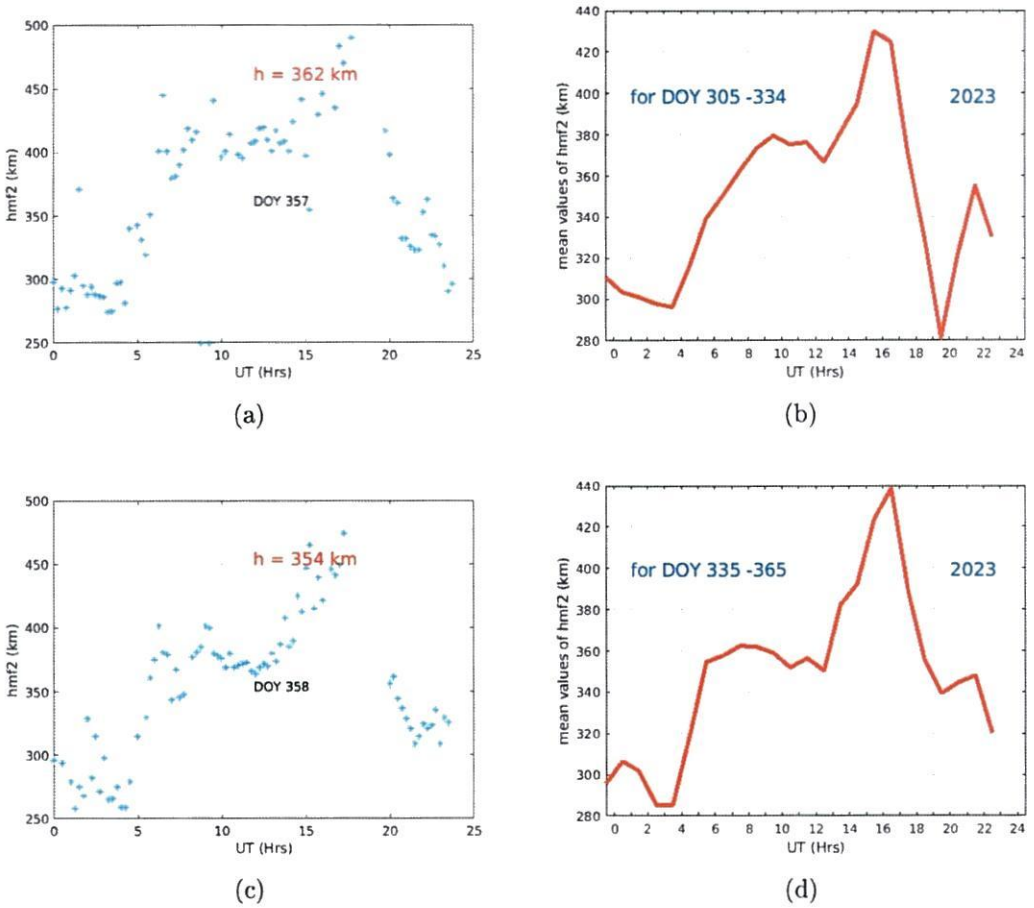


Figure 4.3: Variation of AIS ionosonde values of hmF2 with time of the day in 2023. The left side panels (4.3(a) and 4.3(c)) are for single days, while the right hand panels (4.3(b) and 4.3(d)) are hourly mean for a month

Ababa ionosonde, the one at Malindi registers ionograms after every 15 minutes. This imply that for a given day, 96 ionograms are expected over Malindi station. The values of hmF2 and fof2 were obtained from each ionogram of a given day. The variation of hmF2 and fof2 with time are presented in Figure 4.3. The results indicate that the effective height of the ionosphere on a given day lies in a range. For example, on DoY 357 (Figure 4.3(a)), the range is between 250 km to 490 km, and for Doy 358 (Figure 4.3(c)), the range is between 250 km and 470 km. Similarly the right hand panels indicate that the mean values of the hmF2 for a given month lie in a range of 280 km - 430 km for the month of November 2023 (Figure 4.3(b)) and 282 km - 440 km for the month of December (Figure 4.3(d)), respectively.

The hmF2 values for the two locations in the East African region were extracted from all the ionograms recorded during the entire operational period of the stations, and the modal values were determined. The results are shown in Table 4.2. The modal value of the hmF2 values in both cases is greater than 350 km. Important to note from the table is that the modal value registered at Addis Ababa in 2014 is higher than

the modal value registered at Malindi in 2023-2024. This could be attributed to solar activity since the year 2014 was the period of solar maximum for the solar cycle 24.

Table 4.2: Modal values of hmF2 obtained from all ionograms registered at the two locations

Ionosonde location	**Year of operation**	**Period of recorded ionograms**	**Number of ionograms recorded**	**Modal value of hmF2**
Addis Ababa	2014	June 5, 2014 to Aug 3, 2014	472	423.5
Malindi	2023 to date	Jul 13, 2023 to Aug 31, 2024	31826	384.2

The result obtained from the ionosondes is always regarded as the most accurate value of effective height of the ionosphere. But in places where there are no ionosondes, alternative techniques that use GNSS-TEC have been suggested. In this thesis, the suggested GNSS-TEC techniques have been tested over the East African region using data for the years of 2014 and 2016 when most GNSS receivers had data for many days. The results are discussed in the following subsections.

4.2.2 Effective Height from GNSS-TEC Techniques

GNSS-TEC techniques for determining effective height of the ionosphere were introduced to supplement ionosondes and to be an alternative in places where these ionosondes may not be in existence or have no data. The techniques rely on a special function known as the mapping function (MF) given in Equation 3.4, which is used to convert sTEC to vTEC. The MF is useful for estimating the effective height of the ionosphere. From Equation 3.4, the MF depends on the elevation angle of the GNSS satellite and the ionospheric height h. In order to use MF to determine the ionospheric height, the second parameter, elevation angle must be defined.

To examine the effect of elevation angle on the mapping function, a quiet day in 2014 (DoY 005) was selected, during which the ionosphere is presumed to be influenced only by its daily variation, without the impact of other external factors. The data of this particular day from one station in the region MBAR was used. The satellite passes over Mbarara on this particular day (DoY 5) were tracked to identify a satellite observed by the ground receiver for longer hours (at least 8 hours). The results are shown in Figure 4.4. Satellites visible for over 8 hours were selected, as the maximum duration for a complete satellite pass is 12 hours. In this case satellites identified by PRN 1, 3, 6, 11, 17,18, 22, 25, 27 and 28 were considered (Figure 4.4). On this particular day (DoY 5), satellite identified by PRN 6 which was visible for a longer time (11 hours) was considered to investigate the effect of elevation angle of a satellite on the MF. This was repeated for other quiet days in the same year, i.e, DoY 137 from station MBAR, and DoY 257 from station NURK. In this case satellites identified by PRN 25 and PRN

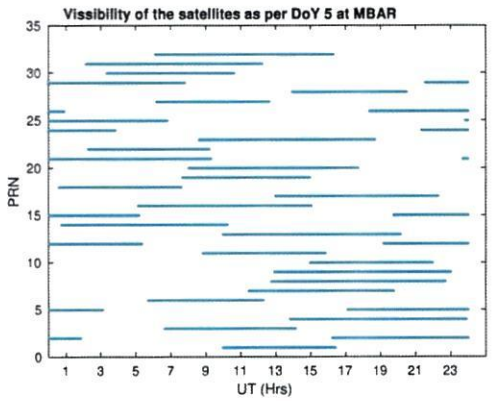


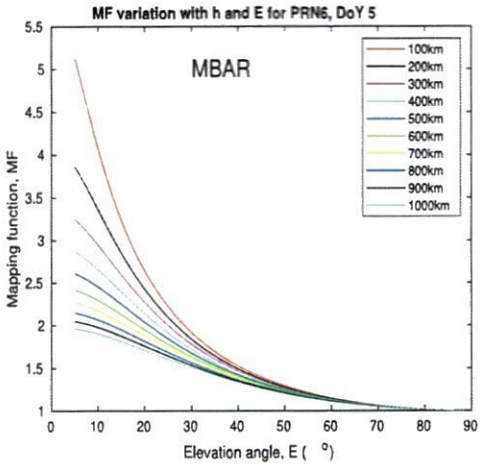
Figure 4.4: Visibility duration of all the satellites at the station MBAR on DoY 5

26 were considered because they were visible for more than 8 hours.

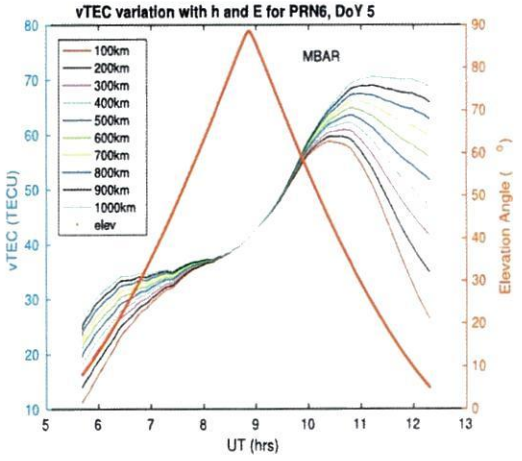
For each of the PRNs considered, the variation of MF with elevation angle at a particular ionospheric height was determined. The study also looked at how the vTEC determined from the selected satellite varies with time as it's elevation angle changes. The results are shown in Figure 4.5. From the left side panels (4.5(a), 4.5(c) and 4.5(e)), the values of MF for elevation angles less than 40° are different at each ionospheric height. i.e., for very low elevation angles, the MF value of about 5.7 at a height of 100 km and a value of 2 at a height of 1000 km is observed. These values are significantly different from height to height. However, for elevation angles greater than 40°, all the curves for the different heights are very close to each other. This means that, at high elevation angles, the mapping function is almost the same. Any slight difference is entirely due to the value of the ionospheric height considered. Therefore, if one is to rely on a mapping function value to estimate the effective height of the ionosphere, h_m, the elevation angle of the GNSS satellite should be set at a value greater than 40°.

Similarly, the curves on right hand panels (4.5(b), 4.5(d), 4.5(f)) show significantly different values of vTEC as a function of elevation angle for a given value of sTEC. It is observed that between 08:00 UT and 10:00 UT in Figure 4.5(b), between 18:00 and 20:00 UT in Figure 4.5(d) and between 03:00 UT and 05:00 UT in Figure 4.5(f), the curves representing vTEC are very close to each other for higher elevation angles. However, when elevation angles are below 40°, the vTEC values computed at different heights show significantly high deviation of about 25 TEC units in Figure 4.5(b), about 30 TECU in Figure 4.5(d) and Figure 4.5(f). This also suggests that, higher elevation angles are suitable for use in the MF.

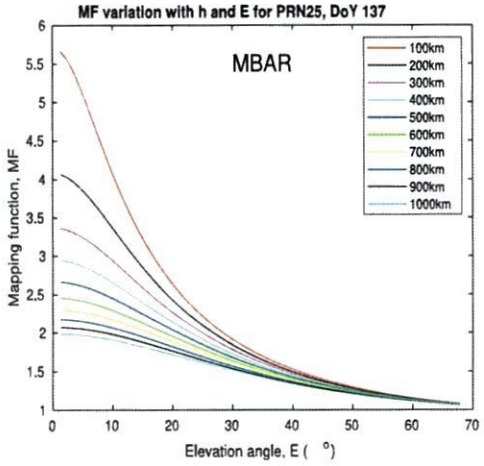
Therefore, both panels suggest that the contribution of ionospheric height h to the values of mapping function in the East African region is significant when the satellite elevation angle used in the height dependant mapping function exceed 40°. In addition, low elevation angles are associated with signal errors due to some factors such as



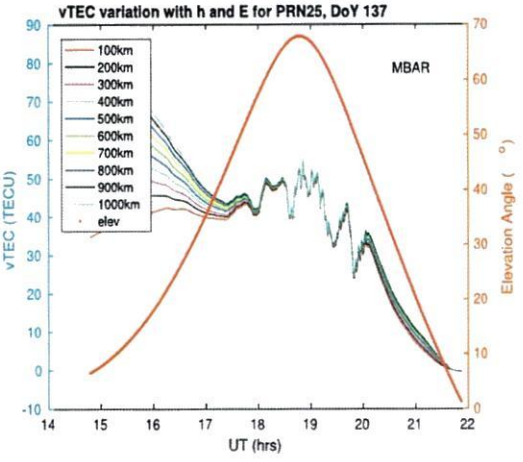
(a)



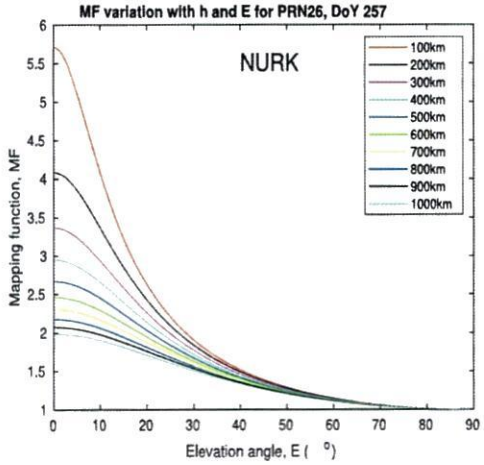
(b)



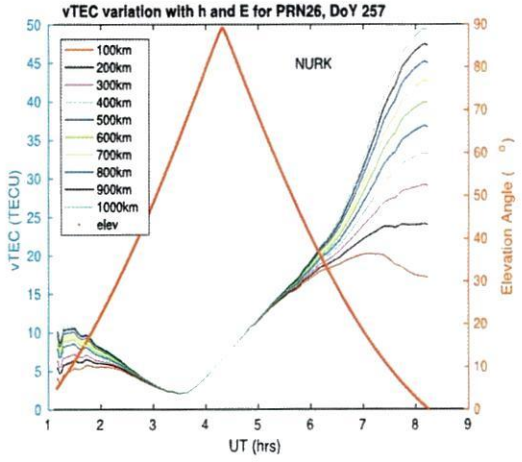
(c)



(d)



(e)



(f)

Figure 4.5: The effect of elevation angle on mapping function and vTEC. The left side panels (4.5(a), 4.5(c) and 4.5(e)) show the variation of mapping function with satellite elevation angles. The right hand panels (4.5(b), 4.5(d) and 4.5(f)) show the variation of vTEC with elevation angle. In both cases, each curve is for a particular value of the height substituted in the MF.

multipath (Moore et al., 2014), which can give wrong values of the effective height of the ionosphere, h_m, deduced from the mapping function. Hence in this study, a threshold elevation angle of 40° was used in the GNSS-TEC techniques discussed in the following subsections.

4.2.2.1 Inversion Technique

This was the first GNSS method proposed by Birch et al. (2002), and it was first employed in the mid-latitude region to estimate the shell height. The value obtained for the mid-latitude region was in the range of 700 km to 1200 km. To test this technique over the East African region, MAL2 data for the year 2014 were used, and pairs of satellites, one along the zenith and the other at a slant path that relayed data simultaneously to the IGS station MAL2, were identified (Elevation angle E of zenith satellite is greater than 85° and for slant satellite $40^o < E < 85^o$). For all the satellite pairs that meet the criteria stated, a scatter plot of the TEC recorded at the zenith (zTEC) versus that at the slant path (sTEC) was created, and the line of best fit was determined for each. The gradient m, of the line of best fit was obtained for each pair of the satellites. The results for the different days are presented in Table 4.3, and Figure 4.6.

Table 4.3: Slant to zenith inversion estimate of the effective height over MAL2 for the days of 2014. The columns included are the correlation coefficient, the slope (m) obtained from regression fit, mean elevation angle of the slant and zenith satellite pass, the mean time of the pass, and the height (h) computed with the help of Equation 3.4.

Doy	Zenith PRN	Slant PRN	Mean UT	Mean Azimuth	Mean elevation	sTEC of slant PRN	sTEC of Zenith PRN	No. of pts	corr. Coef	m	h (km)
1	18	12	4.5542	194.61	61.287	26.635	14.255	76	0.99789	0.31044	999
1	24	21	1.2583	219.53	56.621	11.617	4.4282	17	0.97308	0.15419	547
3	24	15	0.85417	236.06	57.679	5.2038	0.92104	48	-0.33757	-0.04125	140
3	24	21	1.1208	219.46	56.668	11.073	1.0794	16	-0.9746	-0.1104	388
4	24	21	1.05	219.63	56.689	12.804	2.1541	17	0.99043	0.10977	386
5	24	21	0.98333	219.48	56.707	11.438	4.0341	17	0.99576	0.12888	454
6	24	21	0.9125	219.65	56.727	18.715	6.3289	18	0.99764	0.18224	647
7	24	15	0.575	236.78	57.716	18.99	8.3845	47	0.31074	0.058133	198
7	24	21	0.84167	219.72	56.753	19.95	8.5359	17	-0.94266	-0.0413	144
8	24	21	0.77083	219.88	56.774	17.297	8.4278	18	0.98661	0.13983	492
9	24	5	0.27083	219.83	57.564	12.023	6.125	6	-0.03292	-0.0212	72
9	24	15	0.4625	233.69	57.821	12.504	6.1783	40	0.92087	0.24554	859
9	24	21	0.70417	219.72	56.795	16.073	6.4528	18	-0.97205	-0.11959	420
10	24	15	0.36667	237.27	57.764	14.778	7.5122	45	0.44943	0.098673	336
10	24	21	0.63333	219.93	56.827	18.541	7.2837	19	0.98188	0.10576	370
11	24	21	0.5625	219.94	56.844	12.619	5.3467	18	0.96041	0.058663	204
12	24	21	0.49583	219.77	56.864	25.651	15.826	18	0.97836	0.16486	582
13	24	21	0.43333	219.28	56.883	16.838	11.481	17	0.87823	0.047101	164
14	24	21	0.35833	219.76	56.907	18.428	5.9326	19	0.97408	0.055884	194
15	24	21	0.28333	220.17	56.936	22.017	9.3947	19	0.97184	0.10557	368
16	18	12	3.525	187.73	61.447	13.625	5.4519	77	0.99945	0.29502	940
16	24	21	0.21667	219.99	56.958	17.807	8.1847	19	0.94032	0.077915	271
17	24	21	0.14583	220.17	56.978	27.826	10.151	20	0.99442	0.092458	322
17	25	12	3.1125	99.086	63.138	4.8283	4.4917	6	0.79286	0.19132	561

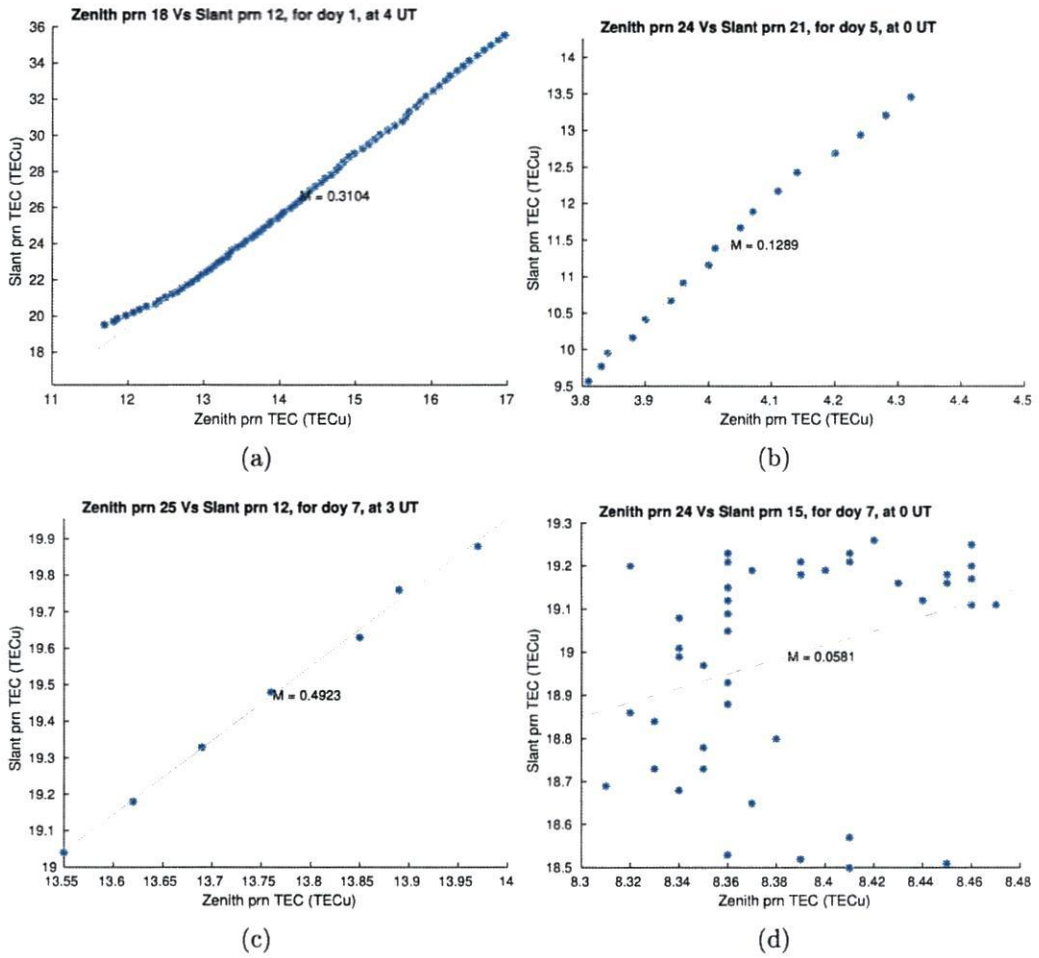


Figure 4.6: Scatter plot of slant TEC vs vTEC over station MAL2. The figures show the gradient m in each plot used to estimate h.

From Table 4.3, the values of the gradient m are significantly different for the different pairs of satellites, and this results in different values of h. For example, DoY 001 shows that the satellite pair 18/12 had a gradient of 0.31044 which gives a value of h to be 999 km. This can also be seen in Figure 4.6(a).

In addition, there are cases where the visibility duration of the two satellites are too long (more than 10 minutes) as seen by high number of points in column 8 of Table 4.3. For example satellite pair 18/12 on DoY 001 recorded 76 epochs (approximately 30 minutes), another pair 24/21 on DoY 016 was visible for longer period, recording 77 data points, and pair 24/15 on DoY 007 for almost 20 minutes (47 points). Similarly, in some cases, the technique produced negative gradients when the TEC recorded by the zenith satellites keep reducing with epoch, while that of slant pass instead increased for the same ionosphere. The negative gradient obtained by Birch et al. (2002), were attributed to several factors related to the shell height of the ionosphere. These factors included changes in temperature, humidity, or other environmental variables that could influence measurements, inaccuracies or inconsistencies in the data collection process. For example, satellite pair 18/12 and 24/15 and 24/15 on DoY 003. On another note,

the correlation coefficient of some pairs are too low (less than 0.4), indicating that the TEC recorded by both satellites in each epoch are completely random. e.g satellite pair 24/15 on DoY 007 in Figure 4.6(d). This was attributed to the specific statistical or analytical techniques used.

Comparison of height from Inversion technique and ionosonde

To check the effectiveness of this particular GNSS-TEC technique, the value of effective height obtained from this GNSS-TEC technique is compared with ionosonde values, because hmF2 from the ionosondes is considered to be more accurate. This requires a station co-located with an ionosonde. As already mention in the previous subsection, the data used to test various GNSS-TEC techniques was for 2014, and the only ionosonde with available data in that year was located in Addis Ababa. An IGS station (ADIS) co-located with the ionosonde was considered. From already known literature, (e.g Zell (2015)), the concentration of electron density in the ionosphere cannot peak at a height less than 200 km. Therefore values of height less than 200 km (like what is shown in Table 4.3) were not considered.

The effective height obtained from Addis Ababa ionosonde for the days with considerable number of ionograms as mentioned earlier and ADIS-IGS station for the different DoY are presented in Figure 4.7. The value of effective height obtained using the

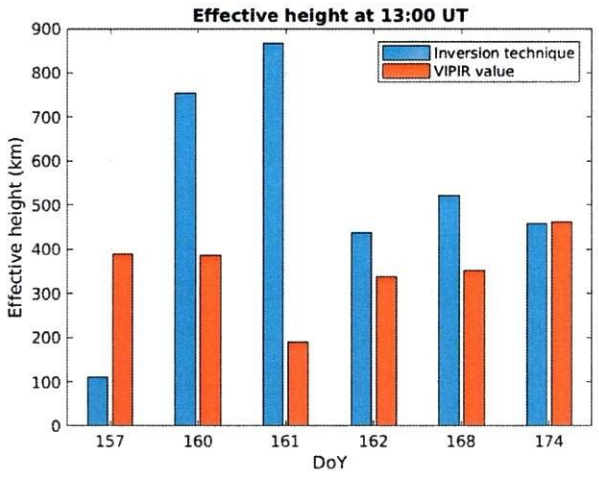


Figure 4.7: Comparison of height obtained from the Addis Ababa ionosonde and inversion technique at 13:00 UT, for selected days in 2014

inversion technique for this particular hour of 13:00 UT is higher than the ionosonde values for most of the days represented in Figure 4.7. For example on DoY 160, inversion technique gave a value of 730 km when ionosonde had 400 km.

The inversion technique was applied to data from GNSS stations that had more than 200 days of available data for the entire year of 2014. The height h values obtained

Table 4.4: Modal values of effective height from GNSS stations having data for more than 200 days in 2014

GNSS Station	No. of days with data	No. of satellite pairs	Modal values of h
MAL2	363	3212	412
ADIS	336	2841	428
MBAR	364	3173	391
MTDK	336	1964	385
DODM	350	2848	368
NURK	335	1836	431

from different satellite pairs at a single station were sorted, and any values less than 200 km or greater than 1000 km were excluded. The modal values of the remaining h measurements from the selected stations are summarized in Table 4.4. The modal value of effective height from each station in Table 4.4 is greater than 350 km.

4.2.2.2 Coinciding Pierce Point Technique

In this technique, pairs of stations at a distance not more than 1000 km apart as recommended in the studt by Li et al. (2017) were identified. In this case the station pair MAL2 & RCMN was selected. Random values of h, ranging from 100 km to 1000 km, were used to calculate the respective IPP coordinates of two satellites visible at a given epoch using Equation 3.12. The IPP coordinates calculated were each tested for coinciding for a given PRN pair, epoch by epoch, using Equation 3.11. For any pair that coincides, the sTEC of each satellite was converted into vTEC using the height dependent MF (Equation 3.4). The difference between the two vTEC values (vTEC error) for a satellite pair at a given epoch was determined. The height h at which the two satellites are considered to coincide is varied between 100 km to 1000 km until the vTEC error is minimum. Figure 4.8 shows some of the results obtained using the method of coinciding pierce point. It can be seen from the figure that the vTEC error reduces to a minimum at a given height. The height at which the vTEC error is minimum is considered as the effective height of the ionosphere h_m. From the result, the effective height of the ionosphere on DoY 001 is about 355 km at 06:00 UT (Figure 4.8(a)), and 385 km on DoY 003 at 02:00 UT, 420 km on DoY 004 at 13:00 UT and 435 km on DoY 005 at 13:00 UT in Figures 4.8(b), 4.8(c), and 4.8(d) respectively. The method yields reliable results as long as the pair of satellites that meet the condition of "coinciding" can be got for a given hour of the day.

To analyse the condition for coinciding further, the IPP coordinates were calculated for different values of height h for a given day, and the number of coinciding pairs determined for each height. The results are shown in Figure 4.9. The number of pairs meeting the condition for coinciding (Figure 4.9(a)), increases with height, e.g at a height of 120 km, the number of coinciding pairs is 100 and the number increased to

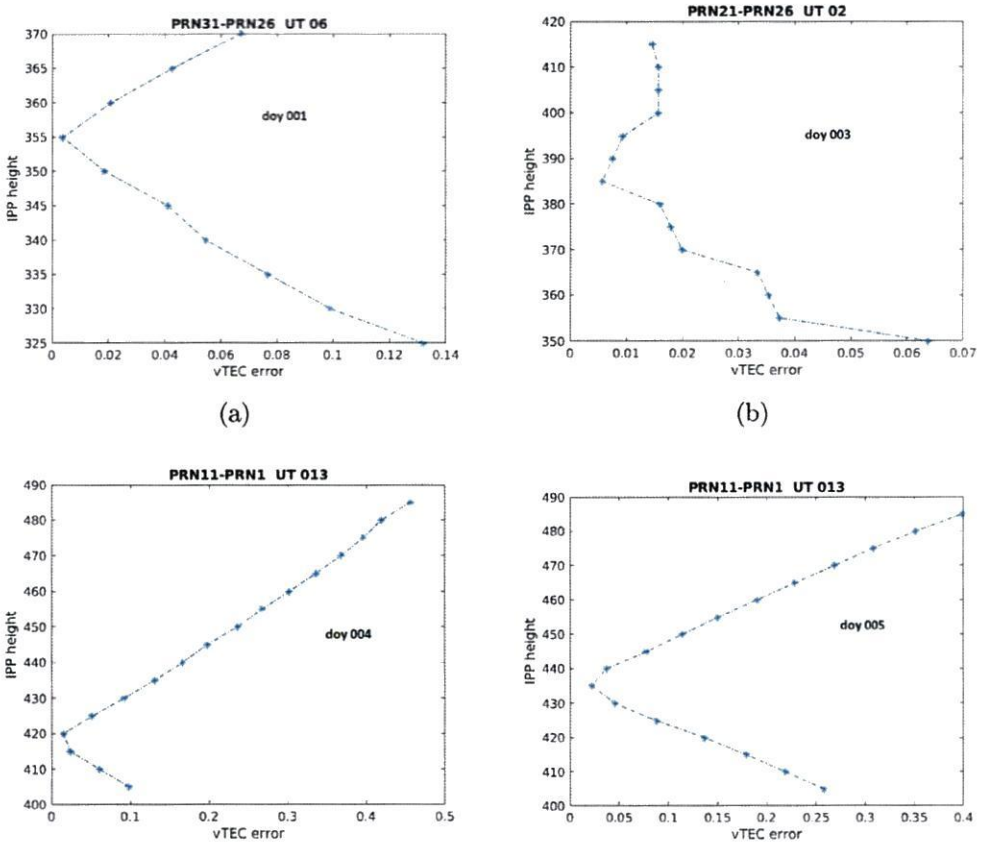


Figure 4.8: Variation of vTEC error with IPP height for a pair of stations MAL2-RCMN in some selected days of January 2016 (DoY 001, 003, 004 and 005) using coinciding pierce point technique.

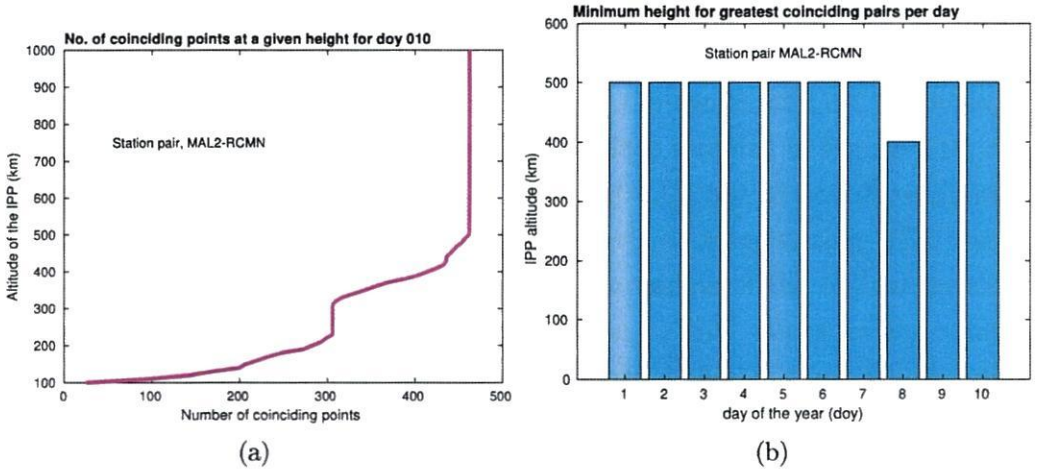


Figure 4.9: Relationship between number of coinciding pairs with IPP height chosen over MAL2-RCMN station pair. Figure 4.9(a) shows variation of the number of coinciding points with the value of height h chosen on DoY 10, 2016. Figure 4.9(b) shows minimum height for the highest number of pairs in the different DoY

200 when the height is about 150 km. The increase continued steadily and became constant at a height of 500 km. Beyond this height, the number of coinciding pairs did

not change. This indicates that the height of 500 km is the maximum height beyond which the number of coinciding pairs will never change. Therefore, to apply coinciding pierce point technique, the effective height of the ionosphere is expected to be below 500 km. Similarly, from Figure 4.9(b), the maximum IPP altitude is 500 km for the 9 days out of 10, with only DoY 008 showing 400 km.

4.2.2.3 Zenith - Oblique Single Epoch sTEC Technique

For this technique, satellite passes for a day over the station MAL2 were tracked until one given satellite is directly at the zenith (Elevation angle of 89^o or 90^o). The TEC registered by the zenith satellite was recorded the vTEC at that moment. For the same epoch, the sTEC registered by another satellite at an elevation angle between 40^o and 80^o was recorded. The sTEC was then converted into its vertical component using Equation 3.4 for a given height h. The two vTEC values (one for zenith satellite and the other for slant satellite) are compared, and found to be different. The difference was tagged to the value of h substituted in the MF during conversion. The h in the MF was adjusted to different values, ranging between 100 km to 1000 km, and in each case vTEC of the slant satellite is calculated. A graph of vTEC against height was then plotted. A horizontal line representing the vTEC of the zenith satellite was then superposed in the same graph as shown in Figure 4.10. The blue dotted marks are the vTEC values obtained, while the horizontal line is the vTEC obtained from the zenith satellite. The height at which the best line of fit of the converted vTEC value intersects with the vTEC of the zenith satellite is considered as the effective height of the ionosphere at that moment. For each epoch, the value of effective height is printed at the center of the figure. It can be seen that the values of the effective height are unique for each hour and day. What is important to note is that, for this method, it's normally one particular satellite that appears at the zenith at that particular time, irrespective of the day. For example, for the four days sampled in Figure 4.10, its only PRN 18 that is observed at the zenith around 02:00 UT for all the days. It was able to pair up with other satellites at an oblique angle, each registering TEC that gives unique values of height, depending on the elevation angle of the oblique satellite. In some cases, two slant satellites can register different sTEC values for the same time. For example, on DoY 4 (Figure 4.10(c) and Figure 4.10(e)), there are two different values of the effective height obtained for the same time, 02:00 UT. The two satellites produced different values of height for the same hour. This may have resulted from the variations in the line-of-sight paths through the ionosphere and potential measurement errors affecting the instruments of the two slant satellites (PRN 10 and PRN 12) (Bidaine and Warnant, 2009).

Comparison of single epoch technique with ionosonde

The ionosonde at Addis Ababa that archived some data in June 2014 was used to

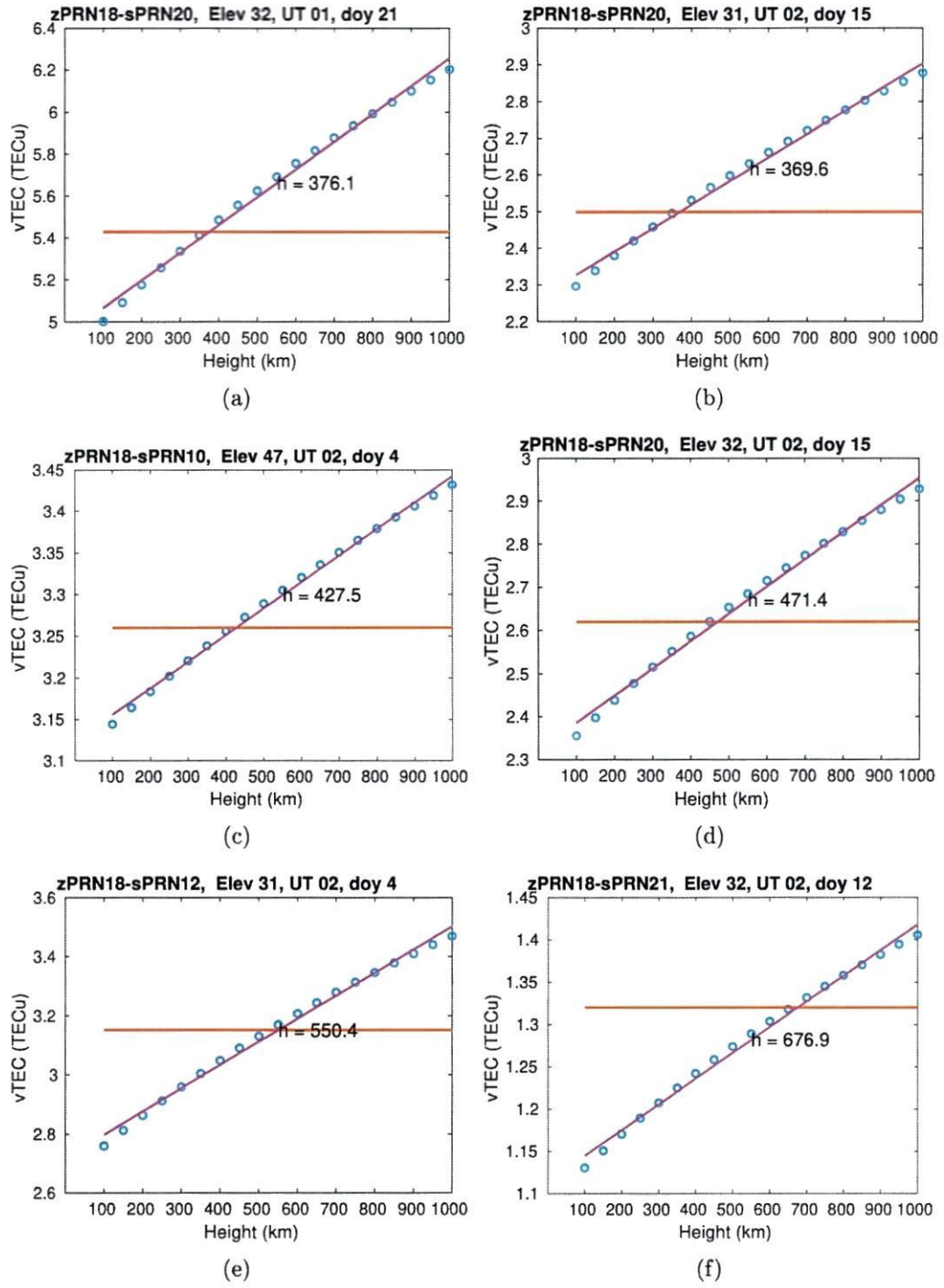


Figure 4.10: Sample results for the days of the year 2016 (004, 012, 015 and 021) from station MAL2 using single epoch technique. The red horizontal line is the vTEC for the Zenith satellite.

compare the zenith - oblique single epoch GNSS-TEC technique. Using the GNSS station ADIS, values of effective height obtained at 17:00 UT using the single - epoch GNSS-TEC technique were compared with the hmF2 from the ionosonde. The results are presented in Figure 4.11.

For the three days shown in Figure 4.11, the values of h obtained using single epoch

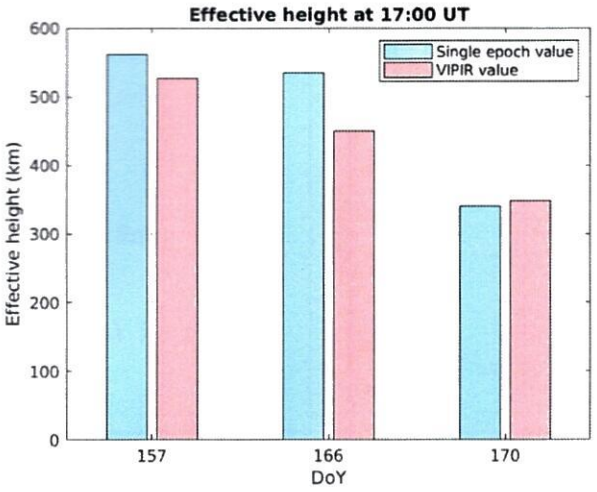


Figure 4.11: Comparison of height got from Addis Ababa ionosonde and zenith - oblique single epoch technique in 2014

technique at 17:00 UT are slightly higher than the ionosonde values. This could be attributed to the errors that arose from the analytical technique used in the single epoch method.

4.2.2.4 IGS-GIMS Technique

This technique was tested using days of the year 2014 when the station MAL2 had full data. The sTEC derived from each GNSS satellite visible to station MAL2 at a given hour was converted to vTEC using a random value of h (Equation 3.4). For a given value of h, the difference between the calculated vTEC from a given visible satellite and the vTEC obtained from GIMs (considered as true vTEC) was obtained to give the error in the vTEC. The rmse of vTEC for all the satellites visible in the period of temporal resolution of GIMs (2 hours) is then determined for the same value of h. The process was repeated for varying values of height h, and in each case, a value of rmse obtained. A graph of height against rmse values was plotted, and the value of height at which the rmse is minimum was taken as the effective height. Figure 4.12 shows the results of particular epochs for the four days chosen. It can be noted that the rmse values for a given GIMs epoch period is higher for lower values of h. For example at a height of 100 km, the value is about 16.5 TECu (Figure 14.12(a)) and 19.2 for Figure 14.12(b). As h is increased, the value of rmse reduces gradually to a minimum at a height regarded as the effective height of the ionosphere (h_m) at that time. In Figure 14.12(a), the ionospheric effective height at 10:00 UT, for the DoY 001 is 450 km, and the effective height on DoY 002 in Figure 14.12(b) is 425 km for the same time of the day. Similarly, for the DoY 003 at 00:00 UT (Figure 14.12(c)), the height is 345 km, while on DoY 004 at 22:00 UT (Figure 14.12(d)) the effective height is 470 km.

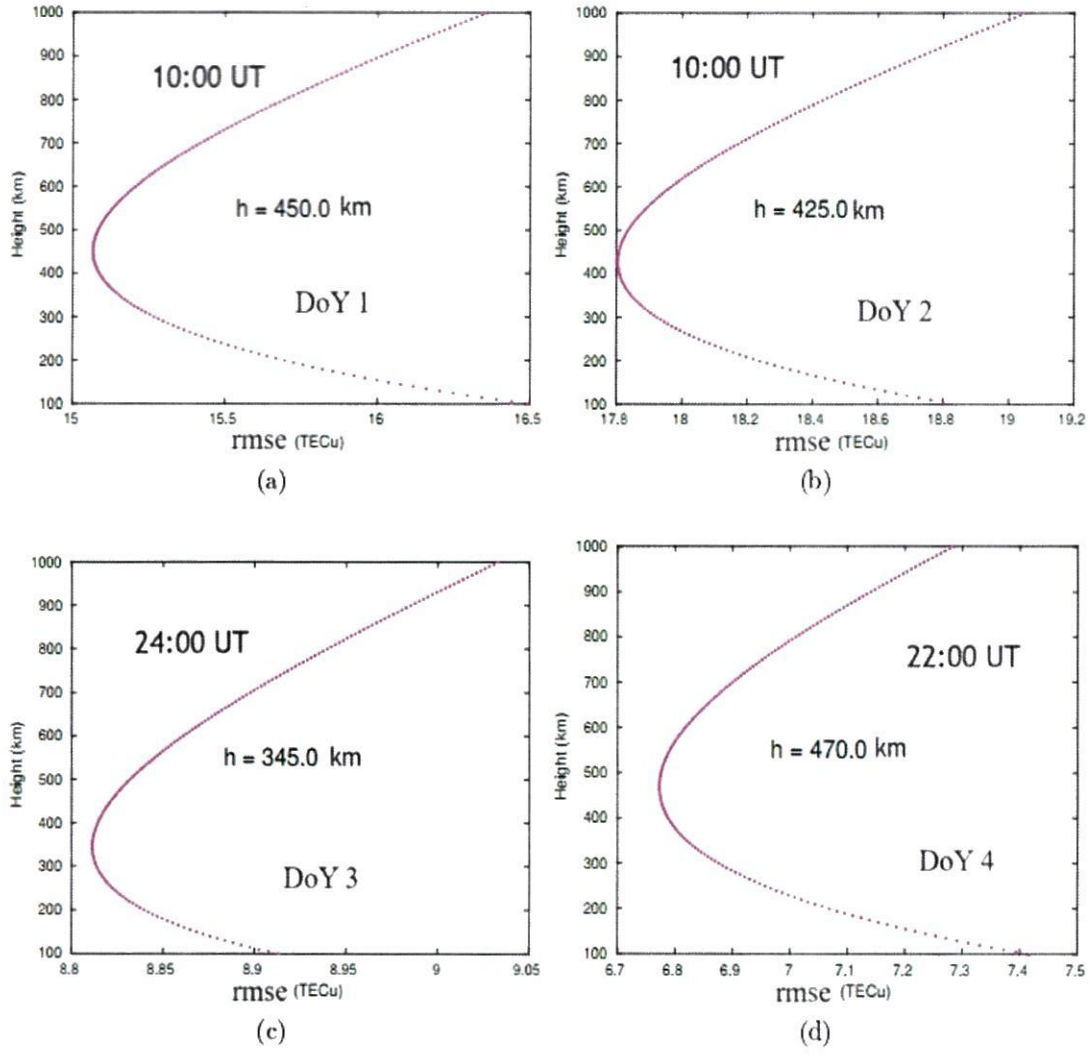


Figure 4.12: Variation of ionospheric height with rmse of the two vTEC values for different days.

4.2.2.5 Swarm-IRI Technique

Data from Swarm B for the year 2016 was used to test the Swarm-IRI technique over ground GNSS station MAL2. Swarm satellite passes were tracked and the time when it passes overhead the ground station was recorded. The IRI data for the time when swarm is overhead the ground receiver was used to calculate IRI-TEC by integrating electron density from height of 65 km to the height of swarm B satellite (530 km). Using the steps listed in section 3.3.3.1, TECbs was obtained for all the moments when Swarm satellite passed overhead MAL2 station in 2016. However, the value of TECbs obtained represents the portion of GNSS slant TEC in the height between the ground receiver and swarm B satellite, meanwhile IRI-TEC represents the vertical TEC in the same height range from the ground to the height of swarm B satellite. Since IRI-TEC are modelled values and TECbs are measured values, a validation relationship was first established between the two values. This was done by a scatter plot of TECbs

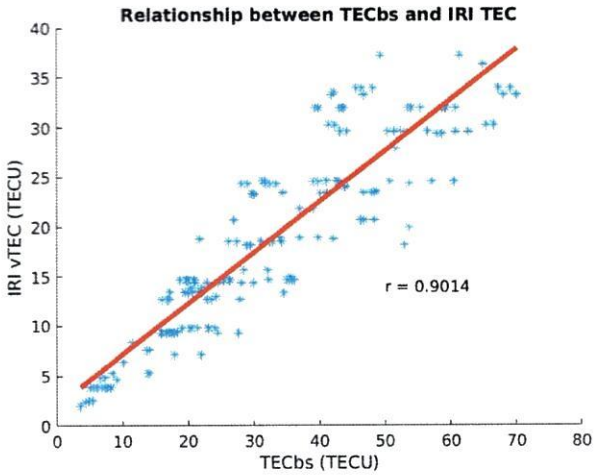


Figure 4.13: Comparison of TECbs obtained from Swarm B and MAL2 with IRI TEC for 122 points of all the epochs when swarm B passes over MAL2 in 2016. The rsme = 18.4901 TECu

obtained in 2016 against IRI-TEC integrated at the respective epochs of TECbs, and a regression analysis between the two carried out. The results are shown in Figure 4.13. From the figure, a correlation coefficient of 0.9104 was obtained, implying that there is a very high positive correlation between IRI-TEC and TECbs. Therefore IRI-TEC can be used together with TECbs to determine the ionospheric effective height as described in the Swarm-IRI-TEC technique.

To ensure that the days selected for testing the different GNSS-TEC techniques belonged to the same ionospheric season, the evaluation used days that matched those chosen in the other techniques. The steps described in section 3.3.3.1 were applied for each selected day, and the results are shown in Figure 4.14 and Table 4.5.
The results show that, for a given epoch, both the swarm satellite and the GNSS ground receiver were observing similar GNSS satellites that are near each other. For example, at 05:39 on DoY 002 (see Table 4.5), both Swarm and MAL2 receiver were observing PRNs 16, 21 and 22. But the TEC recorded by the ground receiver (MAL2) when in the same line of sight with swarm receiver for PRN 16, is 26.780 TECU. This value is much lower than the TEC values recorded at the same time, like in PRN 16 and PRN 21 for the same epoch. Therefore only TEC recorded for the epochs when the two receivers are receiving signals from two different satellites were used. For example, in Figure 4.14(a), when swarm B was receiving a signal from PRN 5, the MAL2 ground GNSS receiver was receiving signal from PRN 2 at the same time. TECbs is obtained for the pair considered and then converted to vTEC. The vTEC error is calculated from the difference between the vTEC computed and IRI-TEC. The rmse of vTEC for all satellite pairs in a given epoch were determined. The values of h substituted in MF were adjusted, and in each case rmse calculated. The height substituted in the mapping function is considered the effective height of the ionosphere at that epoch if the rmse

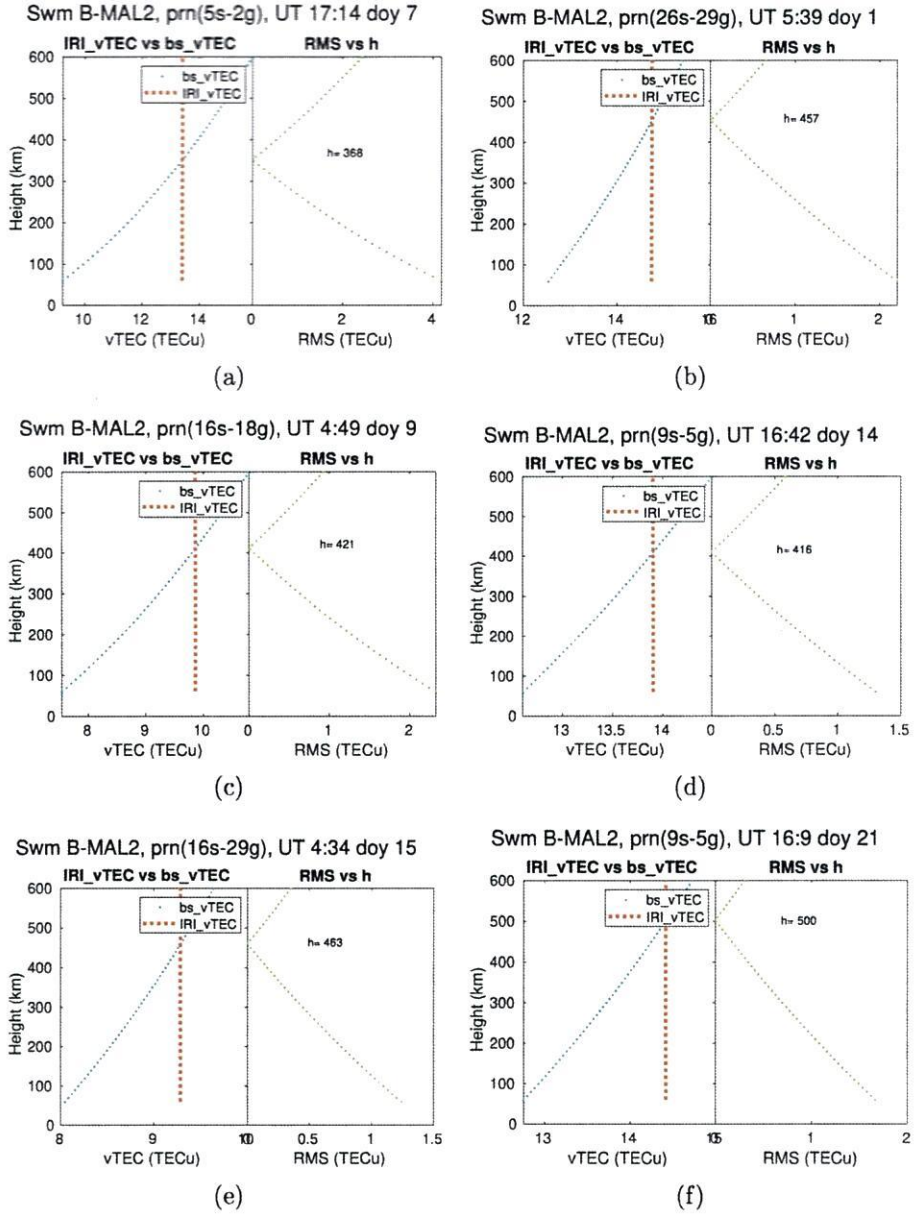


Figure 4.14: Variation of ionospheric height h obtained using SWARM-IGS technique with vTEC. The left subplot of each of the figures 4.14(a) to 4.14(d) shows the effective height obtained from the intersection of the lines bs_vTEC (vertical component of TECbs) and IRI-TEC integrated from IRI. The right hand subplot is rmse of the bs_vTEC for the visible satellites plotted against height.

is minimum. The value of the effective height is different for the different hours and days. For example, at 17:00 UT in Figure 4.14(a), the effective height registered is 368 km. For the other days of the year in Figure 4.14(b), 4.14(e), 4.14(f) and 4.14(c), the values of effective height are 457 km at 05:00 UT, 421 km at 04:00 UT, 316 km at 16:00 UT, 463 km at 04:00 UT and 500 km at 16:00 UT respectively.

Comparison of the effective height obtained from the swarm-IRI method with the value of effective height obtained using ionosonde

The mean value of hmF2 for a given hour was obtained from Addis Ababa ionosonde

Table 4.5: Sample results for three different days showing satellites that were visible to both Swarm and ground receiver. The parameters included are the TEC recorded simultaneously by swarm and ground receiver MAL2.

DoY	Epoch Time (UT)	prn seen by swarm	prn seen by mal2	prn pairs	Average Elevation	TEC by Swarm	TEC mal2
002	05:39:29.88	16, 22	16, 21	16/21	33.4	5.9328	42.1288
				16/16	37.7	5.9328	26.7800
				21/16	38	6.7504	38.0600
				22/21	32	6.7504	42.1200
007	17:14:31.20	5, 6, 9	2, 5, 6, 9	5/2	33	15.5120	50.1300
				5/5	33.8	15.5120	22.0500
				5/6	31.2	15.5120	34.5600
				9/5	34.5	13.039	33.0500
				6/9	30.4	13.0390	34.5600
008	05:07:0.12	10, 26	10, 18	10/10	33.8	5.8827	18.8100
				10/18	31.1	5.8827	38.0300
				26/10	34.5	5.8827	27.0600

for the days with available data in the year 2014. However, for all the days with data, only three days (DoY 157, 168 and 179) had considerable data for at least 5 hours as shown in Table 4.6. The swarm-IRI method can only provide two values in a day since swarm satellite passes over a given ground receiver only twice a day. Therefore, to compare the value of effective height obtained using this technique with ionosonde values, a GNSS receiver (ADIS) at the same location as the ionosonde system was used, and the TEC it registered in the year 2014 was determined. The swarm-IRI method was then applied and the results are shown in Figure 4.15.

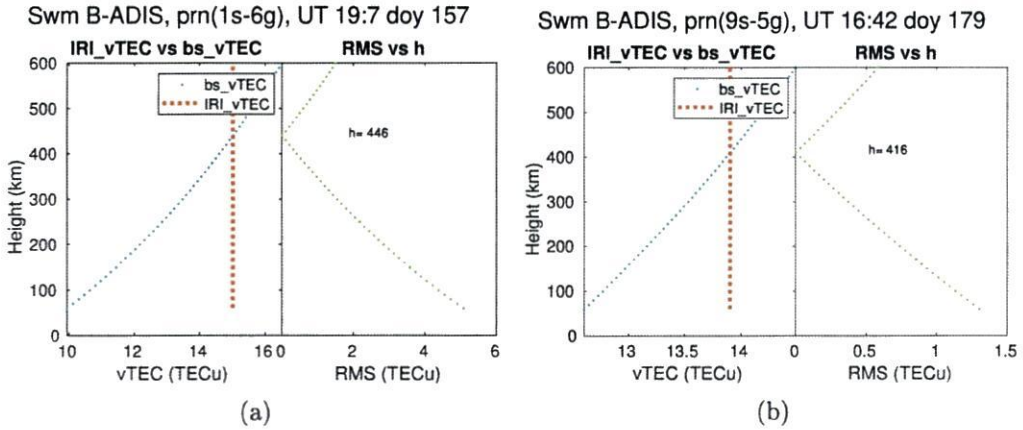


Figure 4.15: Swarm-IRI technique values of effective height at a given hour for particular days of 2014.

The value of effective height obtained on DoY 157 at 19:00 UT using the swarm-IRI method in Figure 4.15(a), is 446 km, while the mean value of hmF2 at 19:00 UT recorded by the Addis Ababa station at the same hour shown in the Table 4.6 is 426 km. These two values are very close to each other. Similarly for the DoY 179, the

Table 4.6: Mean values of hmF2 for a given hour recorded by Addis Ababa ionosonde in 2014. The values of effective height obtained by Swarm- IRI technique is represented in blue. The dash in the table indicate no single data for that given hour.

Time(UT)		00	01	02	03	04	...	14	15	16	17	18	19	20	21	22	23
DoY 157 h(km)	**hmF2 values**	318	290	-	296	-	-	374	378	371	451	-	426	399	406	334	-
	Swm-IRI h-values												446				
DoY 168 h(km)	**hmF2 values**	-	-	-	-	-	-	-	-	-	-	380	382	401	350	310	290
	Swm-IRI h-values														363		
DoY 179 h(km)	**hmF2 values**	-	261	378	364	-	341	416	409	392	400	-	-	-	-	-	
	Swm-IRI h-values					392				416							

Swarm-IRI technique effective height at 16:00 UT is 416 km in Fig. 4.15(b). This corresponds with the hmF2 of 409 km at the same time of 16:00 UT.

Additionally, processed ionograms for the month of September 2023 (the month when the system had stabilized), collected by the recently installed AIS-INGV ionosonde in Malindi, were used to validate the Swarm-IRI technique. The values of hmF2 recorded in the month of September were obtained and compared with TECbs over MAL2 for the same period. Since swarm satellite passes over a given location twice a day, two values of the height h, were derived using the swarm-IRI method for each day. The results of the first nine days of the month of September are presented in Table 4.7.

Table 4.7: Values of hmF2 for a given hour recorded at Malindi Ionosonde in Sept. 2023 and Swarm-IRI Values

Days	doy 244		doy 245		doy 246		doy 247		doy 248		doy 249		doy 250		doy 251		doy 252	
Time(UT)	05	17	04	16	04	16	03	15	03	15	02	14	02	14	01	13	01	13
AIS hmF2 (km)	280	375	270	388	282	375	259	369	276	379	288	340	293	401	–	377	275	397
Swm-IRI h (km)	314	356	292	391	278	359	280	354	306	391	302	342	318	395	317	394	306	413

The results of the swarm-IRI method and that of the ionosonde in Table 4.7 show a similar trend. According to Figure 4.16, the two values are having a very high positive correlation, with correlation coefficient of 0.94. This demonstrates that the swarm-IRI

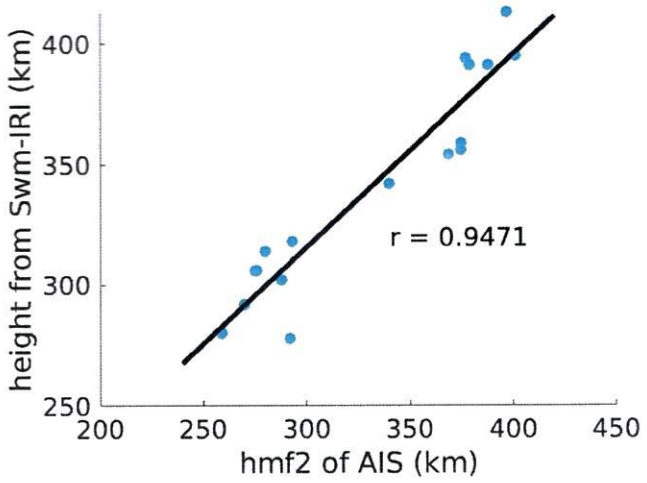


Figure 4.16: Scatter Plot Showing the Correlation Between AIS hmF2 and effective height obtained by Swarm-IRI technique over MAL2 in Sept 2023

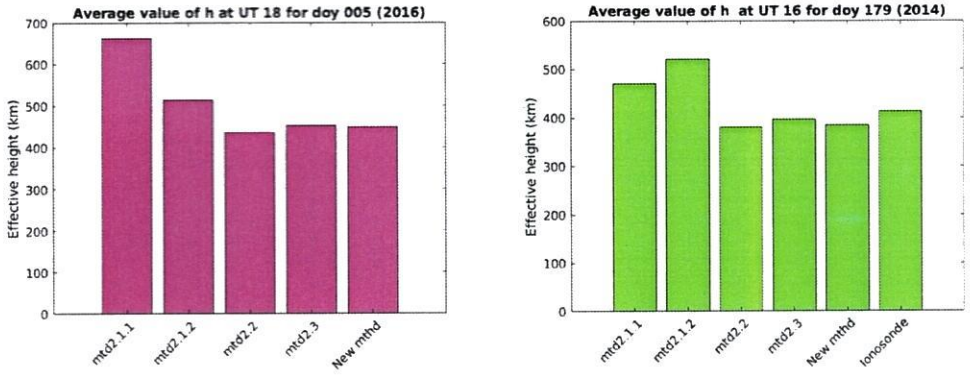
method can also be used to estimate the effective height of the ionosphere.

Comparison of swarm-IRI technique with other GNSS techniques

To compare the results from the swarm-IRI method with the other four GNSS techniques discussed earlier, a particular hour of a day when all the methods had results was identified. This was done using data for the years 2014 and 2016. For the year 2016, all the four techniques had results at the hour of 18:00 UT on DoY 005. The results at 18:00 UT for each of the four GNSS-TEC techniques is presented in a bar graph (Figure 4.17(a)). It can be seen that on the DoY 005, the values of the effective height h_m at 18:00 UT (Figure 4.17(a)) for the different GNSS-TEC techniques are: 660 km for the inversion technique (mtd2.1.1), 510 km for the single epoch technique (mtd2.1.2), 430 km for the coinciding IPP technique (mtd2.2), 450 km for IGS-GIMs technique (mtd2.3) and the Swarm-IRI technique (new mthd).

Similarly, for the year 2014, the different GNSS-TEC techniques had results at 16:00 UT on the DoY 179, including VIPIR ionosonde. The modal value of the effective height h at the respective hour of the day was obtained. The results are presented in bar graphs shown in Figure 4.17(b). On DoY 179, the modal value at 16:00 UT is 480 km for inversion technique, 515 km for single epoch technique, 390 km for coinciding IPP technique, 400 km for GIMs technique, 410 km for the swarm-IRI technique, and the VIPIR ionosonde gave 400 km.

The values of effective height obtained from the different techniques provided enough data points to investigate the spatial and temporal variations of effective height. These variations are discussed in the following section.



(a) DoY 005 2016 (b) DoY 179 2014

Figure 4.17: The ionospheric effective height obtained by the different methods. Figure 4.17(a) shows values of effective height of the different GNSS-TEC techniques. Figure 4.17(b) is model value of h for each GNSS-TEC and the VIPIR ionosonde.

4.3 Spatio-Temporal Variations of Effective Height Over East Africa

The temporal and spatial variations of effective height over East Africa were studied by analyzing the values of effective height derived from the different GNSS-TEC techniques and ionograms recorded at Malindi. The results of the temporal variations are presented in the next two subsections.

4.3.1 Diurnal Variation of Efective Height

Diurnal variation was investigated using both GNSS-TEC techniques and ionosonde values. To study the diurnal pattern using GNSS-TEC, quiet days of the year 2014 (kp $\leq$ 1.3) were identified, i.e days when the ionosphere is under geomagnetic quiet conditions. Data for 288 quiet days of the year 2014 were processed from five receivers that had data in almost all the quite days of the year 2014. The stations listed by their four letter codes are MBAR, MTDK, NURK, MAL2 and ADIS. From each station, the value of h was determined by employing the different techniques described in subsection 4.2.2. The values of h recorded in each epoch from the GNSS-TEC techniques were stored in hourly files for all the quiet days in that year. In each hourly file, the model value of the effective height registered by the different GNSS-TEC techniques was considered as the value of effective height for that particular hour. The model value was considered in order to eliminate the effect of outliers in the data. This was done for all the 24 hours of the day. The results are represented in a graph of effective height against time of the day (Figure 4.18). From Figure 4.18, the minimum height of about 340 km is observed at 04:00 UT, corresponding to sunrise. The value rises gradually to the first peak of about 460 km at 10:00 UT and to the second peak of about 500 km at 14:00 UT, after which it starts to fall gradually to about 370 km at 20:00 UT. According to Chuo and Lei (2014), the gradual increase

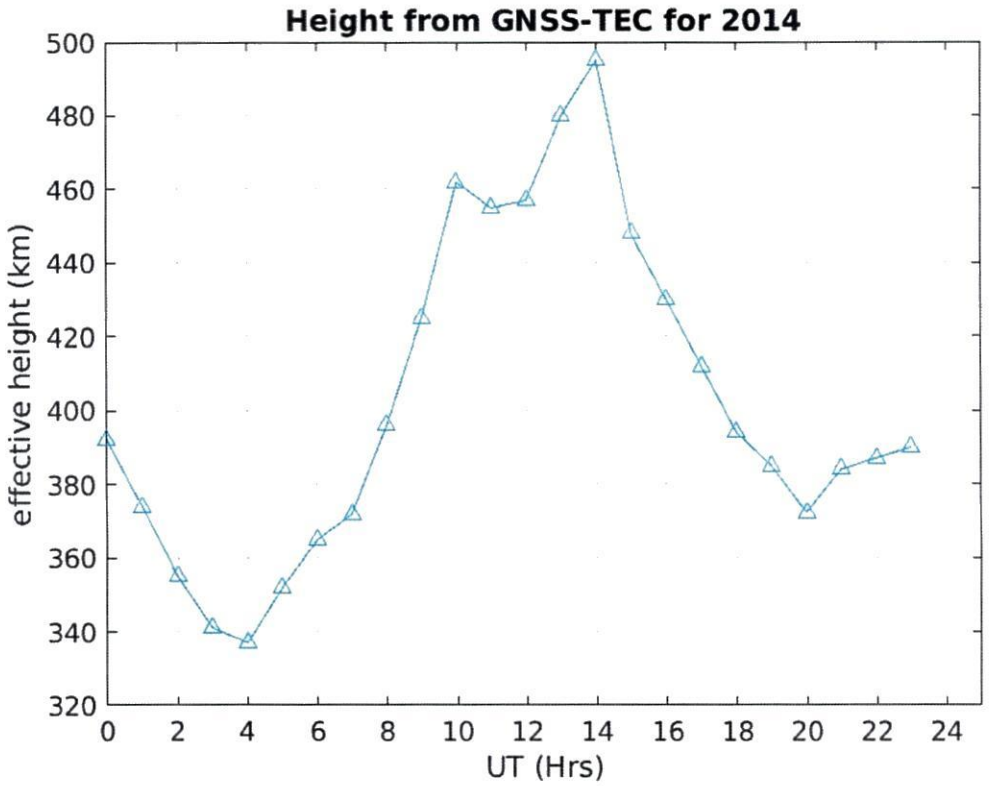
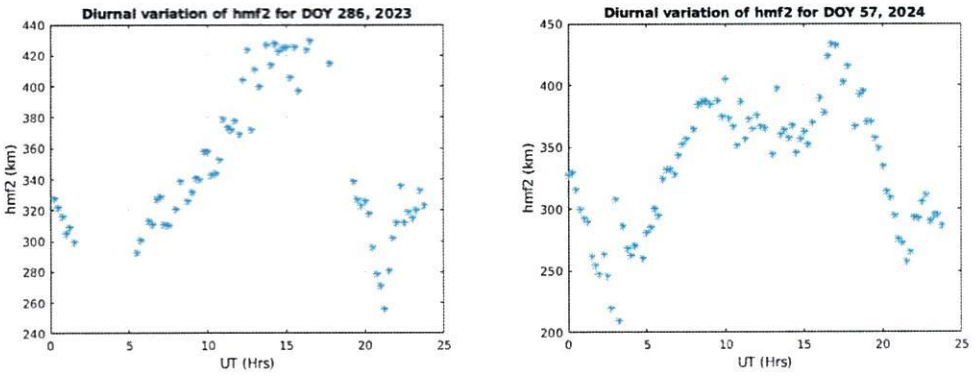


Figure 4.18: Diurnal variation of effective height of the ionosphere

in the ionospheric effective height after sunrise is associated with photoionization and meridional wind. During the day, the meridional neutral wind blows towards the poles, and this causes particles in the upper part of the atmosphere (the ionosphere) to move down to lower altitudes (Khadka et al., 2018). At the same time, the bottom side ionospheric electron density still increases due to photoionization, resulting in increase in $[O^+]$ and uplift of the F2 layer to higher altitudes. The loss rate is thus reduced, and eventually an increase in the effective height of the ionosphere. This observation is in agreement with the diurnal variation of TEC over the East African region reported in studies by Olwendo et al. (2016), Opio et al. (2015), Oron et al. (2013), D'ujanga et al. (2013). This is because ions produced at high altitudes during the day maintain a sizeable density of electrons at the F2 peak throughout the day-time and then diffuse downward at night.

On the other hand, the values of hmF2 obtained at the Addis Ababa ionosonde for the same year 2014 did not cover all the hours of the day. It was not possible to use it in investigating the diurnal pattern. Instead, the study used the hmF2 results obtained from the AIS ionosonde in the year 2023. For each day, the ionosonde at Malindi recorded a number of ionograms from August 2023 to date. In each day, a diurnal pattern is exhibited. For example, in some of the random days of the year 2023, the variation of effective height with time of the day is presented in Figure 4.19. The values of hmF2 exhibit a diurnal variation. The minimum value is observed at about 04:00



(a) (b)

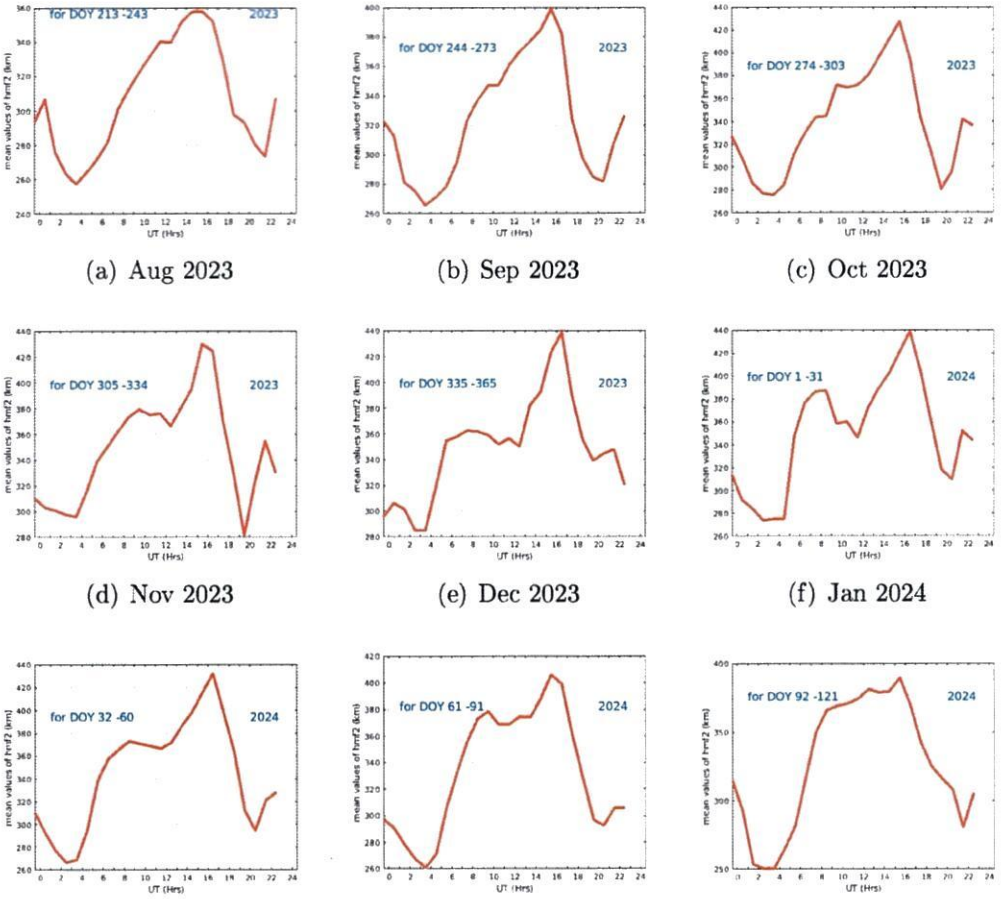
Figure 4.19: Diurnal variation of hmF2 from ionosonde for two given days.

UT, followed by a gradual increase to the first maximum at 10:00 UT. There is a slight reduction between 10:00 UT to 13:00 UT, after which there is a sharp increase to a new maximum at around 16:00 UT higher than the previous maximum. The value then falls rapidly to the second minimum at about 21:00 UT. This is a direct indication of hmF2 dependence on the equatorial dynamics (Jiang et al., 2023). The first maximum and minimum are purely due to the solar zenith angle that influences ionization of the gas molecules. The second maximum is associated with the $E \times B$ drift of the daytime ionosphere (Withers et al., 2023).

Similarly, the hmF2 values from the ionosonde at Malindi were averaged hourly for each month from August 2023 to April 2024. The results are shown in Figure 4.20. The hourly average of hmF2 in all the months showed a variation with time of the day. The peak highest values occurred between 14:00 UT to 16:00 UT. The first minimum occurred at around 03:00 UT in all the months presented and the second minimum at around 21:00 UT. This is a typical diurnal pattern exhibited even by TEC over the region as discussed in several studies e.g (D'ujanga et al., 2013; Opio et al., 2015; Olwendo et al., 2016).

4.3.2 Seasonal Variation of Effective Height

Seasonal variations were analyzed using data from both GNSS-TEC techniques and the ionosonde. The effective height values for GNSS-TEC techniques collected at station MAL2 (co-located with the ionosonde) throughout 2022 were saved in daily files after cleaning, with outliers removed. In each daily files, the values of h were binned in 6 hour intervals (to have considarable data points) for all the 366 days of 2022. The results are presented in Figure 4.21(a). Similarly, the values of hmF2 at Malindi ionosonde registered from August 1, 2023 to July 31, 2024, were binned in 12 hour intervals (due several data gaps) and the results are presented in Figure 4.21(b). From Figure 4.21, effective height of the ionosphere demonstrates a seasonal variation with lowest values during the June solstice. There are relatively higher values at the equinox. However,



(a) Aug 2023 (b) Sep 2023 (c) Oct 2023

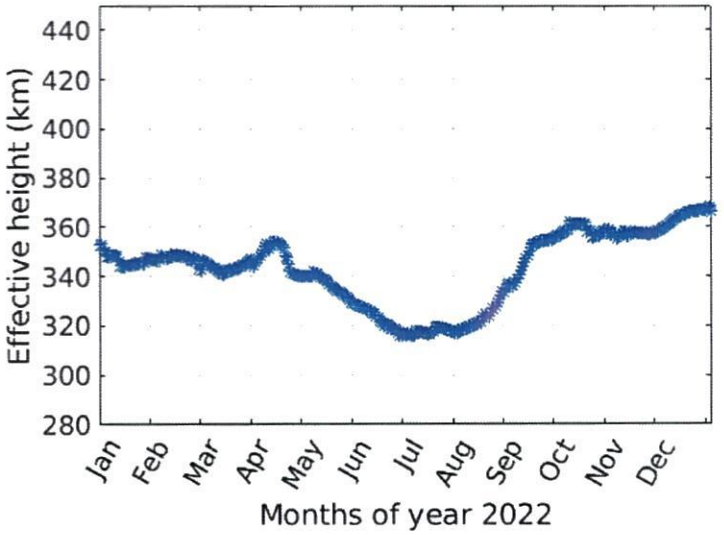
(d) Nov 2023 (e) Dec 2023 (f) Jan 2024

(g) Feb 2024 (h) Mar 2024 (i) Apr 2024

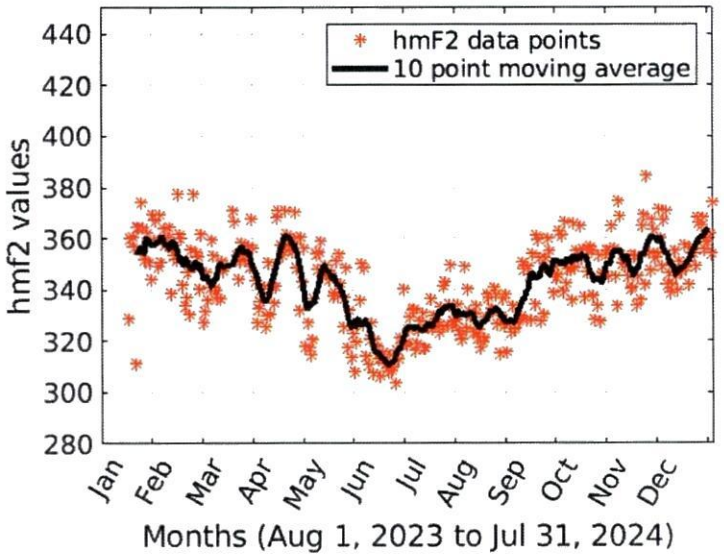
Figure 4.20: Variation of hourly mean of hmF2 with time of the day for the different months.

there is an asymmetry between June and December solstices. In both cases, the values in the December solstice are higher. The highest magnitudes were observed during the September equinox and December solstice, followed by the March equinox, with the lowest during the June solstice. These results are consistent with the findings attained in several studies of TEC in low latitude regions that attributed this kind of pattern to increased ion production during the winter season and an anti-correlation in pre-reversal velocity enhancement between the December and June solstices (Ogwala et al., 2019; Akala et al., 2013).

In addition, using ocoinciding pierce point technique, results from one pair of stations around the crest (RCMN-MAL2) were picked and the values of h for all the quiet days of the year 2014 were grouped into the three seasonal months: January solstice (November, December, January and February), Equinox (March, April, September, October) and June solstice (May, June, July, August). The mean of the daily maximum values of effective height in the respective seasons are represented by the bar graph in Figure 4.22. The daily maximum is observed to be highest at the equinoxes than during the solstice months. Equinox values are higher than solstice values because



(a) h from GNSS-TEC techniques



(b) hmF2 from AIS ionosonde

Figure 4.21: Seasonal variation of effective height with DoY.

during equinox, the sun is overhead the equator and lasts for more hours, making the rate of photoionization at the equator higher compared to the solstice months. This leads to increased height of the ionosphere brought by the enhanced photoionization during equinoctial months compared to solstice months.

Using the value of effective height obtained from all GNSS-TEC techniques, the seasonal variation was investigated using one station around the trough that had all the data for the years of study. In this case ADIS was selected. The mean and standard deviation of the values of effective height of each day were calculated. The coefficient

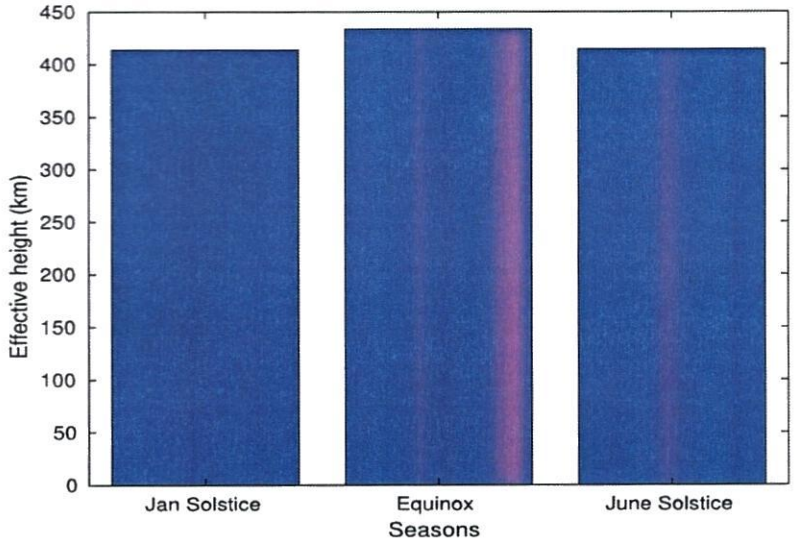


Figure 4.22: Seasonal dependence of effective height of the ionosphere for station pair MAL2-RCMN

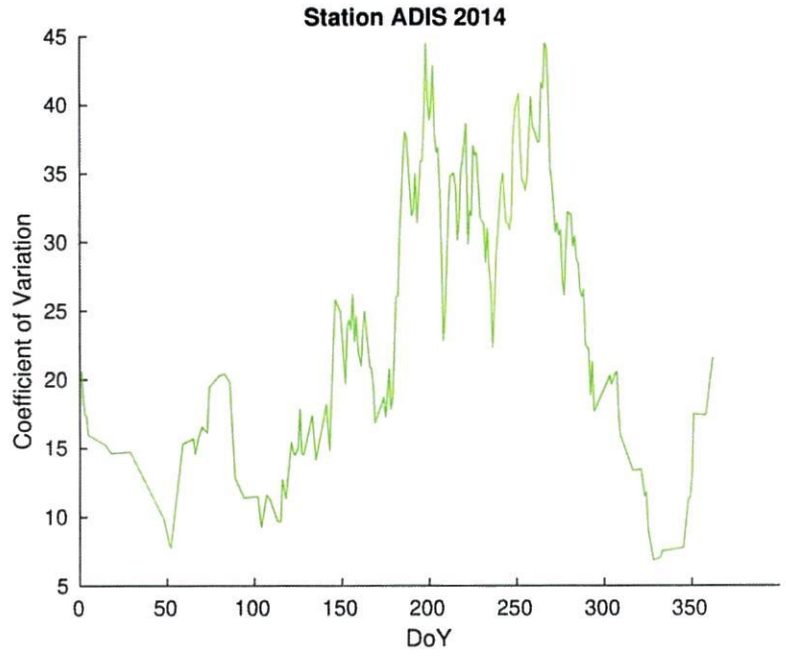


Figure 4.23: Day by day variation of effective height

of variation of the daily values of effective height were determined using the equation,

$$\text{Coefficient of variation} \quad = \left(\frac{\delta_d}{\mu_d} \times 100\right) \% \tag{4.1}$$

where δ_d is the daily standard deviation of of effective height, and μ_d is the daily mean of the effective height. The results of the coefficient of variability are shown in Figure 4.23.

The results indicate that the values of h demonstrate significant variability on a daily basis across all seasons. The least variability is recorded in the months of February and

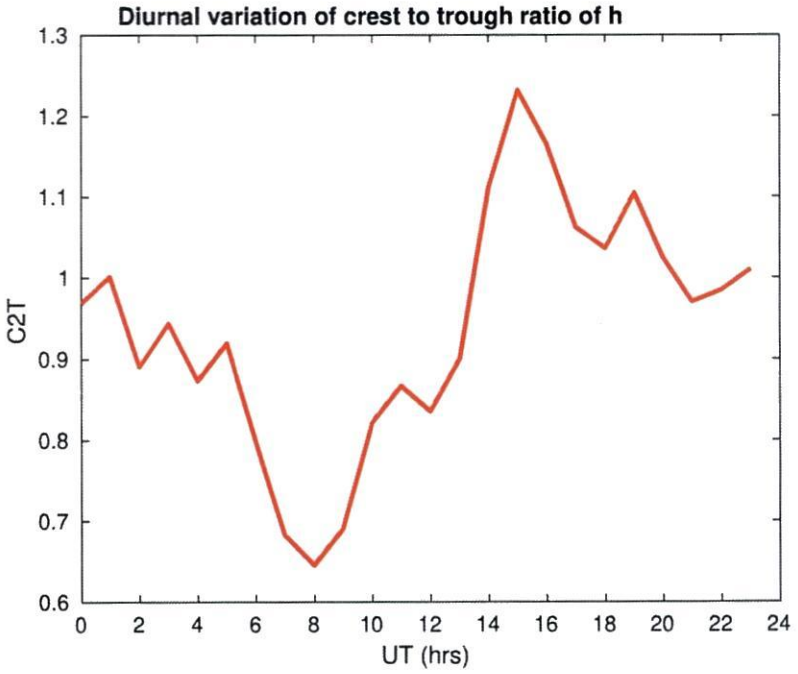


Figure 4.24: Variation of C2T with the time of the day.

December, while the highest coefficient of variation is registered in June and October. This high day to day variability may be attributed to the imbalance between recombination, diffusion and photo ionization as a result of competition between chemistry and the transport responsible for the formation of an electron-density maximum in the F2 layer (McElroy, 2012).

4.3.3 Spatial Variation of Effective Height

To study the spatial variation of effective height, stations were grouped into two: the magnetic equator stations or stations at the trough (ADIS and NAZR) and the crest stations (ARSH,DODM and MTDK). The Crest to Trough ratios (C2T) of h_m were determined. The C2T is determined by dividing the hourly mean of effective height h_m for the stations at the crest, by the hourly mean of h_m for stations at the trough. Figure 4.24, shows the diurnal variation of C2T for all the days of the year 2014. The C2T reduces gradually from a value of 1 at 01: 00 UT to a minimum of about 0.65 at 08:00 UT (Figure 4.24). This implies that the value of h_m recorded at the trough was higher than that at the crest, a typical indication of the day-time ionospheric up welling around the magnetic equator due to $E \times B$ drift (Balan and Bailey, 1995). The ratio then rises steadily, maximizing at around 15:00 UT (18:00 LT) to a value of 1.2 as the sun sets. The increase in the ratio is associated with the downward diffusion of the ions along the magnetic field lines to the anomaly crest regions, increasing the effective height of the ionosphere around the crest. This phenomenon maximizes at sunset (18:00 LT), when the plasma drift is enhanced due to the enhancement of electric field triggered from a sharp day to night E-region conductivity (Tilahun and Mezgebe,

2019; Fejer et al., 2008).

From the different techniques discussed, the effective height of the ionosphere determined for the period from January 2022 to March 2024 was used to model the effective height over the region as discussed in the following section.

4.4 Effective Height Model for East African Region

Measurements of shell height of the ionosphere has been going on for a long period of time, especially to map TEC (Zhao and Zhou, 2019). However, the high cost of infrastructure needed to determine this height has made it very difficult to have adequate coverage of these measurements in the world. The model inputs are discussed in the following subsection.

4.4.1 Model Input Selection

The results obtained in section 4.3 showed that the ionospheric effective height over the East African region is highly variable, and the variation is either periodic (diurnal and seasonal) or random (solar and magnetic dependent). The random variation of effective height is associated with solar and geomagnetic activity (Georgieva et al., 2006), whose level was measured by parameters or indices listed in Section 3.5.

The most appropriate inputs for ANNs model, out of the nine variables listed in section 3.5, were determined by their coefficients from the regression Equation 3.20. The coefficients of the nine variables are presented in Table 4.8.

Table 4.8: Coefficient of the parameters used in regression analysis

Coeff	a_o	a_1	a_2	a_3	a_4	a_5	a_6	a_7	a_8	a_9	a_{10}
Value	280.58	1.80	-41.7	2.88	21.81	3.47	-1.1×10^{-6}	0.0011	0.023	-0.017	0.182

The values of the coefficients of some of the input parameters are so small, implying that their contribution to the variation of effective height is negligible. For example, coefficients represented by a_6, a_7 and a_9 corresponding to proton temperature, solar wind speed and Dst index are very low. These parameters do not significantly influence variation of effective height, and were not considered in the ANN. The variables that were considered are: hours (Hr), day of the year (DoY), sun spot numbers (ssn) and solar flux f10.7 (f10.7). These four parameters became the model input for the artificial neural network model discussed in the subsection that follows.

4.4.2 Artificial Neural Network Model

Out of the four parameters considered, two are periodic and the other two are random. The hours together with the day number of the year that represent the periodic input

were split into cyclical cosine and sine components (Hrc and Hrs for hours and dyc and Dys for days of the year) in order to take into account the adjacency of the last hour of the day and the first hour of the next day (Jasiński, 2022; Sabzehee et al., 2018). The random parameters were used to train the neural network, and establish the variational relationship of effective height using non-linear mathematical modelling, and inter-connectivity between input and output parameter. This was mapped with the aid of different layers and neurons.

To choose a particular architecture used to train data, the most suitable values of the architecture had to be determined as discussed in the following subsection.

4.4.2.1 Optimization of ANN Nodes

Before the actual training of the data, the parameters of the ANNs architecture were optimised to get the most suitable for the data. The data set was first divided into three: training data, validation data and testing data in the ratio of 70%, 25% and 5% respectively. As it is always the case for NN, there is no standard for defining the number of hidden layers or neurons within the network architecture (Habarulema et al., 2011). Depending on the nature of the data, the best number of neurons or hidden layers were arrived at by "trial and error". Several NNs were trained and verified in an effort to find a suitable architecture for the optimum solution. During optimization, a variable number of neurons were set at the first hidden layer and the rmse for both the training data and validation data sets were obtained at the output layer (see Figure 4.25).

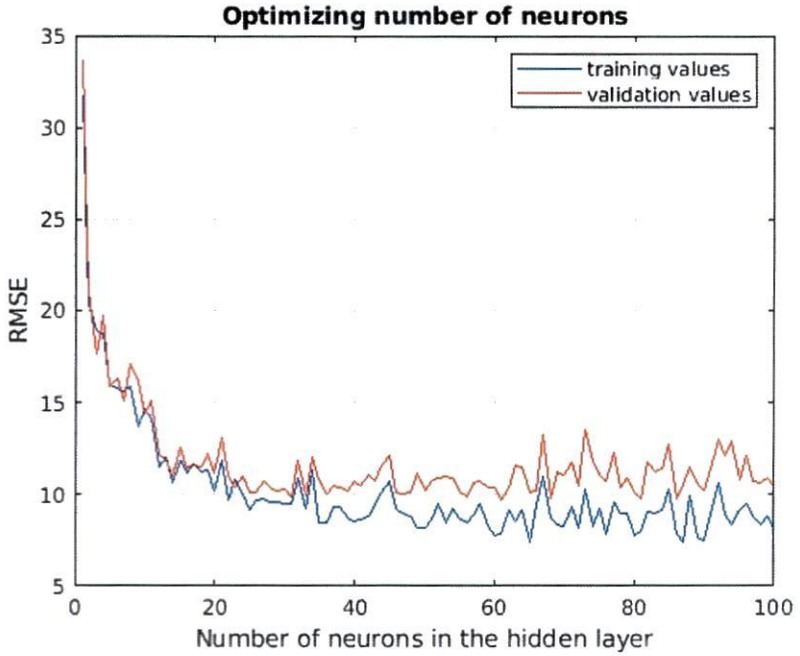


Figure 4.25: rmse between training/validation data set and the respective predicted number of neurons when hidden layers are kept constant

The number of neurons in the first hidden layer that gave the least rmse between training data set and validation data set is about 22 (Figure 4.25). In this case, 22 neurons were used at the first hidden layer to train the data set. Similarly, to find the optimum number of hidden layers, all inputs were fed into the network, and the hidden layers were varied with the number of neurons, giving predictions for the validation data. Statistical analysis using rmse was implemented to determine the suitable architecture, where by the training halts when rmse is minimum to avoid memorisation (Heng et al., 2022). This gave 3 as the optimum number of hidden layers, with the other two each having 5 neurons. Therefore, the final architecture used to train a feedforward neural network were 6 nodes at the input layer, and three hidden layers. The first hidden layer contains 22 neurons, and the subsequent two layers each contain 5 neurons, while the output layer contains only one node of the predicted value of effective height h ($6 \rightarrow 22 \rightarrow 5 \rightarrow 5 \rightarrow 1$) as summarized in Figure 4.26. The

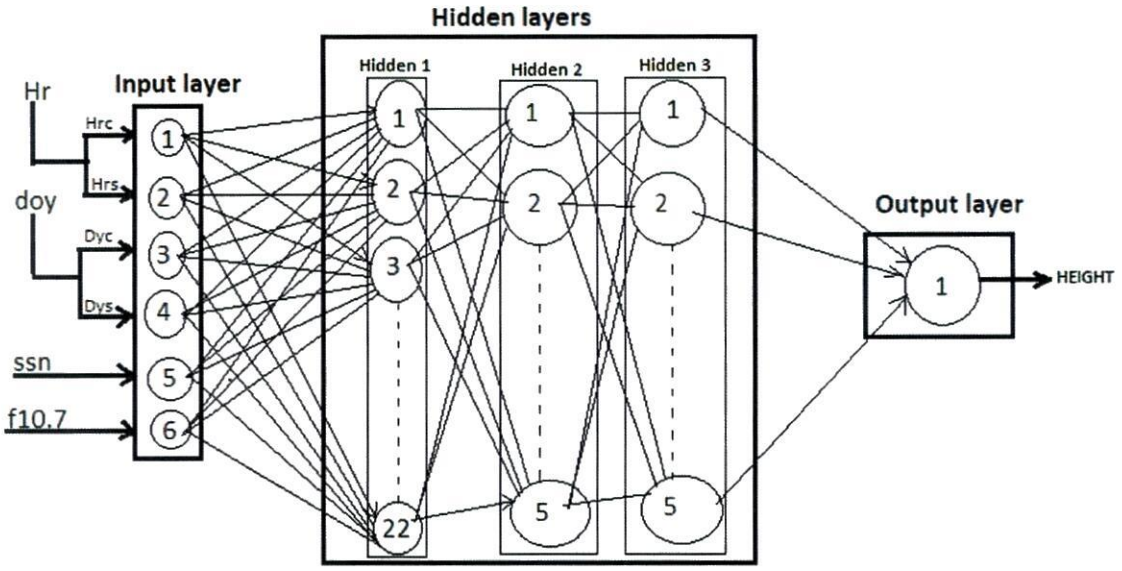


Figure 4.26: An illustration of the final architecture adopted for the neural network model. It has three hidden layers and six input nodes.

measured values of the six inputs were processed through the artificial neural network using the specified architecture, and the predicted values were obtained. The quality of the predicted values were then investigated as discussed in the following subsection.

4.4.3 Validation of the Model

To test the performance of the model, hmF2 recorded at the Malindi ionosonde for the month of April 2024 (since the data used to train the model was up to 31^{st} March 2024) was compared with the model predicted values. Figure 4.27 shows both the hmF2 recorded by the ionosonde and the predicted values over Malindi for days of April 2024 when the station recorded more ionograms. The predicted values of hmF2 mimic the diurnal trend of the ionosonde hmF2 values. The pattern shows two minima, one

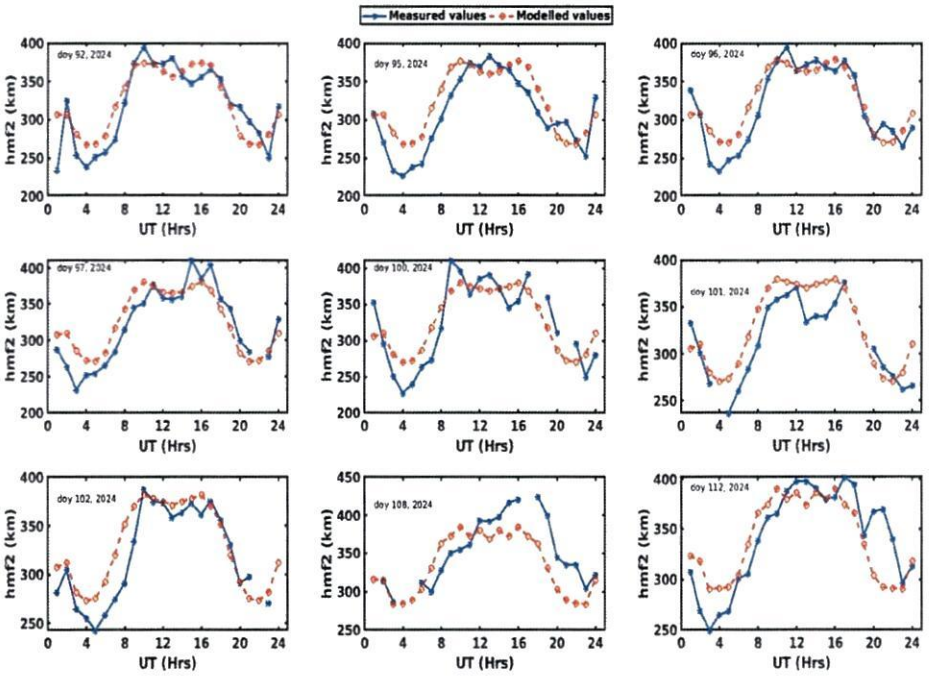


Figure 4.27: Diurnal variation of observed and modeled hmF2 of the AIS ionosonde measurements

around 04:00 UT (dawn) and the other at about 21:00 UT (midnight). The maximum height is experienced between 09:00 UT and 17:00 UT. The model, however, predicts higher values during the morning hours (01:00 UT to 05:00 UT) for all selected days. This occurs because, during this period, there is no sunlight, yet the parameters used to construct the model are solar-dependent. during the day time, the model prediction is in aggrement with the measured values.

4.4.4 Comparison of the ANN model with IRI

The peak heights and electron densities of IRI over the geographic coordinate of Malindi ionosonde (40.19°E, 2.99°S) were downloaded for the month of April 2024. The hmF2 for a given hour provided by IRI were compared with both the ionosonde measured values and the predicted values of the proposed model. The results are shown in Figure 4.28. Both IRI and the proposed model gave consistent predictions before 12:00 UT. IRI predicted higher values of hmF2 compared to the proposed model between 12:00 UT and 20:00 UT. This shows that the proposed model performs better than IRI between 12:00 UT and 20:00 UT for prediction of hmF2. Outside this range, the prediction of the two models are very close to each other. Similarly, the values of rmse for both IRI and the proposed model, shown in Figure 4.29, indicate that the rmse values are minimum between 08:00 UT and 17:00 UT for the predicted values, and instead maximum for IRI in the same time period. The period between 08:00 UT and 17:00 UT, corresponding to the hours when hmF2 is maximum, implying that the

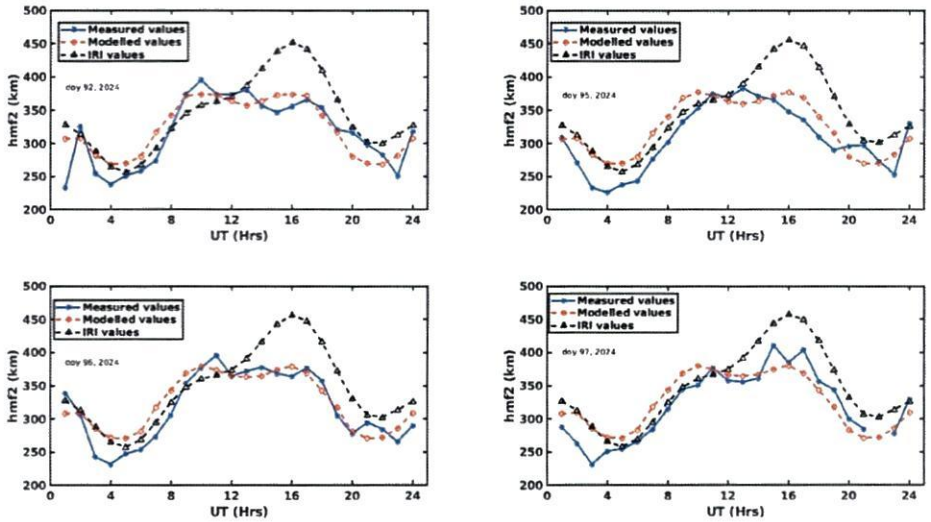


Figure 4.28: Comparison of the diurnal variation between model predicted values of hmF2 and values from both ionosonde and IRI

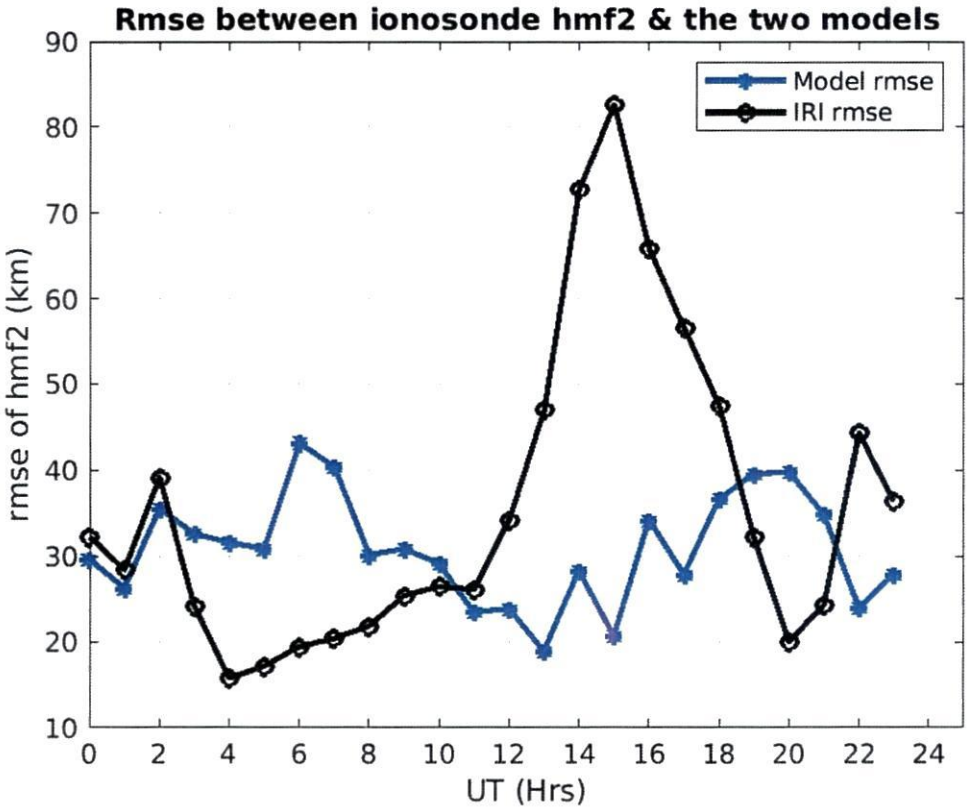


Figure 4.29: Variation of rmse between IRI and predicted values

model prediction is more accurate than the IRI predictions, when hmF2 values are high. This better prediction could be because the model is purely solar dependent.

Chapter 5: Conclusions and Recommendations

5.1 Conclusions

GNSS receivers and two ionosondes in the East African region were used to characterise and model the effective height of the ionosphere over the East African low latitude region. The ionosonde data provided the reference to validate the effective height of the ionosphere.

The effective height falls in a range between 350 km to 500 km, with a modal value of 400 km.

The values of effective height exhibited temporal and spatial variation. The effective height of the ionosphere has a minimum value before sunrise (04:00 UT). It then rises steadily to a maximum between 09:00 UT and 16:00 UT. The value then falls sharply beyond 16:00 UT to another minimum at 21:00 UT. The seasonal variation shows slightly higher values at equinox compared to solstice months. For the spatial variation, ionospheric effective height over the low latitude region of East Africa is higher at the geomagnetic equator during day-time compared to that at the crest of the anomaly region, and vise versa during night.

The model predicted values of the effective height are generally in good agreement with the observed hmf2 from the ionosonde.

5.2 Recommendations

The study found out that the effective height of the ionosphere over the East African region is time dependent and therefore falls in a range. It therefore suggests that the value of 350 km can still be used over the region only for the night time ionosphere. The most appropriate value over East African region is 400 km.

The study also used hmf2 values from a single ionosonde station to develop station specific ionospheric height model. With the number of ionosonde stations begining to increase in the region, there is need to extend this study by considering many more stations to examine the spatial variation over the region.

References

Abdu, M. A. (2016). Electrodynamics of ionospheric weather over low latitudes. *Geoscience Letters*, 3:1–13.

Acharya, R., Roy, B., Sivaraman, M., and Dasgupta, A. (2009). Kalman filter approach for prediction of ionospheric total electron content. In *2009 4th International Conference on Computers and Devices for Communication (CODEC)*, pages 1–4. IEEE.

Adewale, A. O., Oyeyemi, E. O., Adeloye, A. B., Ngwira, C. M., and Athieno, R. (2008). Responses of equatorial F region to different geomagnetic storms observed by GPS in the African sector. *Journal of Geophysical Research*, 116:A12319.

Akala, A., Seemala, G., Doherty, P., Valladares, C., Carrano, C., Espinoza, J., and Oluyo, S. (2013). Comparison of equatorial gps-tec observations over an african station and an american station during the minimum and ascending phases of solar cycle 24. In *Annales Geophysicae*, volume 31, pages 2085–2096. Copernicus Publications Göttingen, Germany.

Anderson, D., Forbes, J., and Codrescu, M. (1989). A fully analytic, low-and middle-latitude ionospheric model. *Journal of Geophysical Research: Space Physics*, 94(A2):1520–1524.

Anderson, D. N., Mendillo, M., and Herniter, B. (1987). A semi-empirical low-latitude ionospheric model. *Radio Science*, 22(2):292–306.

Anthes, R. A., Rocken, C., and Ying-Hwa, K. (2000). Applications of cosmic to meteorology and climate. *Terrestrial Atmospheric and Oceanic Sciences*, 11(1):115–156.

Arikan, F., Shukurov, S., Tuna, H., Arikan, O., and Gulyaeva, T. (2016). Performance of gps slant total electron content and iri-plasma-stec for days with ionospheric disturbance. *Geodesy and Geodynamics*, 7(1):1–10.

Arras, C. (2010). *A global survey of sporadic E layers based on GPS Radio occultations by CHAMP, GRACE and FORMOSAT-3/COSMIC, Deutsches GeoForschungsZentrum GFZ Potsdam.* PhD thesis, Deutsches GeoForschungsZentrum GFZ Potsdam.

Bagiya, M. S., Joshi, H., Iyer, K., Aggarwal, M., Ravindran, S., and Pathan, B. (2009). Tec variations during low solar activity period (2005–2007) near the equatorial ionospheric anomaly crest region in india. In *Annales Geophysicae*, volume 27, pages 1047–1057. Copernicus GmbH.

Balan, N. and Bailey, G. (1995). Equatorial plasma fountain and its effects: Possibility of an additional layer. *Journal of Geophysical Research*, 100:21421–21432.

Banerjee, G. and Mallick, A. K. (1997). A semi empirical model for low latitude hf ionospheric propagation prediction. *IEEE transactions on broadcasting*, 43(1):89–95.

Basheer, I. A. and Hajmeer, M. (2000). Artificial neural networks: fundamentals, computing, design, and application. *Journal of microbiological methods*, 43(1):3–31.

Basu, S., Groves, K., Basu, S., and Sultan, P. (2002). Specification and forecasting of scintillations in communication/navigation links: Current status and future plans. *Journal of atmospheric and solar-terrestrial physics*, 64(16):1745–1754.

Beggan, C. D., Macmillan, S., Hamilton, B., and Thomson, A. W. (2013). Independent validation of swarm level 2 magnetic field products and 'quick look'for level 1b data. *Earth, Planets and Space*, 65:1345–1353.

Bellan, P. M. (2008). *Fundamentals of plasma physics*. Cambridge university press.

Bent, R. B., Llewellyn, S. K., Schmid, P. E., and Llewellyn, M. C. (1972). An improved ionospheric model. *Radio Science*, 7(12):1545–1555.

Beynon, W., PJS, W., et al. (1978). Incoherent scatter of radio waves from the ionosphere.

Bidaine, B. and Warnant, R. (2009). Measuring total electron content with gnss: investigation of two different techniques.

Bilitza, D. (1999). 28. ionospheric models for radio propagation studies. *Review of radio science*, 2002:625–679.

Bilitza, D., Altadill, D., Truhlik, V., Shubin, V., Galkin, I., Reinisch, B., and Huang, X. (2017). International reference ionosphere 2016: From ionospheric climate to real-time weather predictions. *Space weather*, 15(2):418–429.

Bilitza, D., McKinnell, L.-A., Reinisch, B., and Fuller-Rowell, T. (2011). The international reference ionosphere today and in the future. *Journal of Geodesy*, 85:909–920.

Bilitza, D., Rawer, K., and Pallaschke, S. (1988). Study of ionospheric models for satellite orbit determination. *Radio Science*, 23:223–232.

Bilitza, D., Reinisch, B., and McKinnell, L. (2010). International reference ionosphere 2010. In *AGU Fall Meeting Abstracts*, volume 2010, pages SA11B–1580.

Bilitza, D. and Tamara, G. (2012). Towards iso standard earth ionosphere and plasmasphere model. *39th COSPAR Scientific Assembly*, 39:192.

Birch, M. J., Hargreaves, J. K., and Bailey, G. J. (2002). On the use of an effective ionospheric height in electron content measurement by GPS reception. *RADIO SCIENCE*, 37(11015).

Bremer, J. (1998). Trends in the ionospheric E and F regions over europe. In *Annales Geophysicae*, volume 16, pages 986–996. Springer Verlag Göttingen, Germany.

Brownlee, J. (2018). How to configure the number of layers and nodes in a neural network. *Machine Learning Mastery: Vermont, Australia*.

Brunini, C., Camilion, E., and Azpilicueta, F. (2011). Simulation study of the influence of the ionospheric layer height in the thin layer ionospheric model. *Journal of Geodesy*, 85:1432–1394.

Bruno, J. (2021). *Ionospheric tomography and data assimilation*. PhD thesis, University of Bath.

Buchert, S., Zangerl, F., Sust, M., André, M., Eriksson, A., Wahlund, J.-E., and Opgenoorth, H. (2015). Swarm observations of equatorial electron densities and topside gps track losses. *Geophysical Research Letters*, 42(7):2088–2092.

Chen, C.-H., Liu, J.-Y., Yumoto, K., Lin, C.-H., and Fang, T.-W. (2008). Equatorial ionization anomaly of the total electron content and equatorial electrojet of ground-based geomagnetic field strength. *Journal of Atmospheric and Solar-Terrestrial Physics*, 70(17):2172–2183.

Chen, F. F. (1984). *Introduction to Plasma Physics and Controlled Fusion*. Springer link, Electrical EngineeringUniversity of California at Los AngelesLos AngelesUSA.

Chen, J. and Liu, Y. (2022). Neural optimization machine: A neural network approach for optimization. *arXiv preprint arXiv:2208.03897*.

Chen, J., Wang, W., and Lei, J. (2021). Longitudinal variations of equatorial ionospheric electric fields near sunrise. *Journal of Geophysical Research: Space Physics*, 126(5):e2020JA028977.

Chen, P., Liu, H., Ma, Y., and Zheng, N. (2020). Accuracy and consistency of different global ionospheric maps released by IGS ionosphere associate analysis centers. *Advances in Space Research*, 65(1):163–174.

Chen, Z., Wang, S., Zhang, S., Fang, G., and Wang, J. (2013). Automatic scaling of F layer from ionograms. *Radio science*, 48(3):334–343.

Cheng, P.-H., Lin, C., Otsuka, Y., Liu, H., Rajesh, P. K., Chen, C.-H., Lin, J.-T., and Chang, M. (2021). Statistical study of medium-scale traveling ionospheric disturbances in low-latitude ionosphere using an automatic algorithm. *Earth, Planets and Space*, 73(1):105.

Cherniak, I. V., Zakharenkova, I., Dzubanov, D., and Krankowski, A. (2014). Analysis of the ionosphere/plasmasphere electron content variability during strong geomagnetic storm. *Advances in Space Research*, 54(4):586–594.

Chernigovskaya, M., Shpynev, B., Yasyukevich, A., Khabituev, D., Ratovsky, K., Belinskaya, A. Y., Stepanov, A., Bychkov, V., Grigorieva, S., Panchenko, V., et al. (2021). Longitudinal variations of geomagnetic and ionospheric parameters in the northern hemisphere during magnetic storms according to multi-instrument observations. *Advances in Space Research*, 67(2):762–776.

Chuo, Y.-J. and Lei, J. (2014). Variations of scale height at f-region peak based on ionosonde measurements during solar maximum over the crest of equatorial ionization anomaly region. *The Scientific World Journal*, 9.

Ciraolo, L. and Spalla, P. (1997). Comparison of ionospheric total electron content from the navy navigation satellite system and the GPS. *Radio science*, 32:1071–1080.

Coco, D. S., C.Coker, S.R.Dahlke, and Clynch, J. (1991). Variability of GPS satellite differential group delay biases. *IEEE Transactions on Aerospace and Electronic Systems*, 27(6):931–938.

Codrescu, M., Fuller-Rowell, T., and Minter, C. (2004). An ensemble-type kalman filter for neutral thermospheric composition during geomagnetic storms. *Space Weather*, 2(11).

Consortium, S. L. . P. S. et al. (2013). Product specification for L2 products and auxiliary products. *Doc. no: SW-DS-DTU-GS-0001*.

Daniell, R. E. and Brown, L. D. (1995). *PRISM: a Parameterized Real-time Ionospheric Specification Model: Version 1.5*. Phillips Laboratory, Directorate of Geophysics, Air Force Materiel Command.

Danilov, A. (2002). Overview of the trends in the ionospheric e and f2 regions. *Physics and Chemistry of the Earth, Parts A/B/C*, 27(6-8):579–588.

DasGupta, A., Paul, A., and Das, A. (2007). *Ionospheric total electron content (TEC) studies with GPS in the equatorial region*. CSIR.

Davies, K. (1989). *Ionospheric Radio*. Short Run Press, ISBN 0 86341 186 X, United Kingdom.

Davies, K. (1990a). *Ionospheric radio*. Number 31. Iet.

Davies, K. (1990b). *Ionospheric radio*. Peter Peregrinus, London.

Doherty, P. H., Delay, S. H., Valladares, C. E., and Klobuchar, J. A. (2003). Ionospheric scintillation effects on gps in the equatorial and auroral regions. *Navigation*, 50(4):235–245.

dos Santos Prol, F. and de Oliveira Camargo, P. (2015). Review of tomographic reconstruction methods of the ionosphere using gnss. *Brazilian Journal of Geophysics*, 33(3):445–459.

Doshi, S. (2019). Various optimization algorithms for training neural network. *Towards data science*, 13.

D'ujanga, F., Baki, P., Olwendo, J., and Twinamasiko, B. (2013). Total electron content of the ionosphere at two stations in East Africa during the 24-25 October 2011 geomagnetic storm. *Advances in Space Research*, 51:712–721.

Drob, D. P., Emmert, J. T., Meriwether, J. W., Makela, J. J., Doornbos, E., Conde, M., Hernandez, G., Noto, J., Zawdie, K. A., McDonald, S. E., et al. (2015). An update to the horizontal wind model (hwm): The quiet time thermosphere. *Earth and Space Science*, 2(7):301–319.

Dugassa, T., Habarulema, J. B., and Nigussie, M. (2020). Equatorial and low-latitude ionospheric TEC response to CIR-driven geomagnetic storms at different longitude sectors. *Advances in Space Research*, 66(8):1947–1966.

Elliot, J. L. (1979). Stellar occultation studies of the solar system. *Annual review of Astronomy and Astrophysics*, 17(1):445–475.

Emmert, J., Richmond, A., and Drob, D. (2010). A computationally compact representation of magnetic-apex and quasi-dipole coordinates with smooth base vectors. *Journal of Geophysical Research: Space Physics*, 115(A8).

Emmert, J. T., Drob, D. P., Picone, J. M., Siskind, D. E., Jones Jr, M., Mlynczak, M., Bernath, P. F., Chu, X., Doornbos, E., Funke, B., et al. (2021). Nrlmsis 2.0: A whole-atmosphere empirical model of temperature and neutral species densities. *Earth and Space Science*, 8(3):e2020EA001321.

Fan, M., Zhu, K., De Santis, A., Marchetti, D., Cianchini, G., Piscini, A., He, X., Wen, J., Wang, T., Zhang, Y., et al. (2022). Analysis of swarm satellite magnetic field data for the 2015 mw 7.8 nepal earthquake based on nonnegative tensor decomposition. *IEEE Transactions on Geoscience and Remote Sensing*, 60:1–19.

Fejer, B., Jensen, J., and Su, S.-Y. (2008). Quiet time equatorial f region vertical plasma drift model derived from ROCSAT-1 observations. *journal of geophysical research*, 113.

Feltens, J., Angling, M., Jackson-Booth, N., Jakowski, N., Hoque, M., Hernández-Pajares, M., Aragón-Àngel, A., Orús, R., and Zandbergen, R. (2011). Comparative testing of four ionospheric models driven with gps measurements. *Radio Science*, 46(06):1–11.

Filby and D, S. (1997). A validation of the parameterized real-time ionosopheric specification Model(PRISM) version 1. 7 b. Master's thesis, Air Force Institute of Technology.

Forbes, J. M., Palo, S. E., and Zhang, X. (2000). Variability of the ionosphere. *Journal of Atmospheric and Solar-Terrestrial Physics*, 62(8):685–693.

Friis-Christensen, E., Lühr, H., and Hulot, G. (2006). Swarm: A constellation to study the earth's magnetic field. *Earth, planets and space*, 58:351–358.

Fritts, D., Vadas, S., Riggin, D., Abdu, M., Batista, I., Takahashi, H., Medeiros, A., Kamalabadi, F., Liu, H.-L., Fejer, B., et al. (2008). Gravity wave and tidal influences on equatorial spread f based on observations during the spread f experiment (spreadfex). In *Annales Geophysicae*, volume 26, pages 3235–3252. Copernicus GmbH.

Froń, A., Galkin, I., Krankowski, A., Bilitza, D., Hernández-Pajares, M., Reinisch, B., Li, Z., Kotulak, K., Zakharenkova, I., Cherniak, I., et al. (2020). Towards cooperative global mapping of the ionosphere: Fusion feasibility for IGS and IRI with global climate VTEC maps. *Remote Sensing*, 12(21):3531.

Fuller-Rowell, T. J. and Rees, D. (1980). A three-dimensional time-dependent global model of the thermosphere. *Journal of the Atmospheric Sciences*, 37(11):2545–2567.

Ganguly, S. and Brown, A. (2001). Real-time characterization of the ionosphere using diverse data and models. *Radio Science*, 36(5):1181–1197.

Gao, Y. and Liu, Z. (2002). Precise ionosphere modeling using regional gpsnetwork data. *Positioning*, 01:7.

Garner, T., Gaussiran Ii, T., Tolman, B., Harris, R., Calfas, R., and Gallagher, H. (2008). Total electron content measurements in ionospheric physics. *Advances in Space Research*, 42(4):720–726.

Georgieva, K., Kirov, B., and Gavruseva, E. (2006). Geoeffectiveness of different solar drivers, and long-term variations of the correlation between sunspot and geomagnetic activity. *Physics and Chemistry of the Earth, Parts A/B/C*, 31(1-3):81–87.

G.L.Goodwin (1992). Total electron content and ionospheric slab thickness measurements using GPS satellites. *Proc. South Pacific Solar-Terrestrial Physics Workshop. Tenth National Congress of the Australian Institute of Physics. Univ. of Melbourne, Melbourne, Australia.*

Goodman, J. M. (2005). *Space Weather and Telecommunications*. Springer Science and Business Media.

Griffiths, H. (2018). Oliver heaviside and the heaviside layer. *Philosophical Transactions of the Royal Society A: Mathematical, Physical and Engineering Sciences*, 376(2134):20170459.

Gulyaeva, T. and Bilitza, D. (2012). Towards ISO standard Earth ionosphere and plasmasphere model. *New developments in the standard model*, pages 1–39.

Gulyaeva, T., Nava, B., and Stanislawska, I. (2021). Modeling center-of-mass of the ionosphere from the slab-thickness. *Radio Science*, 56(4):1–17.

Guo, J.-P., Zhang, D., Hao, Y., and Xiao, Z. (2014). Simulation study of effective ionospheric shell height based on global core plasma model. *Chinese Journal of Geophysics (Acta Geophysica Sinica)*, 57:3577–3585.

Habarulema, J. B. (2010). *A contribution to TEC modelling over Southern Africa using GPS data*. PhD thesis, Rhodes University.

Habarulema, J. B., McKinnell, L.-A., Burešovà, D., Zhang, Y., Seemala, G., Ngwira, C., Chum, J., and Opperman, B. (2013). A comparative study of TEC response for the African equatorial and mid-latitudes during storm conditions. *Journal of Atmospheric and Solar-Terrestrial Physics*, 102:105–114.

Habarulema, J. B., McKinnell, L.-A., and Opperman, B. D. (2011). Regional GPS TEC modeling; attempted spatial and temporal extrapolation of TEC using neural networks. *Journal of geophysical research: space physics*, 116(A4).

Hardy, D. A., Gussenhoven, M., Raistrick, R., and McNeil, W. (1987). Statistical and functional representations of the pattern of auroral energy flux, number flux, and conductivity. *Journal of Geophysical Research: Space Physics*, 92(A11):12275–12294.

Hasan, H., Aljuneidi, A., and Alfrehat, A. (2020). Estimation of tec total electron content in the ionosphere using the klobuchar model of a single-frequency gps receiver over the city of damascus.

Hawk, M. (2001). Mid-Latitude Sporadic-E - A Review.

Haykin, S. (1998). *Neural networks: a comprehensive foundation*. Prentice Hall PTR.

Hedin, A. E. (1987). MSIS-86 thermospheric model. *Journal of Geophysical Research: Space Physics*, 92(A5):4649–4662.

Hedin, A. E. (1991). Extension of the msis thermosphere model into the middle and lower atmosphere. *Journal of Geophysical Research: Space Physics*, 96(A2):1159–1172.

Hegarty, C. J. (2012). Gnss signals—an overview. In *2012 IEEE International Frequency Control Symposium Proceedings*, pages 1–7. IEEE.

Hein, W., Goto, Y., and Kasahara, Y. (2016). Estimation method of ionospheric tec distribution using single frequency measurements of GPS signals. *International Journal of Advanced Computer Science and Applications*, 7.

Heng, S. Y., Ridwan, W. M., Kumar, P., Ahmed, A. N., Fai, C. M., Birima, A. H., and El-Shafie, A. (2022). Artificial neural network model with different backpropagation algorithms and meteorological data for solar radiation prediction. *Scientific reports*, 12(1):10457.

Henry, R. and Owen, G. (1969). *Introduction to ionospheric physics*, volume 14 of *International geophysics series*. New York, Academic Press.

Heppner, J. and Maynard, N. (1987). Empirical high-latitude electric field models. *Journal of Geophysical Research: Space Physics*, 92(A5):4467–4489.

Hernandez-Pajares, M., Juan, J. M., Sanz, J., Orus, R., Garcia-Rigo, A., Feltens, J., Komjathy, A., Schaer, S. C., and Krankowski, A. (2009). The IGS VTEC maps: a reliable source of ionospheric information since 1998. *J. Geod.*, 83:263–275.

Hernández-Pajares, M., Roma-Dollase, D., Krankowski, A., García-Rigo, A., and Orús-Pérez, R. (2017). Methodology and consistency of slant and vertical assessments for ionospheric electron content models. *Journal of Geodesy*, 91(12):1405–1414.

Ho, A., Datta, I. A. M., and Shumlak, U. (2018). Physics-based-adaptive plasma model for high-fidelity numerical simulations. *Frontiers in Physics*, 6:105.

Hobiger, T. and Jakowski, N. (2017). Atmospheric signal propagation. *Springer handbook of global navigation satellite systems*, pages 165–193.

Hochegger, G., Nava, B., Radicella, S., and Leitinger, R. (2000). A family of ionospheric models for different uses. *Physics and Chemistry of the Earth, Part C: Solar, Terrestrial & Planetary Science*, 25(4):307–310.

Hoque, M. M. and Jakowski, N. (2008). Estimate of higher order ionospheric errors in gnss positioning. *Radio Science*, 43(05):1–15.

Hoque, M. M., Jakowski, N., and Prol, F. S. (2022). A new climatological electron density model for supporting space weather services. *Journal of Space Weather and Space Climate*, 12:1.

Houminer, Z. and Soicher, H. (1996). Improved short-term predictions of f0f2 using gps time delay measurements. *Radio science*, 31:1099–1108.

Hu, L., Ning, B., Liu, L., Zhao, B., Li, G., Wu, B., Huang, Z., Hao, X., Chang, S., and Wu, Z. (2014). Validation of COSMIC ionospheric peak parameters by the measurements of an ionosonde chain in china. In *Annales Geophysicae*, volume 32, pages 1311–1319. Copernicus GmbH.

Huang, W. Q., Xiao, Z., Xiao, S. G., H., D., Hao, Y. Q., and Suo, Y. C. (2011). Case study of apparent longitudinal differences of spread F occurrence for two midlatitude stations. *Radio Science*, 46.

Huang, Z. and Yuan, H. (2013). Analysis and improvement of ionospheric thin shell model used in sbas for china region. *Advances in Space Research*, 51:2035–2042.

Huba, J. and Joyce, G. (2010). Global modeling of equatorial plasma bubbles. *Geophysical Research Letters*, 37(17).

Huba, J., Joyce, G., and Fedder, J. (2000). Sami2 is another model of the ionosphere (sami2): A new low-latitude ionosphere model. *Journal of Geophysical Research: Space Physics*, 105(A10):23035–23053.

Huba, J., Joyce, G., and Krall, J. (2008). Three-dimensional equatorial spread F modeling. *Geophysical Research Letters*, 35(10).

Hunsucker, R. D. and Hargreaves, J. K. (2003). *The high-latitude ionosphere and its effects on radio propagation*. New York, Cambridge University Press.

Hwang, C., Tseng, T.-P., Lin, T., Švehla, D., and Schreiner, B. (2009). Precise orbit determination for the FORMOSAT-3/COSMIC satellite mission using GPS. *Journal of Geodesy*, 83:477–489.

Hysell, D. (2020). From instability to irregularities. In *The Dynamical Ionosphere*, pages 137–167. Elsevier.

Jakowski, N. and Jungstand, A. (1994). Modelling the regional ionosphere by using GPS observations. In *Internat. Beacon Satellite Symposium, University of Wales, Aberystwyth, UK, 11. - 15. Juli 1994*. LIDO-Berichtsjahr=1994, note=RIM,.

Jasiński, T. (2022). A new approach to modeling cycles with summer and winter demand peaks as input variables for deep neural networks. *Renewable and Sustainable Energy Reviews*, 159:112217.

Jiang, C., Wang, W., Yang, G., and Zhao, Z. (2023). A numerical study of noontime bite-outs in F2-region electron density. *Advances in Space Research*, 71(3):1818–1826.

Jiang, H., Zemin, W., Jiachun, A., Jingbin, L., Ningbo, W., and Hang, L. (2018). Influence of spatial gradients on ionospheric mapping using thin layer models. *GPS Solutions*, 22.

Juan, B., Todd, W., and Per, E. (2004). New ionospheric estimation algorithm for SBAS combining kriging and tomography. *Proceedings of the 2004 National Technical Meeting of The Institute of Navigation, San Diego, CA*, pages 524–529.

Kayode, Y. O., Okoh, D., Onori, E., Ometan, O., Ogwala, A., Somoye, E., and Adeniji-Adele, R. (2023). Total electron content variations at a low latitude East African station and its comparison with IRI-2016, iri-plas2017 and NeQuick-2 models during solar cycle 24.

Kelley, M. C. (2009). *The Earth's ionosphere: Plasma Physics and Electrodynamics*. Amsterdam, academic Press, second edition.

Kersley, L., Malan, D., Pryse, S. E., Cander, L. R., Bamford, R. A., Belehaki, A., Leitinger, R., Radicella, S. M., Mitchell, C. N., and Spencer, P. S. (2004). Total electron content-a key parameter in propagation: measurement and use in ionospheric imaging. *Ann. Geophysics*, 47:1067–1091.

Khadka, S. M., Valladares, C. E., Sheehan, R., and Gerrard, A. J. (2018). Effects of electric field and neutral wind on the asymmetry of equatorial ionization anomaly. *Radio Science*, 53(5):683–697.

Kimura, N., Yoshinaga, I., Sekijima, K., Azechi, I., and Baba, D. (2019). Convolutional neural network coupled with a transfer-learning approach for time-series flood predictions. *Water*, 12(1):96.

Klobuchar, J. A. (1987a). Ionospheric corrections for GPS systems. *IEEE Transactions on Aerospace and Electronic Systems*, AES-23(3):325–331.

Klobuchar, J. A. (1987b). Ionospheric time-delay algorithm for single-frequency GPS users. *IEEE Transactions on Aerospace and Electronic Systems*, AES-23(3):325–331.

Knudsen, D., Burchill, J., Buchert, S., Eriksson, A., Gill, R., Wahlund, J.-E., Åhlén, L., Smith, M., and Moffat, B. (2017). Thermal ion imagers and langmuir probes in the swarm electric field instruments. *Journal of Geophysical Research: Space Physics*, 122(2):2655–2673.

Komjathy, A. (1997). *Global Ionospheric Total Electron Content Mapping Using the Global Positioning System*. PhD thesis, University of New Brunswick,.

Komjathy, A., Galvan, D. A., Stephens, P., Butala, M. D., Akopian, V., Wilson, B., Verkhoglyadova, O., Mannucci, A. J., and Hickey, M. (2012). Detecting ionospheric TEC perturbations caused by natural hazards using a global network of GPS receivers: The tohoku case study. *Earth Planets Space*, 64:1287–1294.

Kosary, M., Forootan, E., Farzaneh, S., and Schumacher, M. (2022). A sequential calibration approach based on the ensemble kalman filter (C-EnKF) for forecasting total electron content (TEC). *Journal of Geodesy*, 96(4):29.

Kotov, D., Richards, P. G., Truhlík, V., Bogomaz, O., Shulha, M., Maruyama, N., Hairston, M., Miyoshi, Y., Kasahara, Y., Kumamoto, A., et al. (2018). Coincident observations by the kharkiv is radar and ionosonde, dmsp and arase (erg) satellites, and flip model simulations: Implications for the nrlmsise-00 hydrogen density, plasmasphere, and ionosphere. *Geophysical Research Letters*, 45(16):8062–8071.

Krankowskia, A., I.Shagimuratovb, I.Ephishovb, A.Krypiak-Gregorczyka, and G.Yakimovab (2009). The occurrence of the mid-latitude ionospheric trough in GPS-TEC measurements. *Advances in space research*, 43(11):1721–1731.

Krishnan, S. (2022). How to determine the number of layers and neurons in the hidden layer. *URL: https://medium. com/geekculture/introduction-to-neuralnetwork-2f8b8221fbd3.*

Kumar, Y., Kaul, S., and Sood, K. (2019). Effective use of the machine learning approaches on different clouds. In *Proceedings of International Conference on Sustainable Computing in Science, Technology and Management (SUSCOM), Amity University Rajasthan, Jaipur-India.*

Langley, R., Fedrizzi, M., de Paula, E., Santos, M., and Komjathy, A. (2002). Mapping the low latitude ionosphere with GPS. *GPS World*, 13:41–46.

Langley, R. B. (2000). GPS, the ionosphere and the solar maximum. *GPS world.*

Lanyi.G (1986). Total ionospheric electron content calibration using series gps satellite data. *In its The Telecommunications and Data Acquisition Report 12 p*, (19-32):1–12.

Li, H.-W., Hao, S., Ni, Y.-Q., Wang, Y.-W., and Xu, Z.-D. (2024). Hybrid structural analysis integrating physical model and continuous-time state-space neural network model. *Computer-Aided Civil and Infrastructure Engineering.*

Li, M., Yuan, Y., Zhang, B., Wang, N., Zishen, Liu, X., and Zhang, X. (2017). Determination of the optimized single-layer ionospheric height for electron content measurements over china. *J Geod.*

Liu, L., Wan, W., Ning, B., Pirog, O. M., and Kurkin, V. I. (2006). Solar activity variations of the ionospheric peak electron density. *J. Geophys. Res.*, 111:A08304.

Liu, Q., Hernández-Pajares, M., Yang, H., Monte-Moreno, E., Roma-Dollase, D., García-Rigo, A., Li, Z., Wang, N., Laurichesse, D., Blot, A., et al. (2021). The cooperative IGS RT-GIMs: A reliable estimation of the global ionospheric electron content distribution in real time. *Earth System Science Data*, 13(9):4567–4582.

Ma, G. and Maruyama, T. (2003). Derivation of TEC and estimation of instrumental biases from GEONET in japan. *Annales Geophysicae*, 21(10):2083–2093.

MacDougall, J., Abdu, M., Batista, I., Fagundes, P., Sahai, Y., and Jayachandran, P. (2009). On the production of traveling ionospheric disturbances by atmospheric gravity waves. *Journal of Atmospheric and Solar-Terrestrial Physics*, 71:2013–2016.

MacQueen, R. M., Csoeke-Poeckh, A., Hildner, E., House, L., Reynolds, R., Stanger, A., Tepoel, H., and Wagner, W. (1980). The high altitude observatory coronagraph/polarimeter on the solar maximum mission. *Solar Physics*, 65:91–107.

Madonia, P., Bonaccorso, A., Bonforte, A., Buonocunto, C., Cannata, A., Carleo, L., Cesaroni, C., Currenti, G., De Gregorio, S., Di Lieto, B., et al. (2022). Propagation of perturbations in the lower and upper atmosphere over the central mediterranean, driven by the 15 january 2022 hunga tonga-hunga ha'apai volcano explosion. *Atmosphere*, 14(1):65.

Malik, R., Sarkar, S., Mukherjee, S., and Gwal, A. (2010). Study of ionospheric variability during geomagnetic storms. *Journal of Indian Geophysical union*, 14(1):47–56.

Mallika, L., Ratnam, D. V., Raman, S., Sivavaraprasad, G., et al. (2020). Machine learning algorithm to forecast ionospheric time delays using global navigation satellite system observations. *Acta Astronautica*, 173:221–231.

Mannucci, A. J., Ao, C. O., and Williamson, W. (2020). GNSS radio occultation. *Position, Navigation, and Timing Technologies in the 21st Century: Integrated Satellite Navigation, Sensor Systems, and Civil Applications*, 1:971–1013.

Mannucci, A. J., Wilson, B. D., Yuan, D. N., Ho, C. H., Lindqwister, U. J., and Runge, T. F. (1998). A global mapping technique for GPS-derived ionospheric total electron content measurements. *Radio Science*, 33(3):565–582.

Mas, J. F. and Flores, J. J. (2008). The application of artificial neural networks to the analysis of remotely sensed data. *International Journal of Remote Sensing*, 29(3):617–663.

McDonald, S. E., Coker, C., Dymond, K. F., Anderson, D. N., and Araujo-Pradere, E. A. (2011). A study of the strong linear relationship between the equatorial ionization anomaly and the prereversal EXB drift velocity at solar minimum. *Radio Science*, 46(06):1–9.

McElroy, M. B. (2012). ionosphere and magnetosphere. Technical report, Encyclopedia Britannica.

McKinnell, L.-A., Opperman, B., and Cilliers, P. J. (2007). GPS and Ionosonde TEC over Grahamstown, South Africa: first comparisons. *Advances in Space Research*, 39:816–820.

McNamara, L. F. (1991). *The ionosphere: communications, surveillance, and direction finding.* Malabar, FL, Krieger.

Meggs, R. W., Mitchell, C. N., Watson, R. J., and Dear, R. M. (2006). Real-time imaging of the ionosphere over the united kingdom – preliminary results. *Meeting Proceedings RTO-MP-IST-056.*

Memarzadeh, Y. (2009). *Ionospheric modeling for precise GNSS applications.* PhD thesis, Delft University of Technology.

Millward, G. H., Rishbeth, H., Fuller-Rowell, T. J., Aylward, A. D., Quegan, S., and Moffett, R. J. (1996). Ionospheric F2 layer seasonal and semiannual variations. *Journal of Geophysical research*, 101:5149–5156.

Mochalov, V. and Mochalova, A. (2019). Extraction of ionosphere parameters in ionograms using deep learning. In *E3S Web of Conferences*, volume 127, page 01004. EDP Sciences.

Moeketsi, D., Combrink, A., S, N., and Combrinck, L. (2005). Ionospheric total electron content (TEC) observed using the southern african gps network. *South African Journal of Science*, 101:537–539.

Moldwin, M. (2008). *An Introduction to Space Weather.* Cambridge, Cambridge University Press.

Moore, M., Watson, C., King, M., McClusky, S., and Tregoning, P. (2014). Empirical modelling of site-specific errors in continuous GPS data. *Journal of Geodesy*, 88:887–900.

M.Stankov, S., Stegen, K., Muhtarov, P., and Warnanta, R. (2010). Local ionospheric electron density profile reconstruction in real time from simultaneous ground-based GNSS and ionosonde measurements. *Advances in space research*, 47:1172–1180.

Muslim, B., Juni, K. C., et al. (2019). Harmonic analysis of ionospheric Total Electron Content (TEC) using kalman filter. In *Journal of Physics: Conference Series*, volume 1373, page 012015. IOP Publishing.

Nava, B., S.M.Radicella, R.Leitinger, and P.Coïssona (2007). Use of total electron content data to analyze ionosphere electron density gradients. *Advances in space research*, pages 1292–1297.

Ngayap, U., Paparini, C., Porretta, M., Buist, P., Jacobsen, K. S., Dähnn, M., Hanna, N., Halilovic, D., Świątek, A., and Gajdowska, P. (2023). Comparison of nequick g and klobuchar model performances at single-frequency user level. *Engineering Proceedings*, 54(1):7.

Norsuzila, Y., Abdullah, M., and Ismail, M. (2008). Leveling Process of Total Electron Content (TEC) Using Malaysian Global Positioning System (GPS) Data. *American Journal of Engineering and Applied Sciences*, 1(3):223–229.

Ogwala, A., Onori, E., Kayode, Y., Adele, R. A., and Somoye, E. (2022). The equatorial ionospheric phenomena: A review of past studies, government interest and unsolved problems. *Latin-American Journal of Physics Education*, 16(2):3.

Ogwala, A., Somoye, E. O., Ogunmodimu, O., Adeniji-Adele, R. A., Onori, E. O., and Oyedokun, O. (2019). Diurnal, seasonal and solar cycle variation in total electron content and comparison with iri-2016 model at birnin kebbi. In *Annales Geophysicae*, volume 37, pages 775–789. Copernicus Publications Göttingen, Germany.

Olsen, N., Friis-Christensen, E., Floberghagen, R., Alken, P., Beggan, C. D., Chulliat, A., Doornbos, E., Da Encarnação, J. T., Hamilton, B., Hulot, G., et al. (2013). The swarm satellite constellation application and research facility (SCARF) and swarm data products. *Earth, Planets and Space*, 65:1189–1200.

Olwendo, O. J., Yamazaki, Y., Cilliers, P. J., Baki, P., and Doherty, P. (2016). A study on the variability of ionospheric total electron content over the East African low-latitude region and storm time ionospheric variations. *Radio Science*, 51:1503–1518.

Onwumechikli, C. (2019). *Equatorial electrojet*. Routledge.

Opio, P., D'ujanga, F., and Ssenyonga, T. (2015). Latitudinal variation of the ionosphere in the african sector using GPS TEC data. *Advances in Space Research*, 55(6):1640–1650.

Oron, S., M.D'ujang, F., and Ssenyonga, T. J. (2013). Ionospheric TEC variations during the ascending solar activity phase at an equatorial station, Uganda. *Indian Journal of Radio and Space Physics*, 42:7–17.

Orrall, F., Fisher, R., Munro, R., and Rottman, G. (2005). Implications of a direct photometric comparison of the euv-corona and the k-corona. In *Cool Stars, Stellar Systems, and the Sun: Proceedings of the Fourth Cambridge Workshop on Cool Stars, Stellar Systems, and the Sun Held in Santa Fe, New Mexico, October 16–18, 1985*, pages 469–471. Springer.

Osei-Poku, L., Tang, L., Chen, W., and Mingli, C. (2021). Evaluating total electron content (TEC) detrending techniques in determining ionospheric disturbances during lightning events in a low latitude region. *Remote Sensing*, 13(23):4753.

Oyedokun, O., Akala, A., and Oyeyemi, E. (2020). Characterization of African Equatorial Ionization Anomaly During the Maximum Phase of Solar Cycle 24. *Journal of Geophysical Research: Space Physics*, 125.

Pastena, M., Tossaint, M., Regan, A., Castorina, M., Mathieu, P. P., Rosello, J., Gabriele, A., and Melega, N. (2020). Overview of ESA's Earth Observation upcoming small satellites missions.

Patel, N., Karia, S., and Pathak, K. (2019). Evaluation of the improvement of IRI-2016 over IRI-2012 at the india low-latitude region during the ascending phase of cycle 24. *Advances in Space Research*, 63(6):1860–1881.

Pavlov, A. (2008). The role of the zonal ExB plasma drift in the low latitude ionosphere at solar minimum and maximum near equinox. *37th COSPAR Scientific Assembly*, 37:2370.

Pretab, M. and Enge, P. (2006). *Global Positioning System signals, measurements and performance*. Ganga Jamuna Press.

Pulliam and Charles, R. (2003). *Validation of the Paramaterized Real-Time Ionospheric Specification Model (PRISM)*. PhD thesis, Ohio State University.

Quan, L., Cai, B., Hu, X., Xu, Q., and Li, L. (2021). Study of ionospheric d region changes during solar flares using mf radar measurements. *Advances in Space Research*, 67(2):715–721.

Quegan, S., Bailey, G., and Moffett, R. (1984). Regions of He+ dominance in the high-latitude topside ionosphere. *Planetary and space science*, 32(7):791–802.

Rabah, M. and Sedeek, A. (2018). Evaluation of the IGS-Global Ionospheric Mapping model over Egypt. *Annales Geophysicae Discussions*, 2018:1–21.

Rabier, F. and Liu, Z. (2003). Variational data assimilation: theory and overview. In *Proc. ECMWF Seminar on Recent Developments in Data Assimilation for Atmosphere and Ocean, Reading, UK, September 8–12*, pages 29–43.

Rao, P. V. S. R., Niranjan, K., Prasad, D. S. V. V. D., Krishna, S. G., and Uma, G. (2006). On the validity of the ionospheric pierce point (IPP) altitude of 350 Km. in the equatorial and low latitude sector. *Annales geophysicae*, 24:2159–2168.

Rawer, K., Bilitza, D., and Ramakrishnan, S. (1978). Goals and status of the international reference ionosphere. *Reviews of geophysics*, 16(2):177–181.

Reddy, C. (1989). The equatorial electrojet. *Quiet daily geomagnetic fields*, pages 485–508.

Reinisch, B. W. and Galkin, I. A. (2011). Global ionospheric radio observatory (GIRO). *Earth, planets and space*, 63:377–381.

Reinisch, B. W., Huang, X., Galkin, I. A., Paznukhov, V., and Kozlov, A. (2005). Recent advances in real–time analysis of ionograms and ionosonde drift measurements with digisondes. *Journal of Atmospheric and Solar Terrestrial Physics*, 67:1054–1062.

Richmond, A. (1995). Ionospheric electrodynamics using magnetic apex coordinates. *Journal of geomagnetism and geoelectricity*, 47(2):191–212.

Richmond, A. D. (2017). Ionospheric electrodynamics. In *Handbook of atmospheric electrodynamics (1995)*, pages 249–290. CRC press.

Ridley, A., Deng, Y., and Tóth, G. (2006). The global ionosphere–thermosphere model. *Journal of Atmospheric and Solar-Terrestrial Physics*, 68(8):839–864.

Rino, C. L. (2011). *The theory of scintillation with applications in remote sensing*. John Wiley and Sons, Inc.

Rishbeth, H. and Mendillo, M. (2001). Patterns of F2 layer variability. *Journal of Atmospheric and Solar-Terrestrial Physics*, 63:1661–1680.

Romano, V., Pau, S., Pezzopane, M., Zuccheretti, E., Zolesi, B., De Franceschi, G., and Locatelli, S. (2008). The electronic space weather upper atmosphere (eSWua) project at INGV: advancements and state of the art. In *Annales Geophysicae*, volume 26, pages 345–351. Copernicus Publications Göttingen, Germany.

Sabzehee, F., Farzaneh, S., Sharifi, M. A., and Akhoondzadeh, M. (2018). TEC Regional Modeling and prediction using ANN method and single frequency receiver over IRAN. *Annals of Geophysics*, 61(1):GM103–GM103.

Sardón, E., Rius, A., and Zarraoa, N. (1994). Estimation of the transmitter and receiver differential biases and the ionospheric total electron content from global positioning system observations. *Radio Science*, 29(03):577–586.

Saryo, T., M, T., T, A., T, S., Tsuda.T, Fukao.S, and S, K. (1989). A midday bite-out event of the F2-layer observed by MU radar. *Journal of Geomagnetism and Geoelectricity (Tokyo)*, 41(8):727–734.

Schunk, R. (1988). A mathematical model of the middle and high latitude ionosphere. *Pure and applied geophysics*, 127:255–303.

Schunk, R. and Nagy, A. (2009). *Ionospheres: Physics, Plasma Physics, and Chemistry*. Cambridge University Press.

Schunk, R. and Walker, J. (1973). Theoretical ion densities in the lower ionosphere. *Planetary and Space Science*, 21(11):1875–1896.

Schunk, R. W., Banks, P. M., and Raitt, W. J. (1976). Effects of electric fields and other processes upon the nighttime high-latitude F layer. *Journal of Geophysical Research*, 81(19):3271–3282.

Schunk, R. W. and Sojka, J. J. (1982). Ion temperature variations in the daytime high-latitude f region. *Journal of Geophysical Research: Space Physics*, 87(A7):5169–5183.

Schunk, R. W., Sojka, J. J., and Bowline, M. (1986). Theoretical study of the electron temperature in the high-latitude ionosphere for solar maximum and winter conditions. *Journal of Geophysical Research: Space Physics*, 91(A11):12041–12054.

Scotto, C. and Sabbagh, D. (2021). Climatology of spread F over tucumán from massive statistical analysis of autoscaled data. *Atmosphere*, 12(10):1351.

Sedeek, A., Doma, M., Rabah, M., and Hamama, M. (2017). Determination of zero difference GPS differential code biases for satellites and prominent receiver types. *Arabian journal of geosciences*, 10:1–11.

Seemala, G. K. (2023). Estimation of ionospheric total electron content (TEC) from GNSS observations. In *Atmospheric remote sensing*, pages 63–84. Elsevier.

Seemala, G. K. and Valladares, C. (2011). Statistics of total electron content depletions observed over the south american continent for the year. *Radio Science*, 46:RS5019.

Setti Júnior, P. d. T., Alves, D. B. M., and Silva, C. M. d. (2019). Klobuchar and nequick g ionospheric models comparison for multi-gnss single-frequency code point positioning in the brazilian region. *Boletim de Ciências Geodésicas*, 25:e2019016.

Shakouri, M. and Banihashemi, S. (2019). Developing an empirical predictive saved load-rating model for windows by using artificial neural network. *International Journal of Green Energy*, 16(13):961–970.

Shanmuganathan, S. (2016). *Artificial neural network modelling: An introduction*. Springer.

Shi, C., Zhang, T., Wang, C., Wang, Z., and Fan, L. (2019). Comparison of IRI-2016 model with IGS VTEC maps during low and high solar activity period. *Results in Physics*, 12:555–561.

Shim, J. S. (2009). *Analysis of Total Electron Content (TEC) Variations in the Low- and Middle-Latitude Ionosphere.* PhD thesis, Utah State University, All Graduate Theses and Dissertations. 403.

Sojka, J. J., Raitt, W. J., and Schunk, R. W. (1981). Plasma density features associated with strong convection in the winter high-latitude F region. *Journal of Geophysical Research: Space Physics*, 86(A8):6908–6916.

Sunehra, D. (2013). Validation of gps receiver instrumental bias results for precise navigation. *Indian Journal of Radio and Space Physics*, pages 175–181.

Sussillo, D., Nuyujukian, P., Fan, J. M., Kao, J. C., Stavisky, S. D., Ryu, S., and Shenoy, K. (2012). A recurrent neural network for closed-loop intracortical brain–machine interface decoders. *Journal of neural engineering*, 9(2):026027.

Tang, Q., Zhao, J., Yu, Z., Liu, Y., Hu, L., Zhou, C., Zhao, Z., and Feng, X. (2021). Occurrence and variations of middle and low latitude sporadic E layer investigated with longitudinal and latitudinal chains of ionosondes. *Space Weather*, 19(12):e2021SW002942.

Thakur, A. and Konde, A. (2021). Fundamentals of neural networks. *International Journal for Research in Applied Science and Engineering Technology*, 9(VIII):407–426.

Thomson, N. R., Clilverd, M. A., Brundell, J. B., and Rodger, C. J. (2021). Quiet night arctic ionospheric d region characteristics. *Journal of Geophysical Research: Space Physics*, 126(4):e2020JA029043.

Tilahun, S. and Mezgebe, N. (2019). $\triangle$h as a proxy for the variations of $E \times B$ drift and plasma irregularity over east africa. *Advances in Space Research.*

Titheridge, J. (1968). Nighttime changes in the electron content of the ionosphere. *Journal of Geophysical Research*, 73(9):2985–2993.

van den IJssel, J., Encarnação, J., Doornbos, E., and Visser, P. (2015). Precise science orbits for the swarm satellite constellation. *Advances in Space Research*, 56(6):1042–1055.

Verhoeven, C. J., Bentum, M. J., Monna, G., Rotteveel, J., and Guo, J. (2011). On the origin of satellite swarms. *Acta Astronautica*, 68(7-8):1392–1395.

Vinnikov, K. Y., Robock, A., Grody, N. C., and Basist, A. (2004). Analysis of diurnal and seasonal cycles and trends in climatic records with arbitrary observation times. *Geophysical research letters*, 31(6).

Wang, G. J., Shi, J. K., Wang, X., and Shang, S. P. (2008). Seasonal variation of spread-F observed in Hainan. *Advances in Space Research*, 41:639–644.

Wang, J., Yu, Q., Shi, Y., Yang, C., Ji, S., and Zheng, Y. (2024). A new determining method for ionospheric f2-region peak electron density height. *Remote Sensing*, 16(3):531.

Wang, X.-L., Wan, Q.-T., Ma, G.-Y., Li, J.-H., and Fan, J.-T. (2016). The influence of ionospheric thin shell height on TEC retrieval from GPS observation. *Research in Astronomy and Astrophysics*, 16(7):016.

Whitehead, J. D. (1989). Recent work on mid-latitude and equatorial sporadic-E. *Journal of Atmospheric and Terrestrial Physics*, 51:401–424. Research supported by the Australian Research Council.

Wilson, B. D. and Mannucci, A. J. (1993). Instrumental biases in ionospheric measurement derived from GPS data. *Jet propulsion laboratory, Califonia institute of technology.*

Withers, P., Felici, M., Hensley, K., Mendillo, M., Barbinis, E., Kahan, D., Oudrhiri, K., and Girazian, Z. (2023). The ionosphere of mars from solar minimum to solar maximum: Dayside electron densities from maven and mars global surveyor radio occultations. *Icarus*, 393:114508.

Wood, A. G., Alfonsi, L., Clausen, L. B., Jin, Y., Spogli, L., Urbář, J., Rawlings, J. T., Whittaker, I. C., Dorrian, G. D., Høeg, P., et al. (2022). Variability of ionospheric plasma: results from the ESA swarm mission. *Space Science Reviews*, 218(6):52.

Yang, X., Li, J., and Zhang, S. (2014). Ionospheric correction for spaceborne single-frequency GPS based on single layer model. *Journal of Earth System Science*, 123.

Ya'acob, N., Abdullah, M., and Ismail, M. (2010). Gps total electron content (tec) prediction at ionosphere layer over the equatorial region, trends telecommun.

Ya'acob, N., Abdullah, M., Ismail, M., and Zaharim, A. (2009). Model validation for GPS total electron content (TEC) using 10th polynomial function technique at an equatorial region. *WSEAS Transactions on Computers*, 8(9):1533–1542.

Yeh, K. C. and Liu, C.-H. (1982). Radio wave scintillations in the ionosphere. *Proceedings of IEEE*, 70(4):324–360.

Yen, N. L., Fong, C.-J., Chu, C.-H., Miau, J.-J., Liou, Y.-A., and Kuo, Y.-H. (2010). Global GNSS radio occultation mission for meteorology, ionosphere & climate. *Aerospace Technologies Advancements, edited by Arif, TT*, pages 241–258.

Zell, H. (2015). Earth's atmospheric layers. *Retrieved November*, 12:2016.

Zhang, L., Liu, Y., Liu, Y., Gong, J., Lu, H., Jin, Z., Tian, W., Liu, G., Zhou, B., and Zhao, B. (2019). The operational global four-dimensional variational data

assimilation system at the china meteorological administration. *Quarterly Journal of the Royal Meteorological Society*, 145(722):1882–1896.

Zhang, M.-L., Wan, W., Liu, L., and Ning, B. (2009). Variability study of the crest-to-trough TEC ratio of the equatorial ionization anomaly around 120 E longitude. *Advances in Space Research*, 43(11):1762–1769.

Zhang, S.-R., Oliver, W., Fukao, S., and Otsuka, Y. (2000). A study of the forenoon ionospheric F2 layer behavior over the middle and upper atmospheric radar. *Journal of Geophysical Research: Space Physics*, 105(A7):15823–15833.

Zhao, J. and Zhou, C. (2019). Validation and application of optimal ionospheric shell height model for single-site estimation of total electron content. *Annales Geophysicae*, 37:263–271.

Zhong, J., Lei, J., Dou, X., and Yue, X. (2016). Assessment of vertical TEC mapping functions for space-based GNSS observations. *GPS Solutions*, 20:353–362.

Zhou, S., Shi, Z., and Fu, H. (2023). Prediction of global ionospheric tec based on deep learning and singular spectrum analysis. In *2023 International Applied Computational Electromagnetics Society Symposium (ACES-China)*, pages 1–3. IEEE.

Zhu, F., Yang, J., Qing, Y., and Li, X. (2023). Assessment and analysis of the global ionosphere maps over china based on CMONOC GNSS data. *Frontiers in Earth Science*, 11:1095754.

Zuccheretti, E., Tutone, G., Sciacca, U., Bianchi, C., Baskaradas, J., et al. (2003). The new AIS-INGV digital ionosonde. *Annals of Geophysics*.